COMPRESSIVE AND FLEXURAL PROPERTIES OF POROUS BUILDING MATERIALS CREATED FROM CONTAMINATED WASTE GLASS

Renuka Prabhakar

A thesis
submitted in partial fulfillment of the
requirements for the degree of

Master of Science in Mechanical Engineering

University of Washington
2012

Committee:
Ramulu Mamidala – Chair
John Kramlich
Per Reinhall

Program Authorized to Offer Degree:
Department of Mechanical Engineering

ABSTRACT

A new, energy efficient recycling technology is being developed that is compatible with post-consumer and post-industrial waste glass. This technology may be used to produce sustainable materials for the green building industry. During the process, materials are consolidated through cold isostatic pressing and then densified at temperatures up to 55% lower than the melting temperature. Densification through warm working was found to be compatible with common contaminants present in the glass waste stream and the process results in porous materials that possess up to 95% recycle content. Moreover, when compared to traditional manufacturing techniques, this process will reduce energy consumption by up to 70%. The objectives of this research were to characterize the physical and mechanical behavior of materials created through this process and compare these behaviors to established models for porous brittle materials. In addition, the sintering behavior of contaminated waste glass was characterized through fractography.

The results of this research show that high strength materials with predictable physical and mechanical behavior can be successfully formed at very low temperatures. Given the random nature of the pore structure, a probabilistic rather than deterministic approach was utilized in characterizing the mechanical behavior of the material. Analysis of the data yielded values for compressive strength varying between 6.8 and 150.8 MPa and values for transverse rupture strength varying between 2.8 and 29.9 MPa. In addition, the presence of contaminants did not impede sintering and materials with a wide range of porosity could be produced by using this process. Further, it was found that the resulting materials exhibited performance characteristics in excess of requirements for common masonry materials used in the construction industry.

TABLE OF CONTENTS

LIST OF FIGURES

LIST OF TABLES

ACKNOWLEDGEMENTS

The research described within this document was supported by grant funding from the University of Washington Center for Commercialization and the National Science Foundation. The author also wishes to express sincere appreciation to the College of Engineering and the Department of Mechanical Engineering for their continued support with this research. In addition, this work reflects upon Professor Ramulu's dedication to his students and to the Mechanical Engineering discipline.

CHAPTER 1. INTRODUCTION & OBJECTIVES

In recent years, there has been a growing desire to integrate waste stream materials into feedstocks for the manufacture of new products. For many metallic and plastic materials and some ceramics, recycling techniques have been very successful; however this is not the case with glass. Although pure glass is infinitely recyclable, waste glass commonly found in the solid waste stream is littered with contaminants and because of this, current recycling methods for glass are extremely energy intensive and costly. This inefficiency has contributed to very low recycling rates. In 2010, 11.5 million tons of glass entered the municipal solid waste stream. Merely 27% of the glass waste stream was recovered for recycling, with the remaining 73% accumulating at solid waste facilities, amplifying the need for waste storage infrastructure [1].

Of the recovered glass, nearly 90% was used to reduce the energy and materials costs associated with container manufacturing, where it was combined with traditional virgin materials. Unfortunately, the container glass manufacturing process is extremely sensitive to contaminants present in the waste stream, such as paper, plastic, metal, ceramics and adhesives. Even colored glasses are considered contaminants; their varying composition and melting temperatures have been shown to increase the number of defects present in finished products. These defects include pores, voids, micro-cracks, and inclusions. Therefore, before recycled glass can be used in container production, it must undergo intensive sorting and cleaning operations.

The energy expended on these processes is barely offset by the energy saved through diluting the virgin material stream; in fact, when the virgin materials are diluted by 10%, overall energy consumption is reduced by a scant 2-4%[1]. Moreover, manufacturers have found that as

the percentage of post-consumer glass is increased, the quality of the manufactured container goes down in terms of both mechanical performance and aesthetics.

New recycling technologies must be developed in order to turn waste streams into material sources for new products that are both environmentally responsible and economically viable. The research described in this document will build upon prior work conducted at the University of Washington, by Marchelli and Prabhakar, in which pulverized glass was combined with organic binders, formed into green compacts via cold isostatic pressing (CIP) and then consolidated through a low-temperature heating process[2]. The process was found to be compatible with contaminated glass and resulted in porous articles composed of over 95% waste glass. Preliminary testing indicated that these articles exhibited mechanical properties similar to that of common porous building materials, such as masonry. Moreover, these materials were produced at ~45% of the melting temperature and data acquired during their work indicated that the embodied energy of these articles was nearly 70% lower than that of clay brick and 75% lower than that of common container glass. However, the materials created through this process exhibited a wide range of porosity. Neither the morphology of the pores nor the relationship between porosity and mechanical properties had been investigated.

The purpose of this research is to establish the feasibility of using the process developed by Marchelli and Prabhakar to produce high recycle content building materials that possess low embodied energy. Many types of porous brittle materials, such as brick, concrete and tile, are used commonly in the construction industry. Brick and similar masonry products are generally used in applications where design loads are compressive in nature. However, in several of these applications, materials are also expected to withstand flexural loading. The requirements for compressive and flexural strength in structural ceramics are established by American Society for

Testing and Materials (ASTM). Successful completion of this work may provide the manufacturing and construction industries with sustainable alternatives to standard products, while also providing a commercial outlet for the large quantities of waste stream glass that cannot currently be recycled. Further, this work will contribute to the scientific understanding of porous materials, particularly with respect to contaminated waste glass. The objectives of this research are as follows:

1. Investigate the relationship between the peak firing temperature and the bulk properties of the material.
2. Characterize the relationship between porosity and the mechanical properties of the material.
3. Compare observed mechanical behavior to zero porosity behavior and to established empirical and theoretical models.
4. Characterize sintering behavior through fractography.

This thesis is organized as follows. Background information will be presented in Chapter 2 and will include a discussion of prior experimental approaches and theoretical modeling techniques. The experimental work performed will be described in Chapter 3, where the densification process and the evaluation of mechanical properties will be discussed. The results of experimentation will be presented in Chapter 4, followed by a discussion of these results in Chapter 5 and conclusions in Chapter 6. This report will conclude with recommendations for future work in Chapter 7.

CHAPTER 2. BACKGROUND & LITERATURE REVIEW

2.1 BACKGROUND

2.1.1. GLASS MANUFACTURING AND RECYCLING

Glass has been produced for 1000s of years and in that time many different compositions have been formulated. Today glass is used primarily in the manufacture of containers and windowpanes. Plate or sheet glass and container or bulb glass can be manufactured through a variety of processes, all of which involve melting the virgin materials at temperatures of up to 1800°C. The majority of these glasses fall into the soda-lime silicate category and exhibit lower melting temperatures than glasses belonging to other families. Soda-lime silicate glasses are generally composed of 65-75% SiO_2, 13-18% Na_2O, 6-12% CaO, 0-7% K_2O 0-4.5% MgO, 0-4% Al_2O_3 and 0-1% Fe_2O_3. The composition directly affects the mechanical properties of the resulting products and manufacturers adjust the composition for specific applications. Published values for the relevant physical and mechanical properties of common soda-lime silicate glasses are given in Table 1, on the following page.

In order for waste stream soda-lime silicate glass to be incorporated into the virgin raw material stream it must be extremely clean. Recycled glass undergoes a number of processing steps between collection and resale. First, the glass is coarsely sorted from other waste and during that process it is broken down into smaller pieces termed "cullet." As the cullet get smaller and smaller sorting becomes increasingly difficult. Glass processors and manufacturers have found that cullet smaller than ~8 mm cannot be cleaned to the level required in container or sheet glass manufacturing through cost effective means. A significant volume (over 30,000 tons) of this small cullet is produced annually and, because of the high contamination levels and small size, this waste glass cannot currently be used by industry and has no commercial value.

Table 1. Physical and mechanical properties of common soda-lime silicate glasses.

Glass Type	Density (g/cm^3)	Compressive Strength (MPa)	Flexural Strength (MPa)	Elastic Modulus (GPa)	Poisson's Ratio
soda-lime silicate plate[3]	2.5				
Asahi AS soda-lime silicate[4]	2.49				
soda-lime silicate[5]	2.5				
soda glass[6]		2000-3000			
soda-lime silicate bulb[7]			102		
soda-lime silicate[8]			166		
soda-lime silicate[8]			135		
soda-lime silicate plate[3]				74	
soda-lime silicate[8]				67.1	
soda-lime silicate bulb[7]				70.3	
Asahi AS soda-lime silicate[4]				71.7	
soda-lime silicate[5]				69	
soda-lime silicate plate[3]					0.22
soda-lime silicate bulb[7]					0.24
soda-lime silicate[8]					0.215
Asahi AS soda-lime silicate[4]					0.21

2.1.2. Densification Through Sintering

Sintering is a powder process widely used in the manufacture of metals, plastics, ceramics and glasses. The powdered materials are first consolidated at high pressure and then densified through a heating process[9-12]. Densification takes place in three stages and the first stage is shown below in Figure 1 [13].

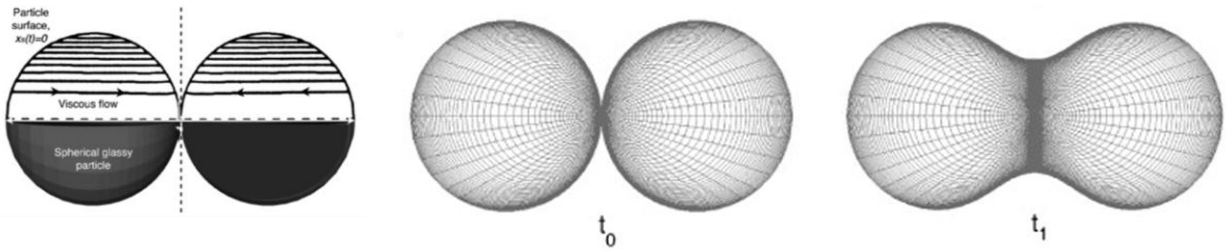

(a) (b) (c)

Figure 1. Graphical representation of necking between particles during the sintering process. (a) Depicts direction of viscous flow. b) Depicts contact area between particles at t=0. (c) Depicts the formation of a neck.

During the first stage in the densification process the viscosity of the particles is reduced sufficiently to allow for the material to flow. This occurs slightly above the glass transition temperature, which for soda-lime silicate glasses is ~615°C. The particles begin to soften and behave in a more rubbery manner, which allows them to settle and become more densely packed. This increases the contact area between adjacent particles and they begin to fuse together; this is known as necking. The second stage in the process occurs near the dilatometric softening point (~675° for soda-lime silicate glasses). At this temperature the particles are extremely soft and the contact surface area is much higher. This accelerates the necking process and as the number and size of necks increase, grains begin to form. It is during the second stage that the porous network forms. The third stage is known as the crystallization stage and during this stage grain growth dominates. As the grains become larger, they begin to engulf the pores and isolate them from the porous network. After full crystallization only a percentage of isolated pores will continue to exist within the resulting solid body. In soda-lime silicate glasses crystallization takes places between ~750 and 975°C.

2.1.3. Mechanical Properties

The uniaxial compression test is a common technique for establishing the compressive strength of materials. Load and displacement data are used to calculate the engineering stress and strain at many points during testing using Equations 2.1 and 2.2, where σ_c is defined as the compressive stress, P_c is the compressive load, A_o is the initial cross sectional area of the specimen perpendicular to loading direction, Δl is the change in thickness of the specimen, and l_o is the initial thickness[14, 15].

$$\sigma_c = P_c / A_o \tag{2.1}$$

$$\varepsilon = \left(\frac{\Delta l}{l_o}\right) \tag{2.2}$$

In pure compression, the fracture plane is expected to form a 45° angle with the plane of maximum principal stress. This can be demonstrated using Mohr's circle (Figure 2) and Equation 2.3, where τ_{max} is the maximum shear stress and σ_1 and σ_2 are the principal stresses[14, 15]. In the case of pure compression σ_1 is equal to zero and solving for θ yields 45°.

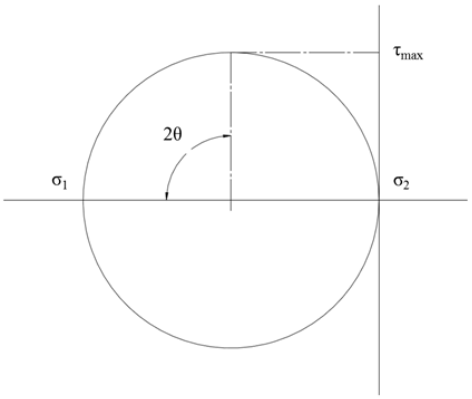

Figure 2. Mohr's circle for uniaxial compression.

$$\tau_{max} = \frac{(\sigma_1 - \sigma_2)\sin 2\theta}{2} \tag{2.3}$$

Brittle and porous materials are seldom subjected to pure tensile stresses in service, as their tensile strength is almost invariable much lower than their compressive strength. Further, tensile testing is often unsuccessful or yields inaccurate values of tensile strength, as failure generally occurs very near the grips. During the characterization of brittle material researchers often forego tensile testing in favor of flexural testing. This provides data regarding the transverse rupture strength of the specimen, which describes the material's ability to resist deformation under flexural loads, as well as data regarding the material's elastic modulus in flexure. Because of its relative ease, flexural testing is most commonly performed via the 3-point bending test, as shown in Figure 3, on the following page.

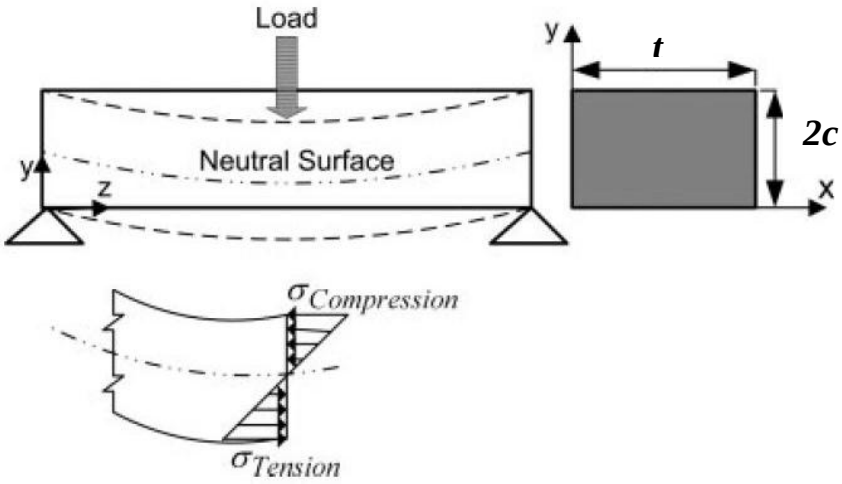

Figure 3. Prismatic specimen in 3 point bending.

In Figure 3, the upper left image depicts a prismatic specimen under 3-point loading. The specimen is supported on the underside in two locations and the load is applied from above at equal distance from both supporting members. The upper right image shows the cross sectional view of a typical specimen. The lower view shows the distribution of stresses induced in the specimen normal to the direction of loading, where it can be seen that the stresses vary with depth. The uppermost fibers are subjected to compressive stresses, while the bottommost fibers are subjected to tensile stresses. The central plane of the specimen is subjected to no stresses at all and is termed the neutral surface. The transverse stress in a specimen subjected to 3-point bending is given by Equation 2.4-2.6[14, 15], where σ_t is the transverse stress, M is the bending moment, I is the area moment of inertia, c is the distance from the neutral plane, P is the applied load, L is the support span, t is the width of the specimen. The transverse strain is defined as in Equation 2.7, where D is the deflection of the beam directly under the load.

$$\sigma_t = \frac{Mc}{I} \tag{2.4}$$

$$I = \frac{2tc^3}{3} \tag{2.5}$$

$$M = \frac{PL}{4} \tag{2.6}$$

$$\varepsilon = \frac{12Dc}{L^2} \tag{2.7}$$

The elastic modulus describes a material's ability to undergo elastic deformation when subjected to loading. The elastic modulus can be calculated from the stress-strain data acquired through compressive, tensile or flexural testing. In isotropic materials, the values calculated from any of the three sets of data will be equivalent. In anistropic materials, these values will differ due to the inherent directionality of the material. The most common form of the elastic modulus is Young's modulus as shown in Equation 2.8, where E is Young's modulus, σ is the stress in compression, tension or flexure and ε is the corresponding strain. Young's modulus is used to describe materials that exhibit linear elastic behavior during the initial stages of loading and mathematically, it is the slope of the initial, linear portion of the stress strain curve [15].

$$E = \frac{\sigma}{\varepsilon} \tag{2.8}$$

2.2. Experimental Investigations

2.2.1. Porous Glass

Porous glasses have become a topic of increased interest in recent years, particularly in the fields of confined matter, solid-phase biochemistry, optical chemosensors, composites, membrane technology and bioengineering. The materials are typically produced through one of two processes: leaching of phase-separated alkali-borosilicate glass, or preparation via the sol-gel process[16]. The preparation of porous glass through leaching of phase-separated glass has been performed for nearly sixty years and has been the preferred method, as it produces open or closed cell materials with predictable geometry and controllable pore sizes in the 0.3-1000 nm range.

2.2.2. Foamed Glass

On a larger scale porous glass materials have been produced for decades through foaming processes [17-21]. Materials produced via foaming are generally described as cellular, as they exhibit a large void to solid ratio and voids are arranged in a roughly geometric fashion[6]. Originally this process involved the introduction of reactive gases into the molten glass during processing; this required high temperatures and was therefore very energy intensive. Another technique, first developed in the 1940s, allows for foamed glass materials to be produced through cold isostatic pressing (CIP) processes and then consolidated at lower temperatures (T = ~$0.55T_m$) [17, 18, 22]. This method has gained popularity in recent years because of its lower energy requirements.

In CIP processes, the glass is first pulverized to less than 50 microns and then a foaming agent is added in powder form, after which the mixture is formed into molds at high pressure. Recent work has shown that waste glass is compatible with this process [23-25]. Bernardo et al.[20] showed that several types of waste glasses can be densified successfully through foaming processes; unfortunately the feedstocks used were refined wastes and did not contain contaminants typical of municipal waste glass. The materials used in these investigations exhibited bulk densities ranging from 0.22 to 0.42 g/cm^3 and were found to agree with Gibson and Ashby's models for the compressive strength of foams[6].

2.2.3. Sintered Waste Glass

Several researchers have also demonstrated that waste glass can be successfully incorporated into high-density glass ceramics [26-29]. Bernardo's experimental work focuses on the crystallization of industrial wastes through fast sintering at slightly higher temperatures than used during foaming processes (T = ~$0.6T_m$) and results in materials with porosities ranging from

2.8% to 22%. However, in this investigation the waste glass was first fully melted and then cooled and pulverized to the desired size. Again, this work uses raw materials with a rather narrow particle size distribution (<37 microns). Their results indicate transverse rupture strength as high as 130.7 MPa and elastic moduli as high as 89.3 GPa at 3% porosity. At 22% porosity they report values for the transverse strength and elastic modulus of 59.1 MPa and 48.8 GPa respectively.

2.3. Porosity-Property Relations

The manufacture and mechanical characterization of porous ceramics have been topics of interest since the 1950s. Since that time advanced ceramic materials have been used in a wide range of applications, including sensors, insulators, heat exchangers, particulate filters, refractories, building materials and more recently, bone scaffolds. Researchers have proposed many models to characterize the behavior of materials in relation to their porosity or bulk density. The relevant models are given in Table 2.

Some of the earliest work was presented by MacKenzie in 1950, where he proposed a quadratic relationship between porosity and the elastic modulus of porous ceramics (Eq. 2.13)[30]. This was empirical in nature and has been found to fit wide range of experimental data. Duckworth followed in 1953 with his commentary on Ryshkewitch's work, where he proposed an empirical, exponential relationship between porosity and compressive (Eq. 2.9) [31, 32]. Spriggs[33] then extended Duckworth's work to the relationship between porosity and elastic modulus in 1961 (Eq. 2.14). This was predicated on Knudsen's[34] research, which assumed that the solid phase of the material was composed of spherical particles.

The drawback of Spriggs' model was that it failed to satisfy the boundary conditions e.g. a calculation with porosity equal to one would not result in an elastic modulus value of zero. This

was addressed by Hasselman (Eq. 2.15) in 1962[35], when he proposed a semi-empirical approach based on Hashin's work (Eq. 2.16) [36], in which the shear or bulk modulus was expressed in terms of the continuous phase and the disperse phases present in the material. Again, this work assumed that the continuous phase was composed of spherical particles.

Realizing that porosity alone did not account for variations in mechanical properties, researchers began to recognize the importance of pore geometry. In 1964, Brown, Biddulph and Wilcox proposed a 2/3-power relationship based on their investigation on the effects of pore geometry and orientation (Eq. 2.17)[37]. Wang's 1984 work focused on the effects of open versus closed cell pores and he proposed an exponential relationship similar to Spriggs', which included higher order terms (Eq. 18) [38]. This was based on a theoretical model in which materials were composed of spherical particles packed in a cubic array and was found to agree with experimental data at the lower end of the porosity range (≤ 0.32).

This led to Phani and Niyogi's semi-empirical power model, which was meant to account for pore interconnectivity (Eq. 2.19) [39]. The Phani-Niyogi model was later simplified by Wagh, Singh and Poeppel, whose model assumes random pore geometry and packing density (Eq. 20) [40]. In 1993, Ramakrishnan[41] built on the composite sphere model using a two phase approach like Hashin (Eq. 2.22). His correlation was based on the effective Poisson's ratio of two-phase materials.

In the early, 1990s Nielsen proposed a theoretical model that was found to successfully predict behavior in a broad range of materials, including porous glasses. His work focused on the relationship between porosity and stiffness (Eq. 2.21)[42, 43] and the models were based on pore size, pore geometry, and pore interconnectivity. In addition, materials could be characterized by the coarseness of the porous structure.

Gibson and Ashby also proposed relationships between the strength, elasticity and porosity of cellular materials[6]. This work was based on the relative density of the two-phase material and was largely theoretical. The models were built upon the geometry of the walls, which in cellular materials can be quite tightly controlled. Their models for open and closed cell foams were found to successfully predict compressive strength in a wide range of materials including ceramics, plastics and metals (Equations 2.10-2.12). Gibson and Ashby are often cited by researchers investigating glass foams and foaming techniques [25, 44].

The equations are shown on the following page in Table 2. In Equations 2.9-2.12, σ represents the compressive strength, σ_o is the zero porosity compressive strength, P is the porosity, and ρ_r is the relative density, while a, b and φ are fitting parameters. The parameter φ describes the degree to which cells are open or closed and can vary between zero and one. In Equations 2.13-2.22, E_o is the zero porosity value of the elastic modulus, v_o is the zero porosity Poisson's ratio and a, b, c, f_1 and f_2 are fitting parameters. In Equations 2.16 and 2.21 the data is fit by manipulating Poisson's ratio. In Equation 2.21, a describes the complexity of the pore structure, P_D is the critical porosity and M describes variation in interaction of the pores. Nielsen's work has shown that the elastic modulus of porous glasses is successfully predicted when P_D and M are equal to unity.

Table 2. Published models for strength and elastic modulus as a function of porosity.

Duckworth[32]	$\sigma = \sigma_o e^{-aP}$		(2.9)
Gibson-Ashby: Open Cell[6]	$\sigma = \sigma_o a {\rho_r}^{3/2}$		(2.10)
Gibson-Ashby: Open, high density[6]	$\sigma = \sigma_o a {\rho_r}^{3/2}\left(1 + {\rho_r}^{1/2}\right)$		(2.11)
Gibson-Ashby: Closed Cell[6]	$\sigma = \sigma_o a(\varphi\rho_r)^{3/2} + b(1-\varphi)\rho_r$		(2.12)
MacKenzie[40]	$E = E_o(1 - f_1 P + f_2 P^2)$		(2.13)
Spriggs[33]	$E = E_o e^{-bP}$	$P \leq 0.5$	(2.14)
Hasselman[35]	$E = E_o\left[1 - \frac{aP}{1 + (\mathrm{a} - 1)P}\right]$		(2.15)
Hashin[37]	$E = E_o\left(\frac{1-P}{1+kP}\right)$ $k = \frac{(1+v_o)(13-15v_o)}{2(7-5v_o)}$		(2.16)
Brown et al.[45]	$E = E_o(1 - aP^{2/3})$		(2.17)
Wang[38]	$E = E_o e^{[-(bP + cP^2)]}$	$\mathrm{P} \leq 0.32$	(2.18)
Phani-Niyogi[39]	$E = E_o(1 - aP)^n$		(2.19)
Wagh-Poeppel-Singh[40]	$E = E_o(1 - P)^n$		(2.20)
Nielson[43]	$E = E_o\left(\frac{1-P}{1+P/\mu}\right)$ $\mu = a(1 - P/P_d)^M$		(2.21)
Ramakrishnan[41]	$E = E_o\frac{(1-P)^2}{1+k_E P}$ $k_E = 2 - 3v_o$		(2.22)

2.4. SUMMARY

Many investigations have explored the addition of waste glass into the virgin raw material stream. This work has been largely unsuccessful and currently, the energy and cost associated with incorporating waste stream materials outweighs any advantage. More promising research has been centered on incorporating waste glass into foaming and sintering processes. Both the foaming and fast sintering work has resulted in significant reductions in energy expenditures. However, Marchelli and Prabhakar's work poses three significant advantages. First the process temperatures used by Marchelli and Prabhakar were ~15-30% lower than those used in prior investigations and the preliminary melting step was omitted entirely. This reduces the energy requirements of the process significantly. Second, Marchelli and Prabhakar were able to utilize raw materials with a broader particle size distribution. This may mean that less energy will be required to pre-process feedstocks. Third, the process described by Marchelli and Prabhakar's was the first work to utilize contaminated waste glass in a process that does not result in crystallization. This is compelling as crystallized materials have little utility in the built environment. Their density, stiffness and low strength to weight ratio make them appropriate for a very narrow range of applications.

Theoretical investigations into the mechanical properties of porous materials have resulted in a wide variety of models. Generally these models are based on the assumption that the solid phase of the material can be approximated by spherical particles or that the material can be modeled as cellular. It is unclear how accurately these models will predict the behavior in a non-homogenous material.

CHAPTER 3. EXPERIMENTAL WORK

3.1. GREEN COMPACT & DENSIFICATION

3.1.1. MATERIALS

The materials used in this research were collected from the municipal waste stream in the greater Seattle area. The composition of collected glass can vary significantly. After collection, it was processed by TriVitro® into a product called VG105, which contains irregularly shaped particles of differing size. This product is generally sold as a sandblasting medium and is screened to the appropriate size for that particular application. Independent particle size analysis was performed prior to experimentation and data was obtained via sieve analysis. The results of the analysis are shown in Figure 4.

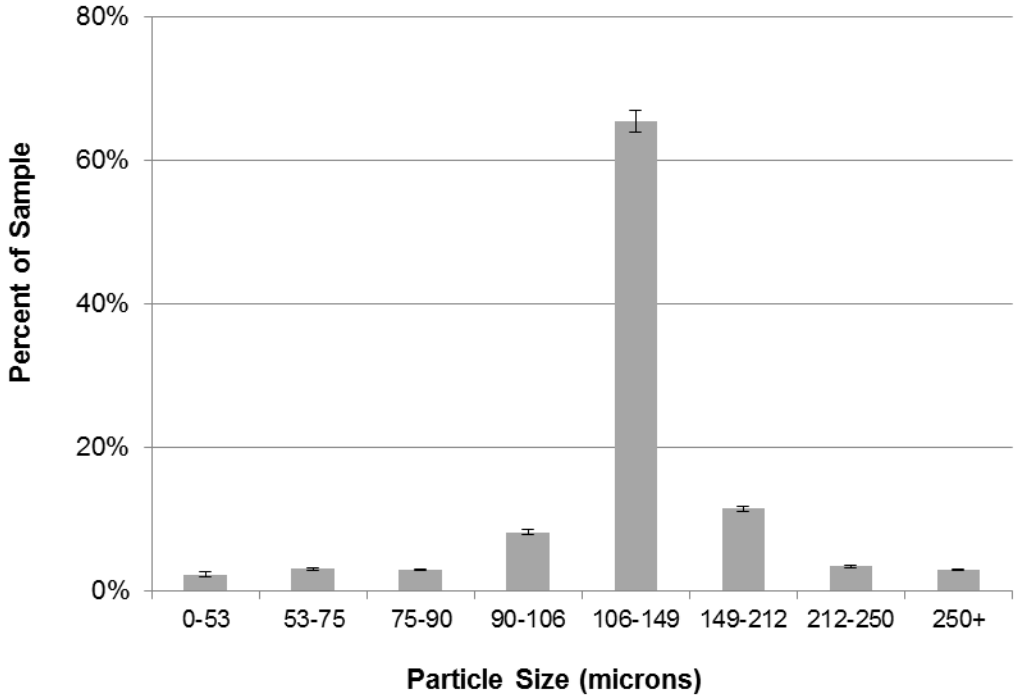

Figure 4. Particle size distribution of waste glass feedstock. Results were obtained through sieve analysis.

The particle size distribution exhibits Gaussian behavior, with particles being concentrated in the 106-149 micron range. The as received glass was not processed in any way prior to

experimentation. It was not further screened or sorted for color and contamination was not removed.

3.1.2. Experimental Procedure

Specimens composed of waste soda-lime silicate glass were formed using the method described by Marchelli and Prabhakar and green compacts were formed in the cold state using a CIP method[2]. Materials were formed in aluminum molds and hydrostatic pressure was applied by means of a Wabash 30-1515-2TMB four-post hydraulic press with an operating range of 0 to 30 tons (0-266.9 kN). Prismatic specimens with two specific geometries were formed in batches of 20. The first type of specimen was to be used in subsequent compressive testing and these specimens were formed to nominal green dimensions of 1.25" x 1.25" x 0.5" (31.75mm x 31.75mm x 12.7mm). The second type of specimen was to be used in subsequent flexural testing and these specimens were formed to nominal green dimensions of 1.75" x 0.75" x 0.5" (44.45mm x 19.05mm x 12.7mm). In an effort to simulate the process used in the industrial production of clay brick and comparable masonry products, specimens were formed using 1 ton of force (~8900 N).

Once formed, the green compacts were removed from the molds and allowed to dry at ambient conditions for 48 hours. At this time the green dimensions were recorded; width and length were measured using 6 inch Mitutoyo Absolute Digimatic calipers (Model 500-171) with accuracy of +/- 0.001inches (+/- 0.0254 mm) and the thickness was measured using a Mitutoyo 570 Series height gage with accuracy of +/-0.002 inches (+/- 0.0508 mm). Two measurements were recorded for the length, two for the width and three for the thickness of each specimen. Specimens were then fired on one inch (2.54 mm) thick vermiculite in a Cress C181822-DWH electric furnace with chamber dimensions of 18"H x 18"W x 22"D (0.457m x 0.457m x 0.559m)

and chamber uniformity of +/- 25°F (+/- 14°C). Vermiculite is a low-density material often used in the densification of ceramics. Because of its low thermal mass, specimens that are fired on vermiculite rather than directly on the firebrick or on alumina kiln furniture, experience more uniform heat transfer and deformation during firing is minimized.

Fourteen batches were prepared using the above procedure: seven batches of compression specimens and seven batches of flexural specimens. The batches were then fired at peak temperatures between 705 and 790°C. It should be noted that this is only slightly above the dilatometric softening temperature of soda-lime silicate waste glasses (~675°C) and 15-30% lower than the firing temperatures used in previous work with waste glass[25-29]. Once the densification process was complete, dimensional measurements of each specimen were recorded using the procedure described above for the green state specimens. These data were then used to calculate the mean and standard deviation of volumetric shrink for each batch.

The apparent porosity and bulk density were calculated using the Archimedes' method[46]. All data was taken using an Ohaus Adventurer laboratory scale with +/- 0.001g readability. Once the specimens were fired, their dry mass (*D*) was recorded. The specimens were then boiled in distilled water at 100°C for 5 hours and allowed to soak at ambient temperature for an additional 24 hours following the boil. Each specimen was then suspended in a bath of distilled water using the Archimedes' test apparatus and the suspended mass (*S*) was recorded. Finally, the saturated mass (*M*) of each specimen was recorded and the apparent porosity and bulk density of each specimen was calculated using Equations 3.2-3.8. In these equations, V is the exterior volume, V_{OP} is the volume of the open pores, V_{IP} is the volume of the impervious portions, P is the apparent porosity (in percent), A is the water absorption (in percent), T is the apparent specific

gravity and *B* is the bulk density in g/cm^3. During these calculations, the assumption is made that the density of water at room temperature is 1 g/cm^3 as specified by ASTM [46].

$$V = M - S \tag{3.2}$$

$$V_{OP} = M - D \tag{3.3}$$

$$V_{IP} = D - S \tag{3.4}$$

$$P = 100\left[\frac{(M - D)}{V}\right] \tag{3.5}$$

$$A = 100\left[\frac{(M - D)}{D}\right] \tag{3.6}$$

$$T = \frac{D}{D - S} \tag{3.7}$$

$$B = \frac{D}{V} \tag{3.8}$$

3.2. Mechanical Property Evaluation

3.2.1. Specimen Geometry

The optical micrographs in Figure 5 are representative of two batches of compression specimens following densification. The specimen in Figure 5a-c was fired at a peak temperature of 1300°F (~705°C), while the specimen in Figure 5d-f was fired at 1450°F (790°C).

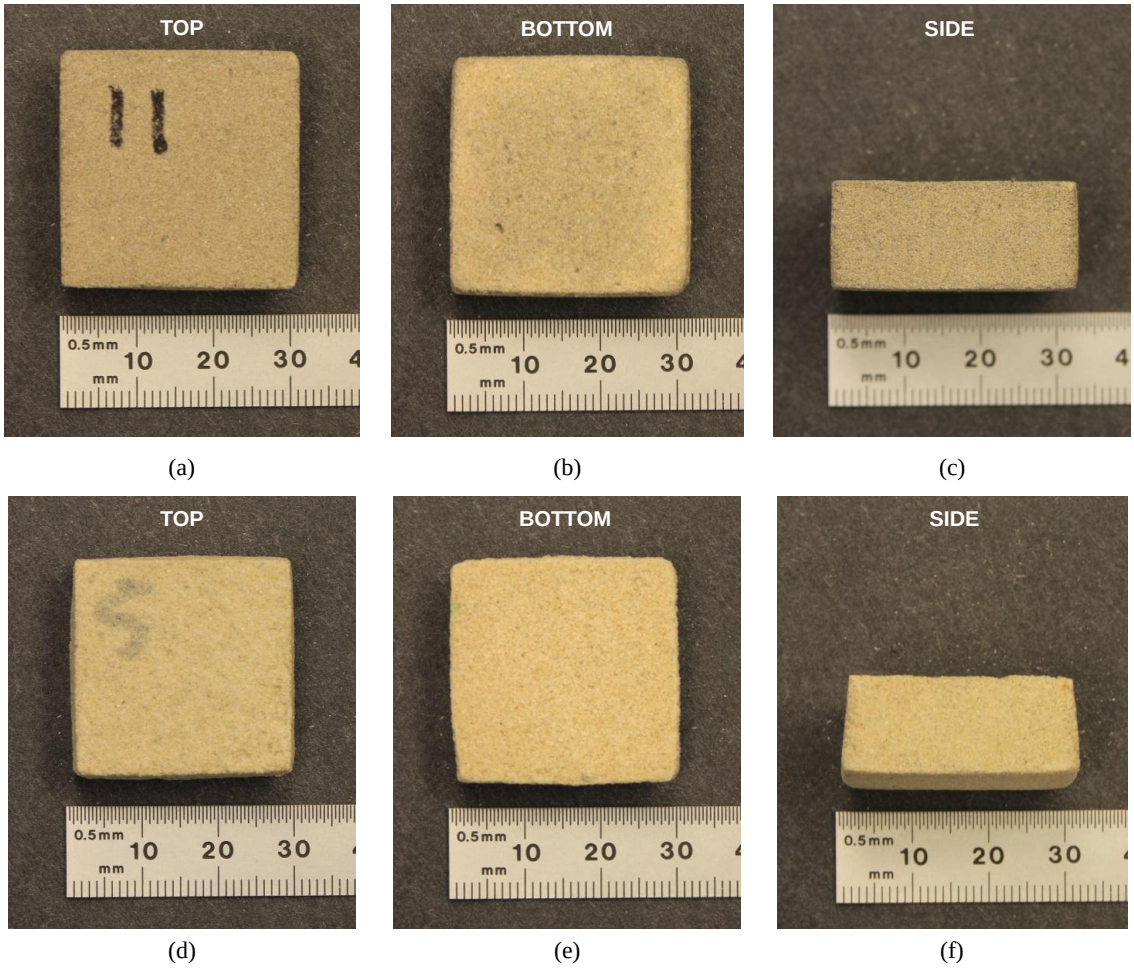

Figure 5. Compression specimen after densification. (a-c) Fired at peak temperature of 1300°F (~705°C). (d-f) Fired at peak temperature of 1450°F (~790°C).

Visual inspection of the two specimens indicates that the specimen fired at 705°C appears to have undergone negligible dimensional distortion. The edges and face remained relatively planar and square after densification. A similar inspection of the specimen fired at 790°C shows considerable dimensional distortion along all three axes. From the side view the specimen is trapezoidal.

The optical micrographs in Figures 6 are representative of two batches of flexure specimens following densification. The specimen in Figure 6a-c was fired at a peak temperature of 1300°F (~705°C), while the specimen in Figure 6d-f was fired at 1450°F (790°C).

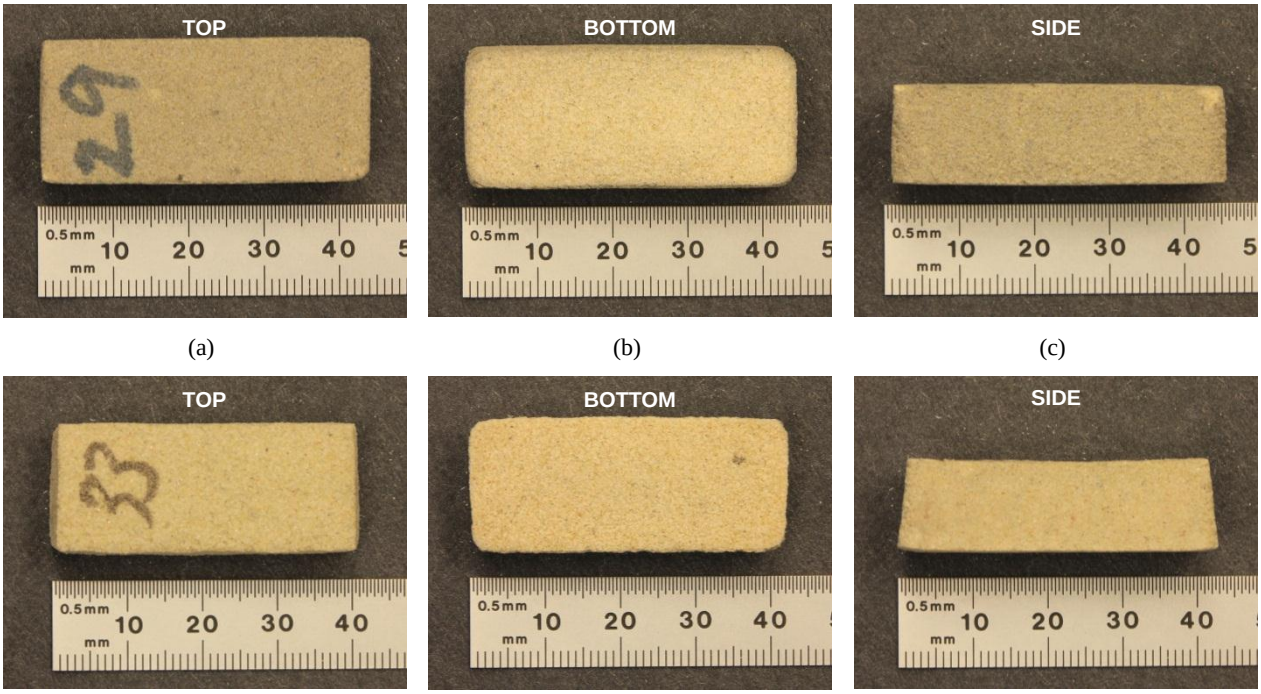

Figure 6. Flexure specimen after densification. (a-c) Fired at peak temperature of 1300°F (~705°C). (d-f) Fired at peak temperature of 1450°F (~790°C).

Visual comparison of the two specimens follows the same pattern as was observed for the compression specimens. As the peak firing temperature is increased, specimens undergo a higher degree of dimensional distortion. This seems to be more pronounced in the flexure specimens.

3.2.2. Experimental Setup & Procedures

3.2.2.1. Compression Test System: Compressive testing took place using an INSTRON 5585H series floor model load frame equipped with a 250 kN load cell. To the extent that was possible, compressive testing took place in accordance with ASTM testing standards for structural ceramics [47]. Specimens were placed on a spherically seated bottom bearing surface, which was free to rotate in the longitudinal and transverse directions as shown in Figure 7.

Figure 7. INSTRON 5585H outfitted with spherically seated bottom bearing plate.

Once the specimen was centered upon the bottom bearing surface, a preload of one pound was applied. The load was applied in two stages as per ASTM [47]. During the first stage, testing was performed at a speed of 0.1 in/min (2.54 mm/min) until an applied load of one half the expected maximum value was reached. During the second stage, the speed of testing was reduced by 50% (1.27 mm/min). Experimental data, including engineering stress, engineering strain, maximum compressive load and maximum compressive stress, were acquired through the Bluehill2 software package.

In calculating the elastic modulus in compression the stress-strain data was manipulated to include only the most linear portion of the curve. Inspection of the stress-strain curves revealed that linear elastic behavior began primarily after 40%, but before 80%, of the maximum stress was achieved. Once the data was truncated to include only this portion of each stress-strain

curve, Equation 2.8 was then used to calculate the modulus of elasticity. These calculations were performed in MATLAB and the code is shown in Appendix A.

3.2.2.2. Flexure Test System: Flexural testing took place using the INSTRON 5585H as before. To the extent that was possible, testing took place in accordance with ASTM testing standards for structural ceramics, which is published in English units[47, 48]. The 3-point bending test fixture is shown in Figure 8, with and without a specimen loaded. The rate of testing was held constant throughout all batches tested at an extension speed of 0.05 inches per minute (1.27 mm/min). Experimental data, including engineering stress, engineering strain, maximum transverse load and transverse stress, were acquired through the Bluehill software package.

(a) (b)

Figure 8. Experimental setup for 3-point bending test. (a) Test fixture (b) Flexure specimen positioned in fixture.

3.2.2.3. Experimental Procedure: Specimens were prepared in batches of 20 and the peak firing temperature during densification was varied from 705°C to 790 °C. After testing was complete, batch data was analyzed through the Weibull approach, which has been used widely in the field of fracture, particularly in brittle materials. The theory behind this model is that the specimen

will fail when its weakest element fails and it is the preferred method for analyzing strength and fatigue data in ceramics and other brittle materials.

In analyzing the data through the Weibull approach a probability plot was first constructed for each batch of data [49]. This provides three important pieces of information. First if the data can be fit reasonably well with a linear equation, this justifies the use of the two parameter Weibull distribution. Second, the slope of the line describes the degree of variability in the data set and is termed the shape factor or Weibull modulus. Third, the Weibull characteristic strength or scale factor is defined as the strength at which the probability of failure is 63.2%.

Using this information the Weibull probability density function, cumulative distribution function, mean and standard deviation can be calculated. The Weibull probability density function (PDF) is given by Equation 3.9, where *a* is defined as the scale parameter and *b* is defined as the shape parameter. The Weibull cumulative distribution function (CDF) is given by Equation 3.10, which can be derived through integration of the PDF. The Weibull mean and standard deviation are given by Equations 3.11 and 3.12 respectively. All Weibull calculations were performed in MATLAB and the code is shown in Appendix A.

$$f(x|a,b) = \frac{b}{a}\left(\frac{x}{a}\right)^{b-1} e^{-(x/a)^b} \tag{3.9}$$

$$F(x|a,b) = 1 - e^{-(x/a)^b} \tag{3.10}$$

$$\mu = a[\Gamma(1 + b^{-1})] \tag{3.11}$$

$$\sigma = \sqrt{a^2[\Gamma(1 + 2b^{-1}) - \Gamma(1 + b^{-1})]^2} \tag{3.12}$$

CHAPTER 4. RESULTS

4.1. PHYSICAL PROPERTY EVALUATION

4.1.1. VOLUMETRIC SHRINKAGE

Once the dimensional measurement data was collected, the volumetric shrinkage in each batch was compared to the peak firing temperature, as seen in Figure 9.

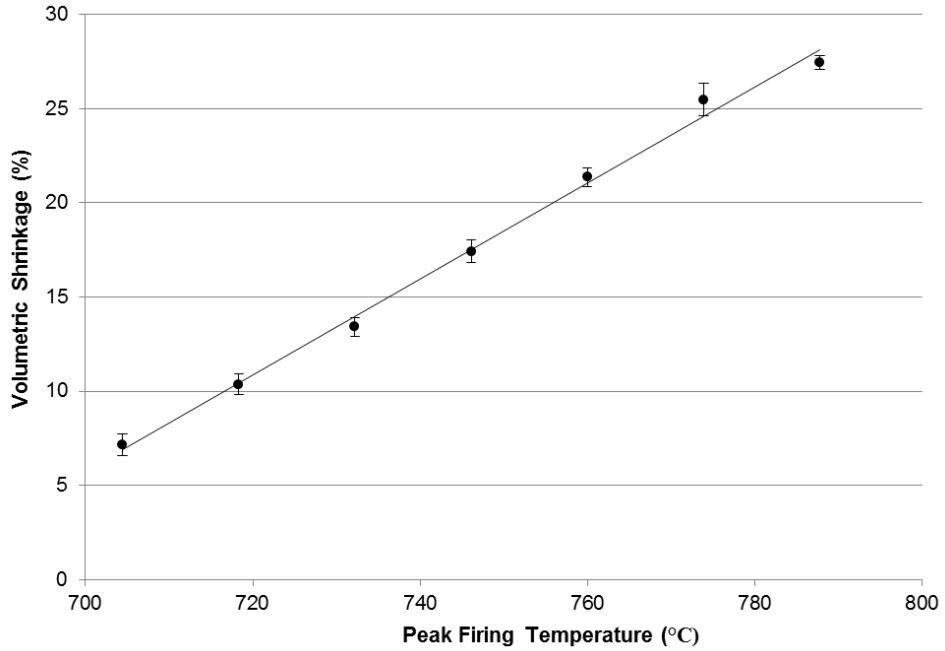

Figure 9. Relationship between peak firing temperature and volumetric shrinkage.

Each data point in the plot above represents the arithmetic mean of 20 compression specimens and 20 flexure specimens. Variation in each batch is shown by the vertical error bars, which represent the arithmetic standard deviation. Figure 9 shows that, when peak firing temperatures are varied within 705 and 790°C range, the volumetric shrinkage and the peak firing temperature are linearly related.

4.1.2. APPARENT POROSITY

Analysis of the specimens via the Archimedes' method resulted in mean values of apparent porosity ranging from ~6.8 to ~35.4% and bulk density ranging from ~1.5 to ~2.1 g/cm^3. Volumetric shrinkage is compared with apparent porosity in Figure 10.

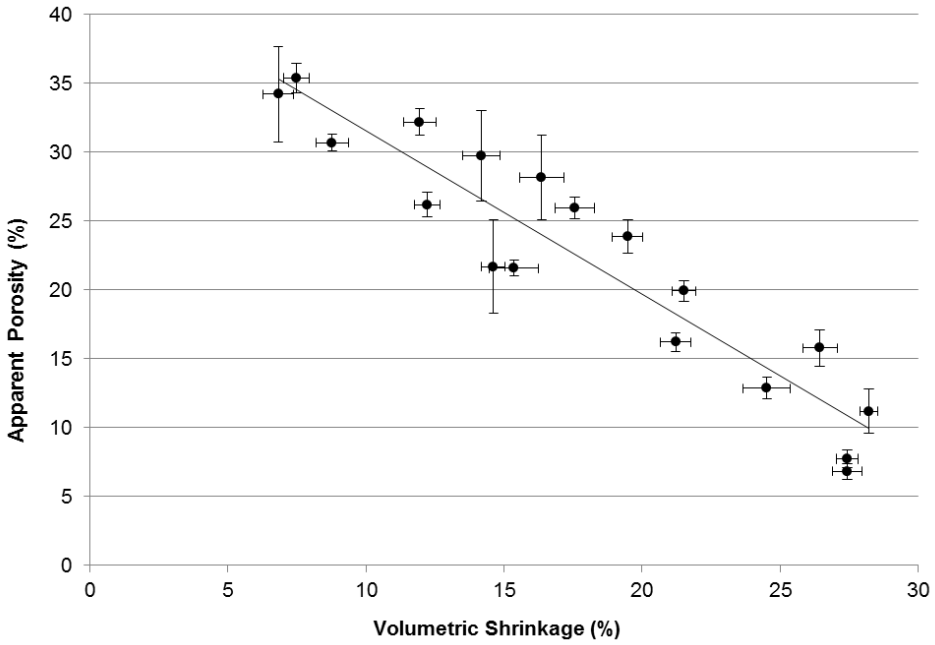

Figure 10. Comparison of measured volumetric shrinkage due to firing and resulting apparent porosity.

The data points represent the arithmetic mean of 20 specimens. Variation present in the apparent porosity is shown by the vertical error bars, which represent the arithmetic standard deviation for each batch. The horizontal error bars represent the standard deviation in volumetric shrinkage. In this particular temperature range, it appears that apparent porosity has a linear relationship with the volumetric shrinkage that results from the densification process; however, the data is somewhat scattered. In addition, the standard deviation in apparent porosity is considerably higher in four of the batches.

This behavior appears to be most prevalent around 15% volumetric shrinkage, which correlates to peak firing temperatures of ~740°C (Figure 9). This temperature corresponds to the onset of crystallization in soda-lime silicate glasses. Because of the variability in composition of the feedstock, some of the particles may have begun to crystallize while others have not. This may have contributed to larger variation in apparent porosity observed near 15% volumetric shrinkage.

4.1.3. Bulk Density

The bulk density of the specimens as it relates to apparent porosity is shown in Figure 11. The vertical and horizontal error bars represent the standard deviation in bulk density and apparent porosity respectively.

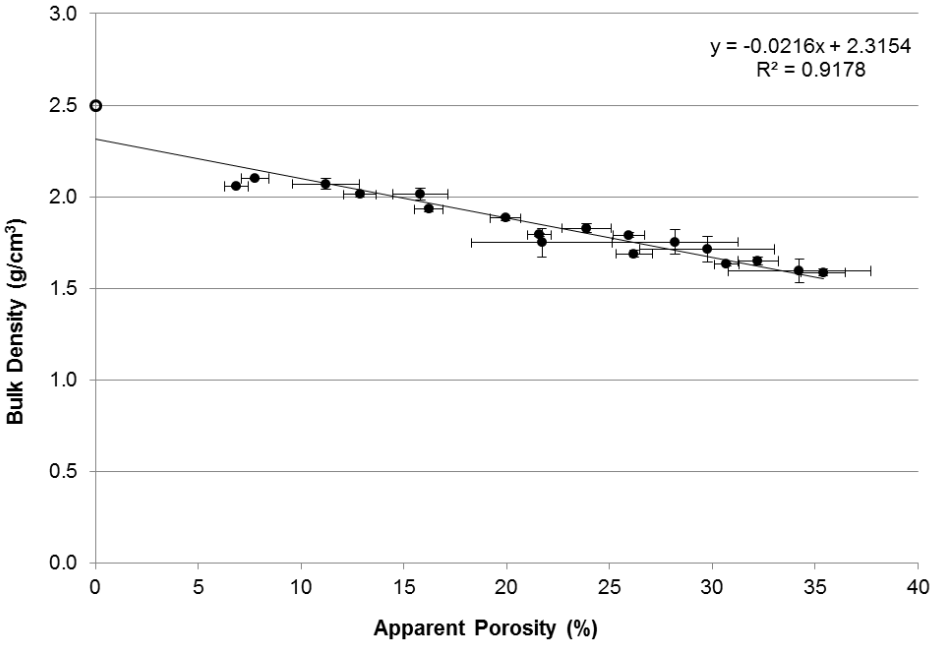

Figure 11. Relationship between apparent porosity and bulk density**.** Circle on y-axis represents the mean of published values for the zero porosity density of soda-lime silicate glass.

The single circle on the Y-axis represents the average of published values for the bulk density of zero porosity soda-lime silicate glass (Table 2). It appears that bulk density and apparent porosity are related linearly, as expected. Further, the experimentally obtained values are in good agreement with published zero porosity values.

4.2. Compressive Behavior

4.2.1. Stress-Strain Behavior Under Compression

The stress-strain behavior of the seven batches of compressive specimens can be seen on the next few pages in Figures 12-18. The data is grouped in batches and is shown in order of descending apparent porosity, which was between 6.8 and 35.4%.

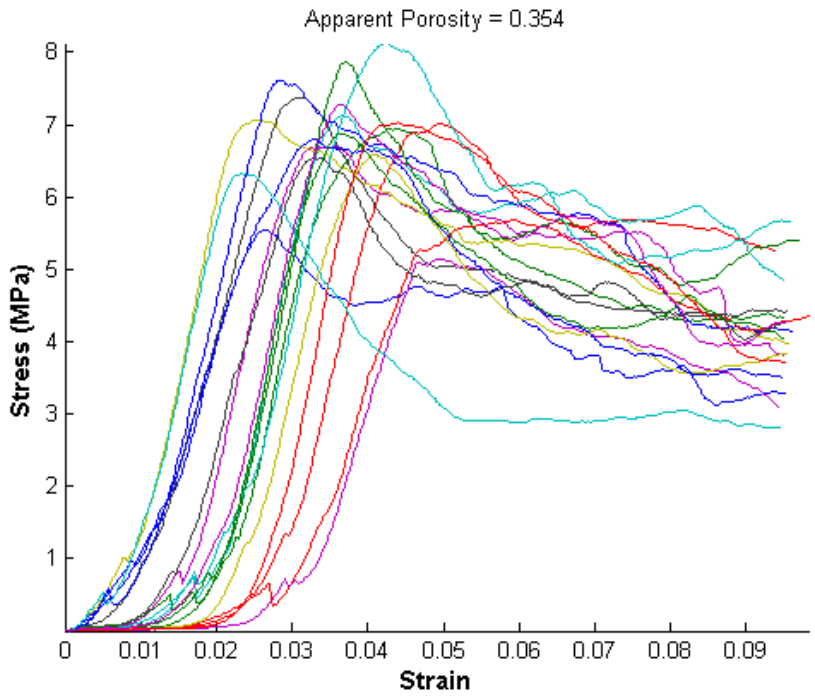

Figure 12. Compressive stress vs. compressive strain: 35.4% apparent porosity

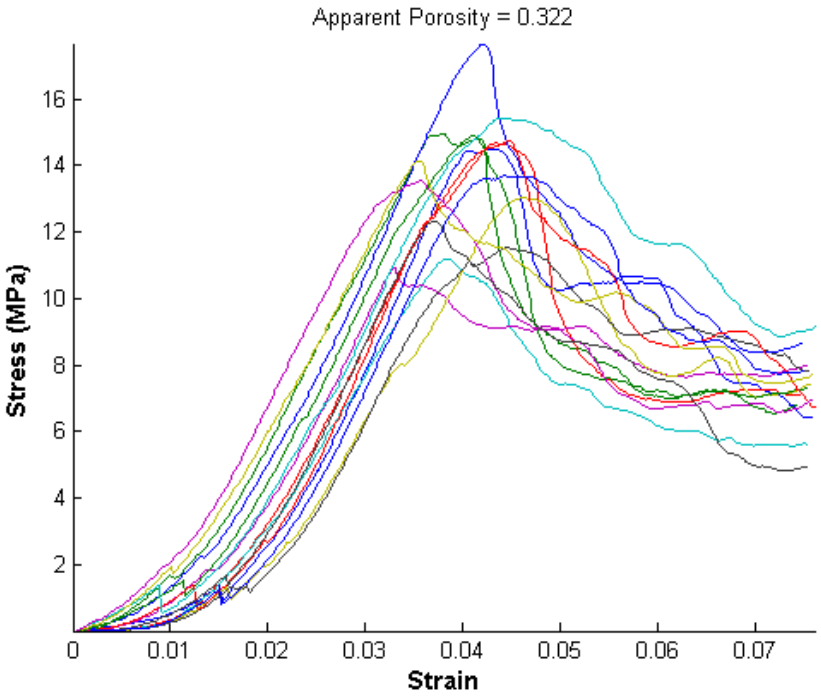

Figure 13. Compressive stress vs. compressive strain: 32.2% apparent porosity.

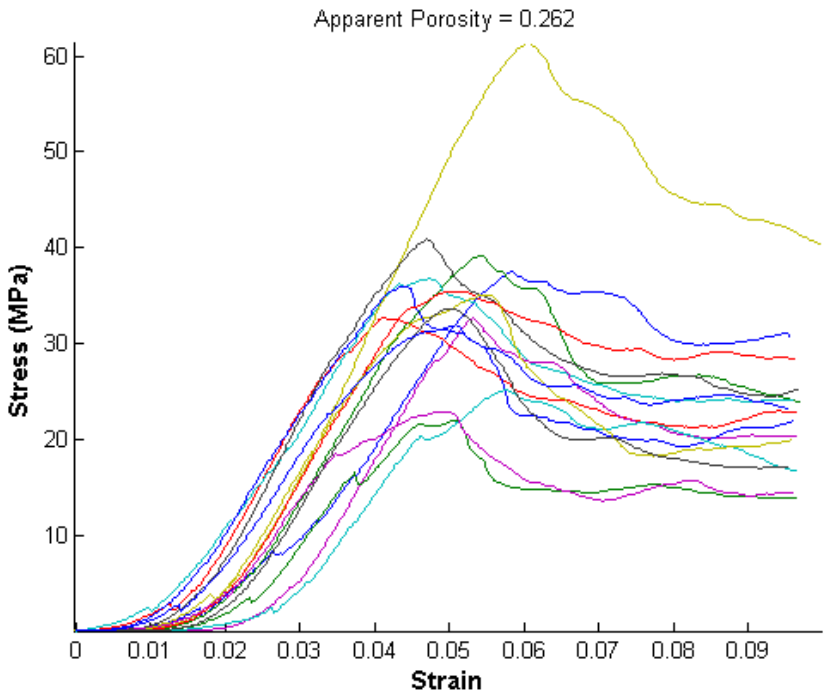

Figure 14. Compressive stress vs. compressive strain: 26.2% apparent porosity.

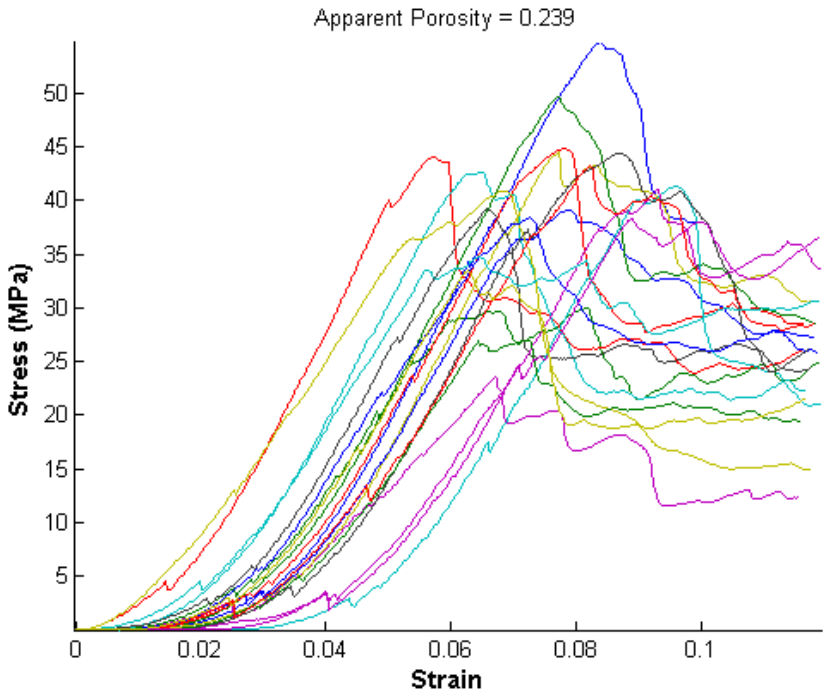

Figure 15. Compressive stress vs. compressive strain: 23.9% apparent porosity.

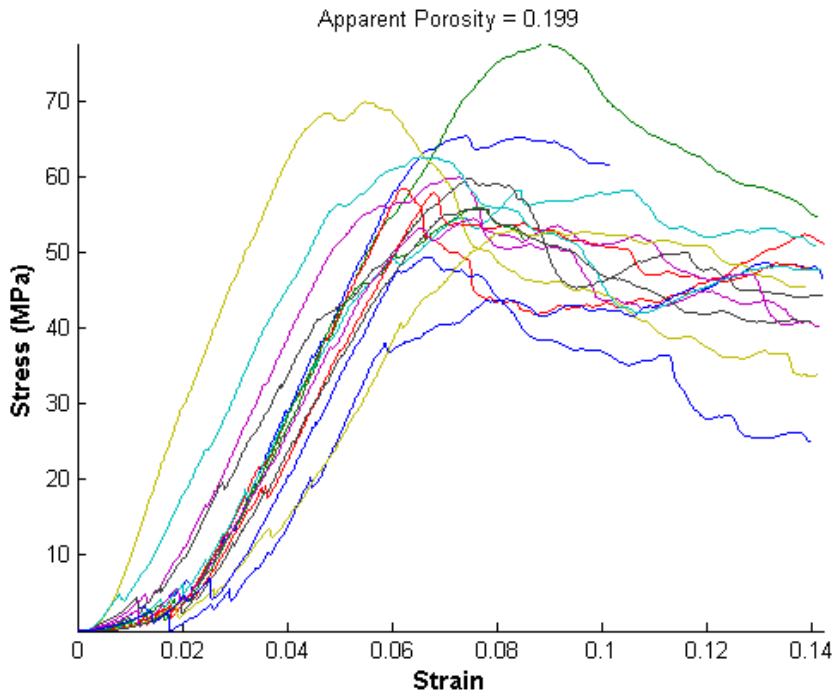

Figure 16. Compressive stress vs. compressive strain: 19.9% apparent porosity.

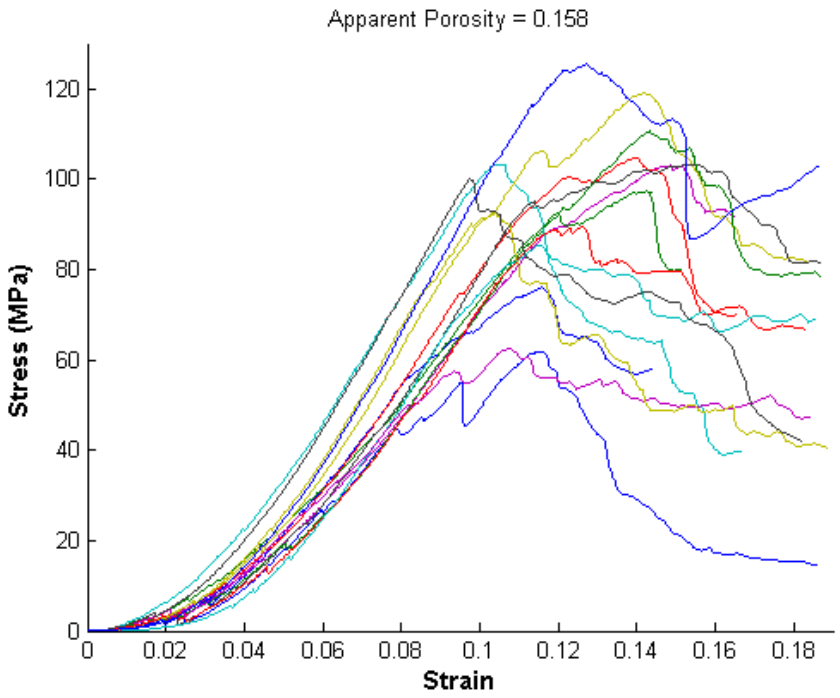

Figure 17. Compressive stress vs. compressive strain: 15.8% apparent porosity.

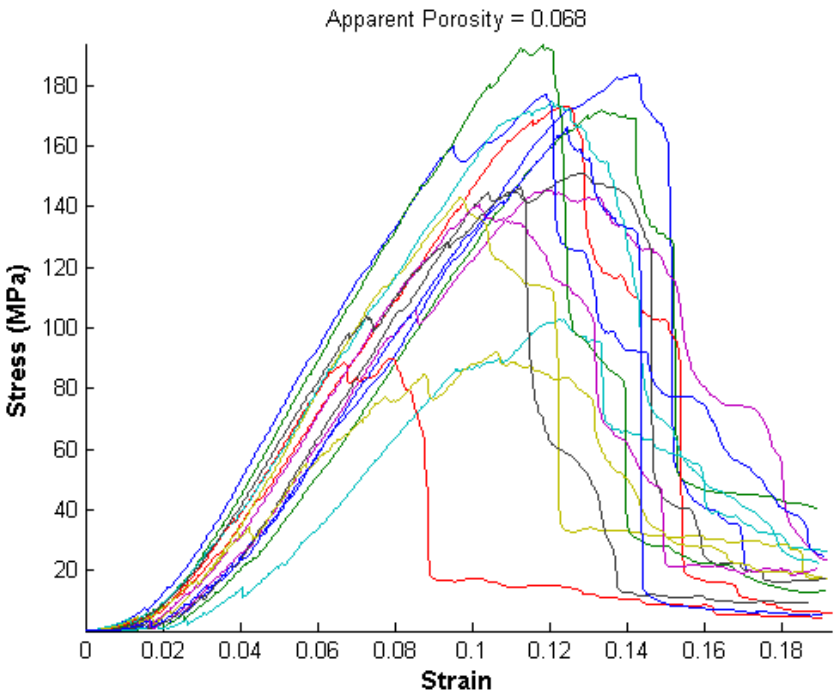

Figure 18. Compressive stress vs. compressive strain: 6.8% apparent porosity.

From Figures 12-18 it can be seen that within each batch, the specimens behave similarly through the elastic portion of the curves. It should be noted that during initial loading the stress-strain behavior appears to be non-linear. This is somewhat common in porous materials; as the load is applied, dynamic modifications in the structure of the particles and the pore system may occur. Inspection of the stress-strain curves also shows that the maximum stress exhibited by specimens in a given batch can vary considerably. Further, in batches exhibiting mean apparent porosity higher than ~20%, the specimens generally appear to lose 40-50% of their strength once the strain reaches approximately twice the value observed at the point of maximum stress. In batches exhibiting less that ~20% porosity the behavior is quite different.

At 15.8% apparent porosity the stress-strain data is quite scattered after maximum stress is achieved. At 6.8% apparent porosity the strength drops dramatically after maximum stress is

achieved. In fact at 6.8% apparent porosity, stress appears to be negligible once strain has reached twice the value observed at the point of maximum stress.

4.2.2. Elastic Modulus Under Compression

In order to evaluate the elastic modulus, the stress-strain curves were truncated as described in Section 3.2.2.1. The linear portion of the stress-strain curves can be seen in Figures 19-25. Again the results are shown in order of descending porosity: 6.8-35.4%.

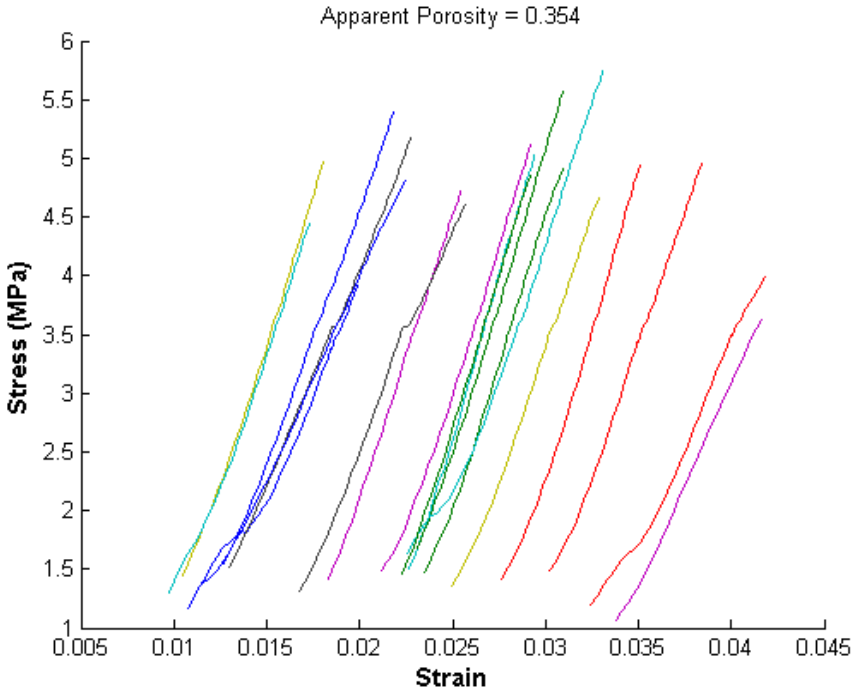

Figure 19. Portion of the stress-strain curve used in calculating the elastic modulus in compression: 35.4% apparent porosity.

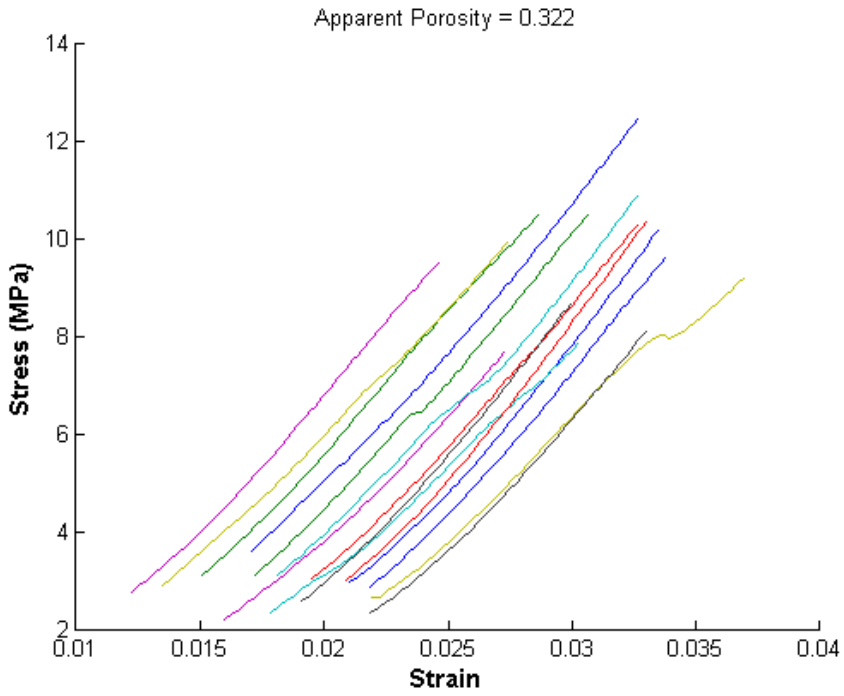

Figure 20. Portion of the stress-strain curve used in calculating the elastic modulus in compression: 32.2% apparent porosity.

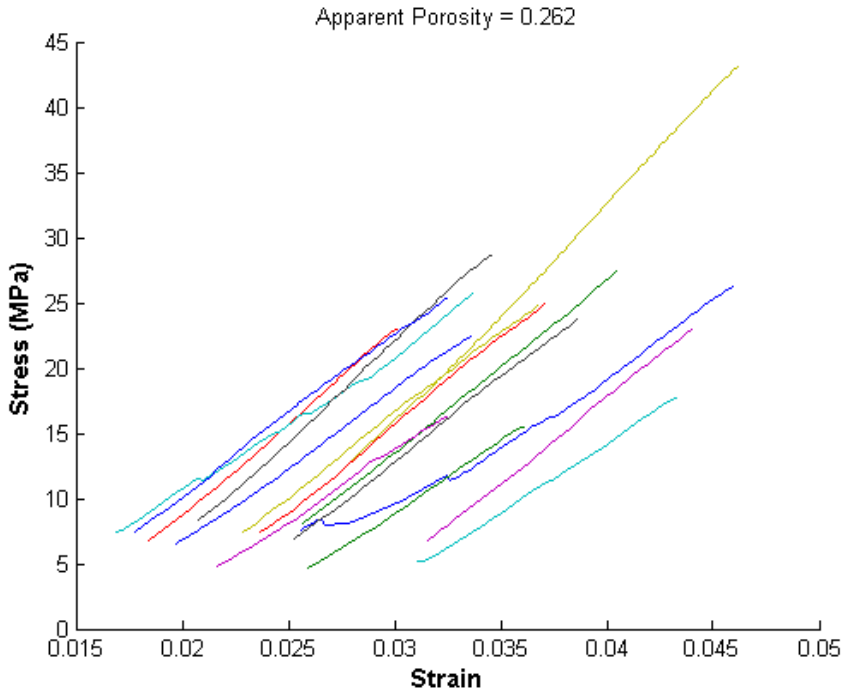

Figure 21. Portion of the stress-strain curve used in calculating the elastic modulus in compression: 26.2% apparent porosity.

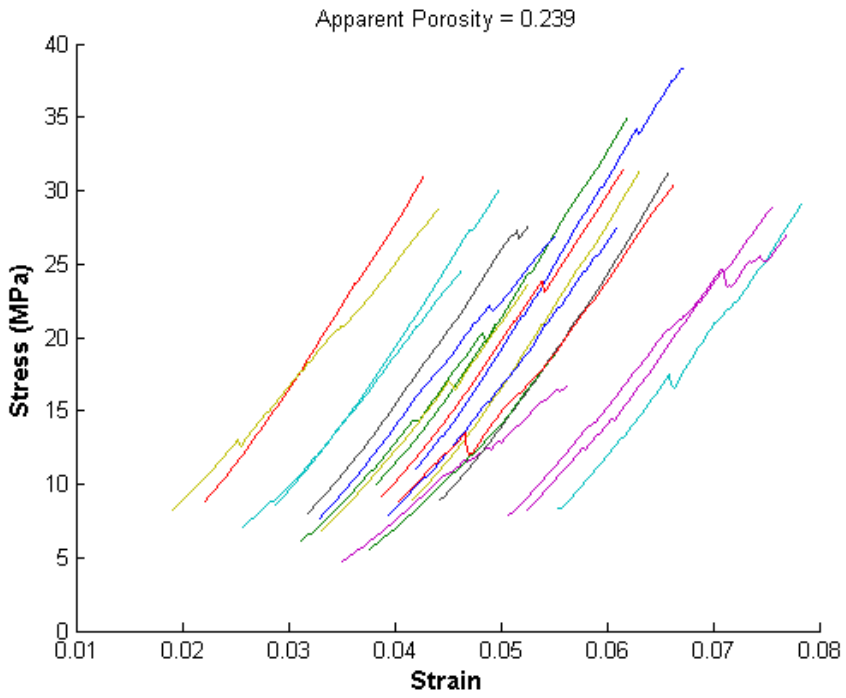

Figure 22. Portion of the stress-strain curve used in calculating the elastic modulus in compression: 23.9% apparent porosity.

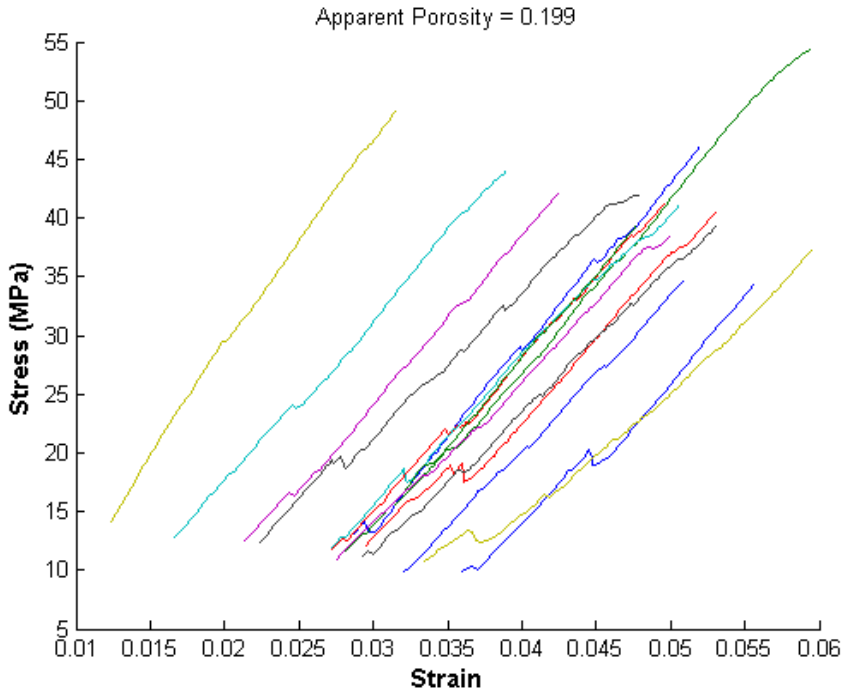

Figure 23. Portion of the stress-strain curve used in calculating the elastic modulus in compression: 19.9% apparent porosity.

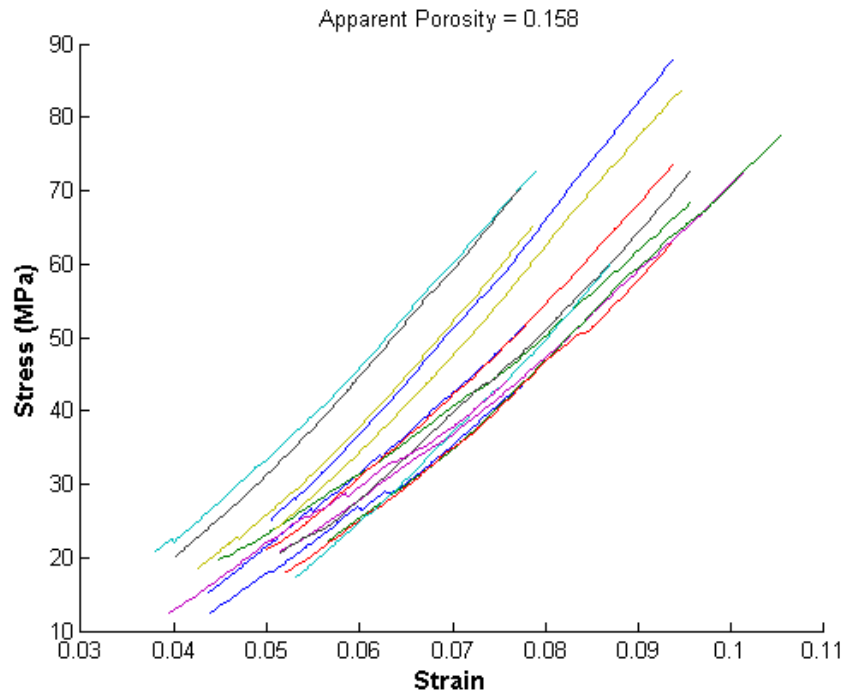

Figure 24. Portion of the stress-strain curve used in calculating the elastic modulus in compression: 15.8% apparent porosity.

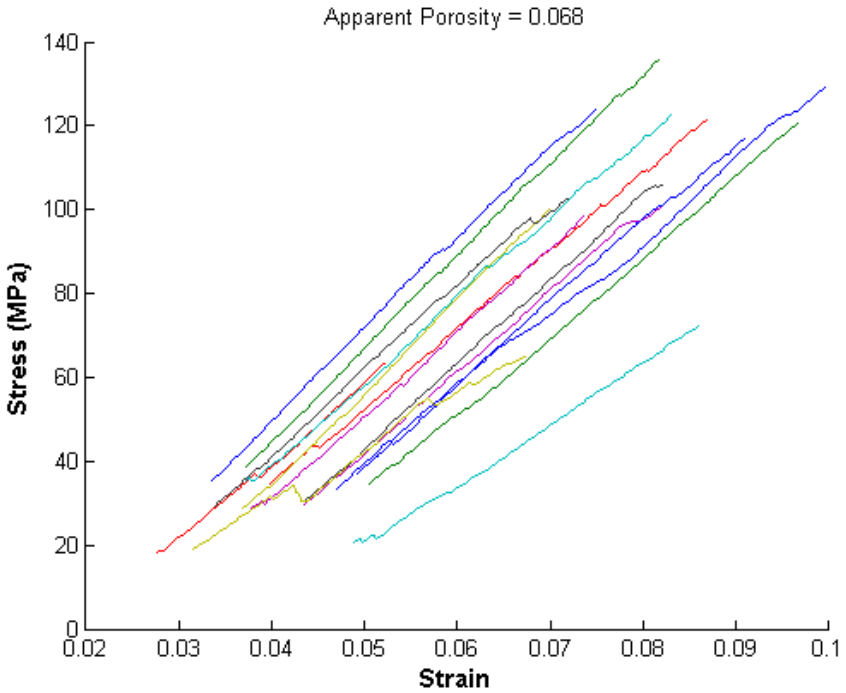

Figure 25. Portion of the stress-strain curve used in calculating the elastic modulus in compression: 6.8% apparent porosity.

Although the elastic portion of compressive stress-strain curves can be characterized by being generally linear, in almost all cases, they can also be characterized by discontinuities and load drops.

4.2.3. WEIBULL CHARACTERISTICS

The results of Weibull analysis are summarized in Table 3 and Weibull probability plots are shown in Appendix B. The tabulated data shows that the mean compressive strength ranges from 6.82 to 150.83 MPa and values for the Weibull modulus vary from 3.79 to 11.08.

Table 3. Summary of Weibull data for compressive strength.

Apparent Porosity	Mean (MPa)	Std. Dev. (MPa)	Scale Factor (MPa)	Modulus
0.0683	150.8232	28.8636	162.4528	6.0817
0.1579	95.8558	17.2735	102.8817	6.4909
0.1994	58.7336	9.0505	62.4912	7.6821
0.2387	39.7263	7.2634	42.6742	6.3898
0.2619	34.6224	10.1872	38.3112	3.7945
0.3221	13.7630	1.9455	14.5782	8.4248
0.3539	6.8241	0.7449	7.1429	11.0823

Once the data was analyzed through the Weibull approach, the cumulative distribution function for each of the seven batches of compressive specimens was calculated. The CDF plots are shown in Figures 26-32. In each of the figures the experimental data is denoted by blue x's, the Weibull CDF is denoted by the solid red line and the 95% upper and lower confidence bounds are denoted by the dashed red lines.

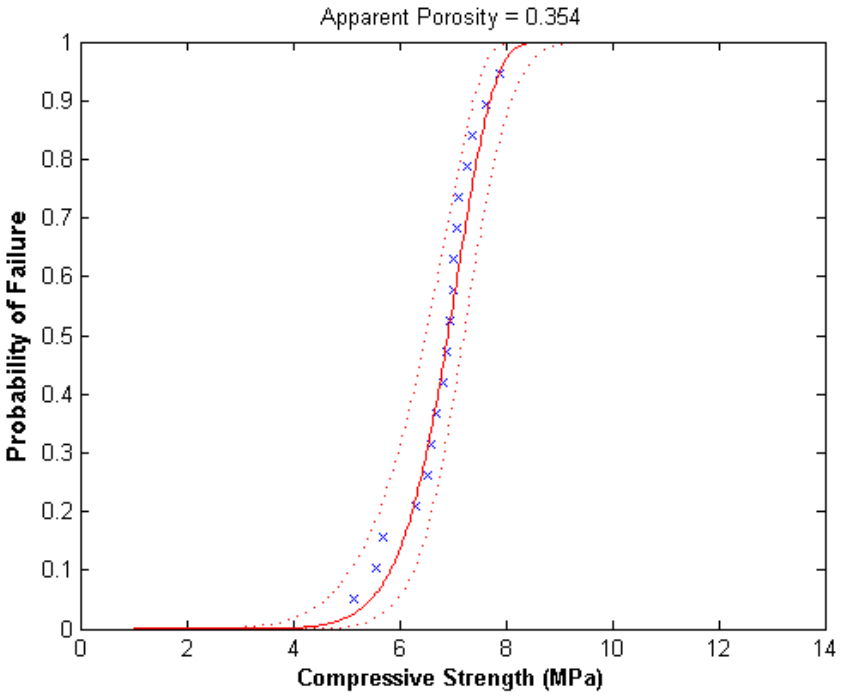

Figure 26. Weibull CDF for compressive strength at 35.4% apparent porosity.

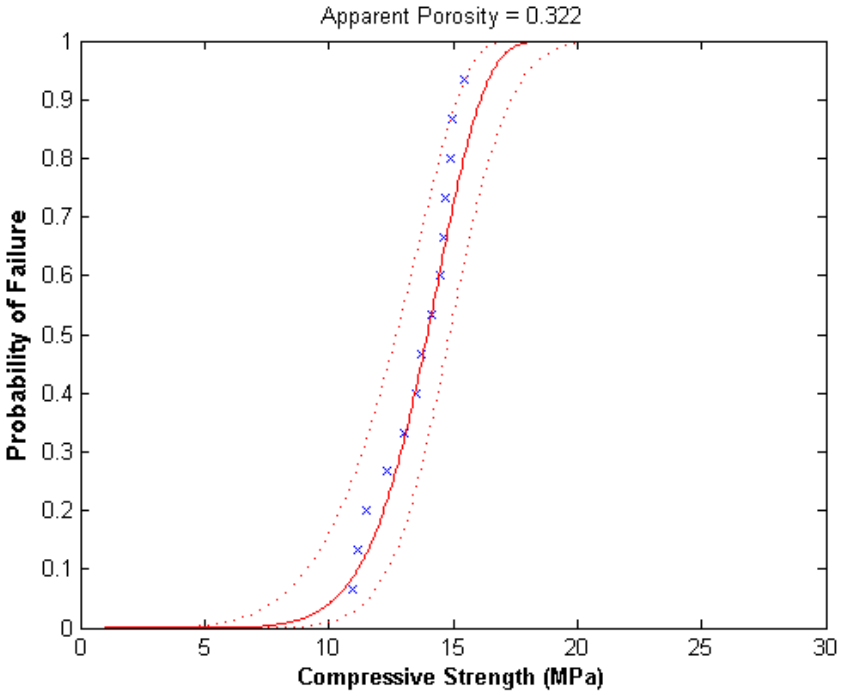

Figure 27. Weibull CDF for compressive strength at 32.2% apparent porosity.

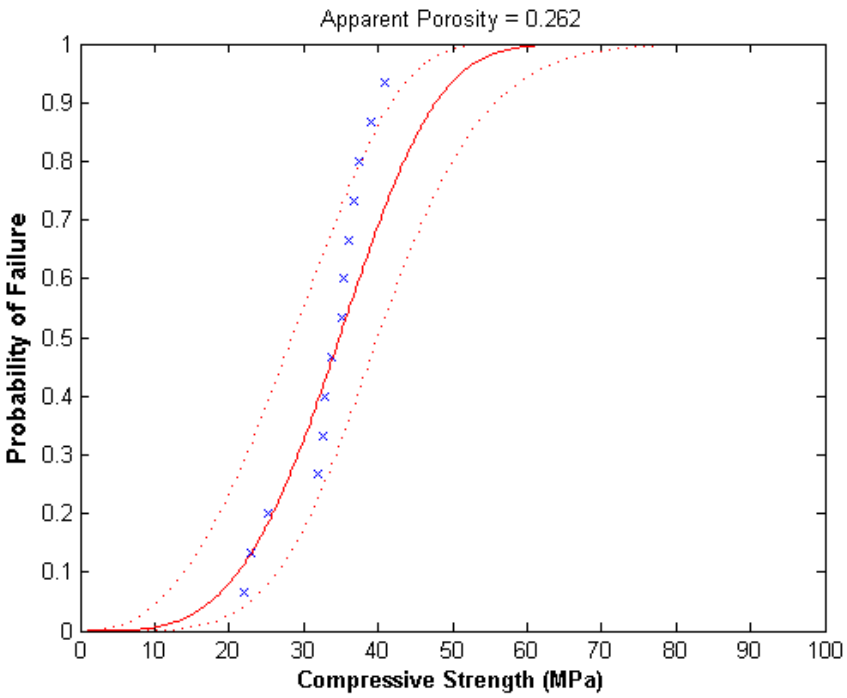

Figure 28. Weibull CDF for compressive strength at 26.2% apparent porosity.

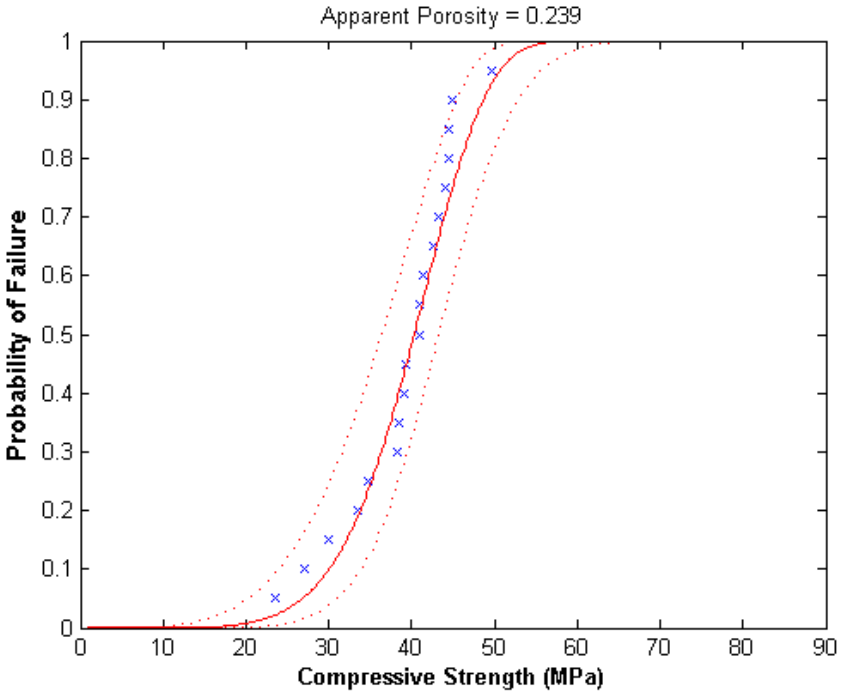

Figure 29. Weibull CDF for compressive strength at 23.9% apparent porosity.

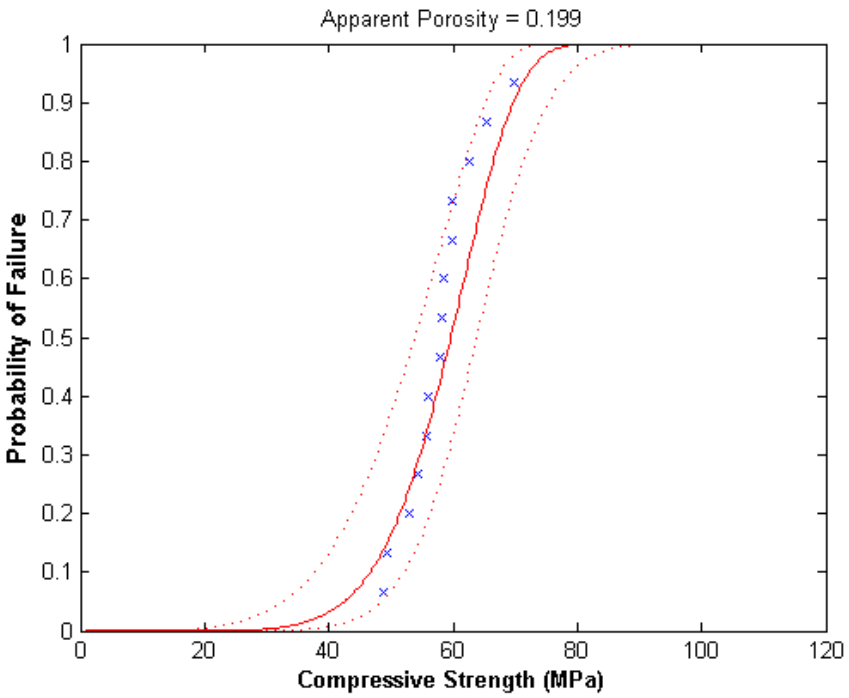

Figure 30. Weibull CDF for compressive strength at 19.9% apparent porosity.

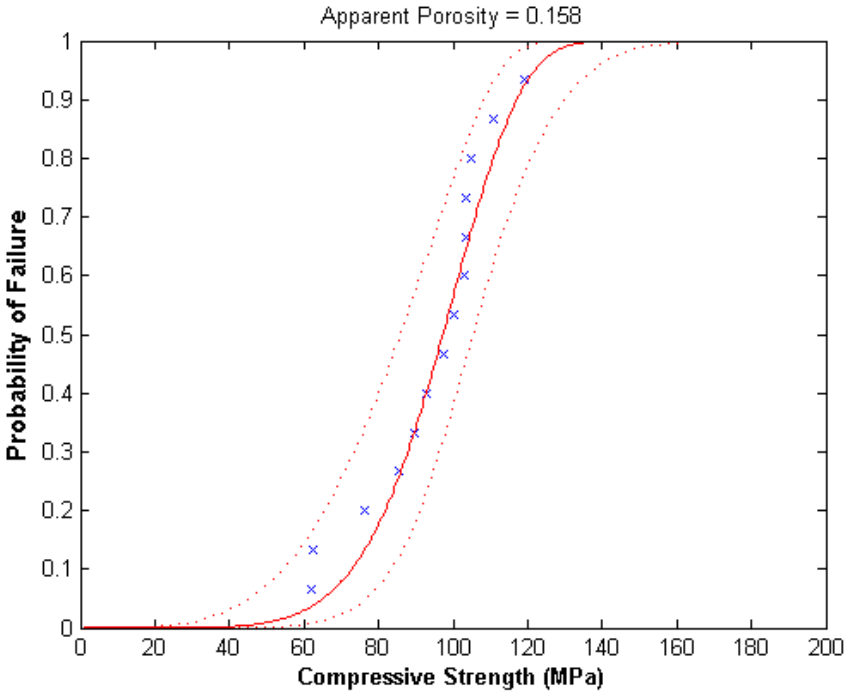

Figure 31. Weibull CDF for compressive strength at 15.8% apparent porosity.

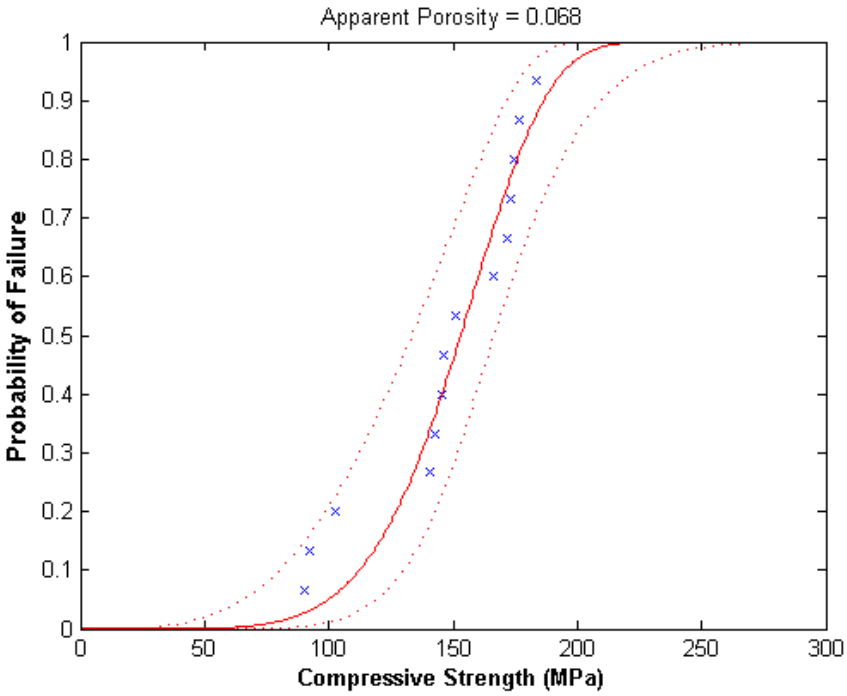

Figure 32. Weibull CDF for compressive strength at 6.8% apparent porosity.

The Weibull analysis data for each batch of compression specimens is compared graphically in Figures 33 and 34 on the following page. In Figure 33 the mean compressive strength is plotted against the mean porosity. In Figure 34 the Weibull modulus, or shape factor is plotted against mean apparent porosity.

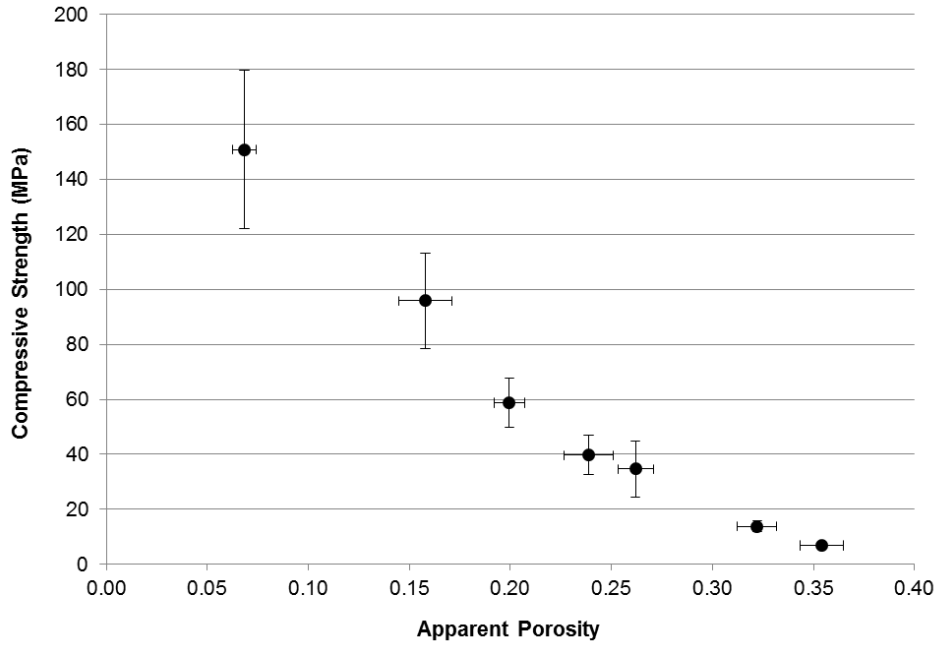

Figure 33. Mean compressive strength as a function of porosity.

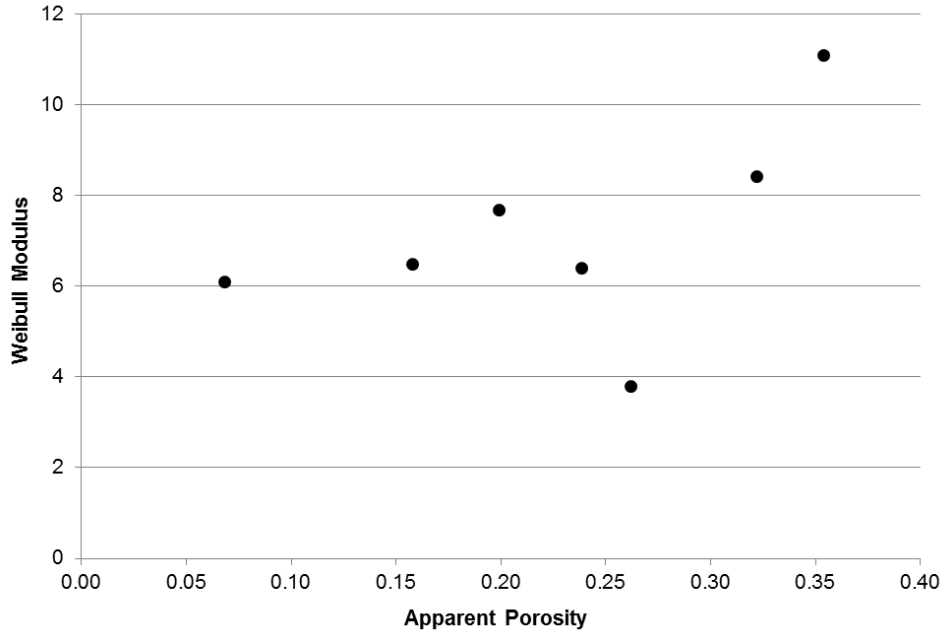

Figure 34. Weibull Modulus for compressive strength as a function of apparent porosity.

In Figure 33 the vertical error bars represent the Weibull standard deviation in strength, while the horizontal error bars represent the arithmetic standard deviation in apparent porosity. As expected, the mean strength was observed to increase with decreasing apparent porosity.

Figure 33 also shows that the standard deviation in compressive strength increases as the apparent porosity decreases. In addition, the standard deviation in compressive strength at 26.2% apparent porosity appears to be unusually large.

Although the standard deviation is a useful metric in measuring the variation between specimens in a batch, the Weibull modulus is generally a better indicator. This non-dimensional number correlates to the slope of the Weibull CDF and a larger value indicates less variation. In Figure 34 no trend in the data can be readily observed. In most cases the Weibull modulus for the compressive data is between six and eight; however, at higher apparent porosity the value of the Weibull modulus is less consistent. The lowest value for the Weibull modulus was calculated at 26.2% apparent porosity.

As with the strength versus porosity data, Weibull analysis was performed on the elastic modulus data. The results of the Weibull analysis are summarized in Table 4, which shows that mean values for the elastic modulus in compression range from 429.18 to 1902.88 MPa and values for the Weibull modulus vary from 6.74 to 13.88. The Weibull CDFs for each batch are shown in Figures 35-41.

Table 4. Summary of Weibull data for elastic modulus in compression.

Apparent Porosity	Mean (MPa)	Std. Dev. (MPa)	Scale Factor (MPa)	Modulus
0.0683	1902.8754	216.7266	1995.3692	10.5968
0.1579	1173.8136	183.6375	1249.9230	7.5583
0.1994	1328.6743	210.3062	1415.7156	7.4642
0.2387	920.2174	133.8807	976.1544	8.1695
0.2619	1251.6881	217.7025	1340.6929	6.7442
0.3221	544.4070	47.9993	565.2040	13.8677
0.3539	429.1786	66.8446	456.8972	7.5945

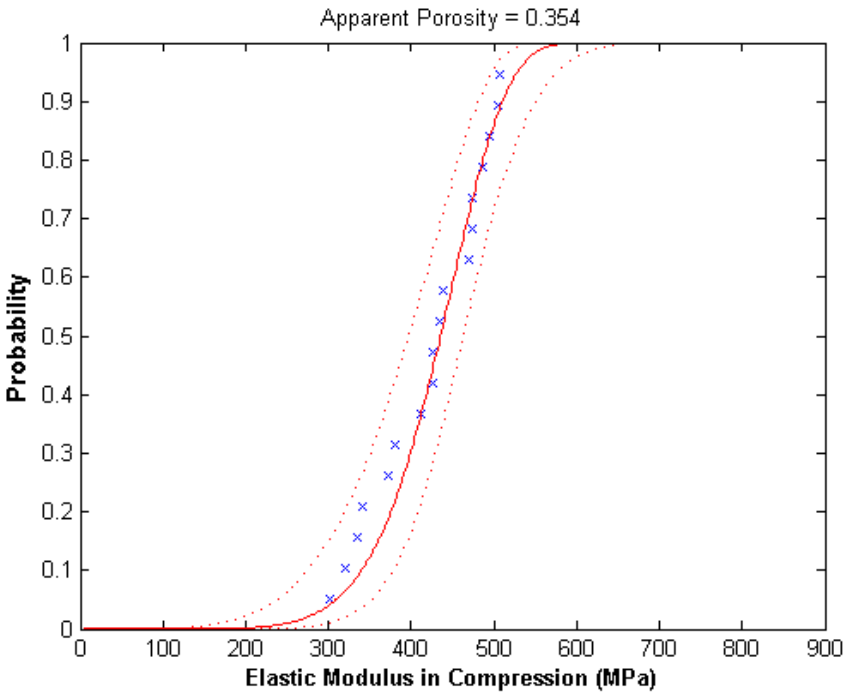

Figure 35. Weibull CDF for the elastic modulus in compression at 35.4% apparent porosity.

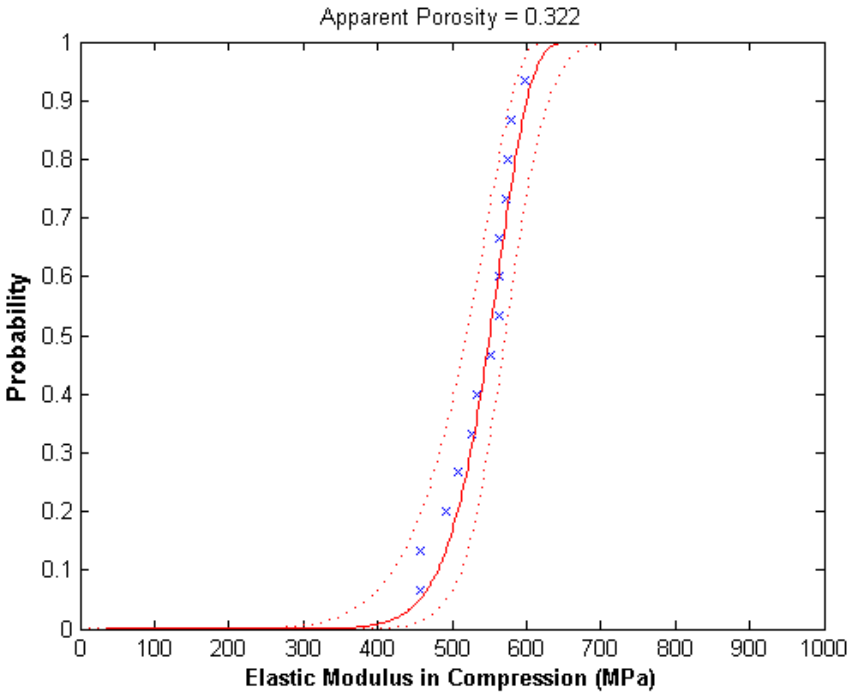

Figure 36. Weibull CDF for the elastic modulus in compression at 32.2% apparent porosity.

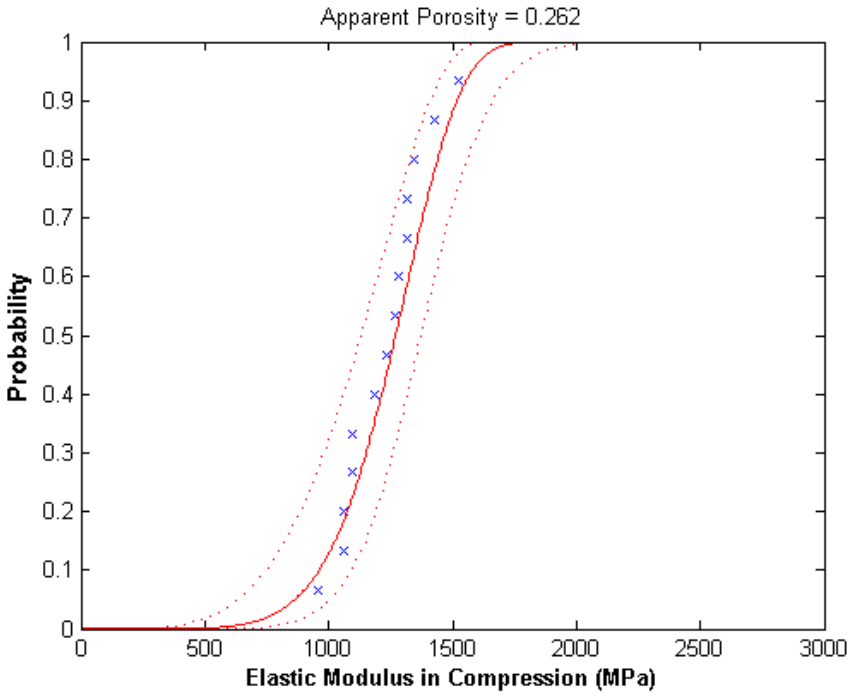

Figure 37. Weibull CDF for the elastic modulus in compression at 26.2% apparent porosity.

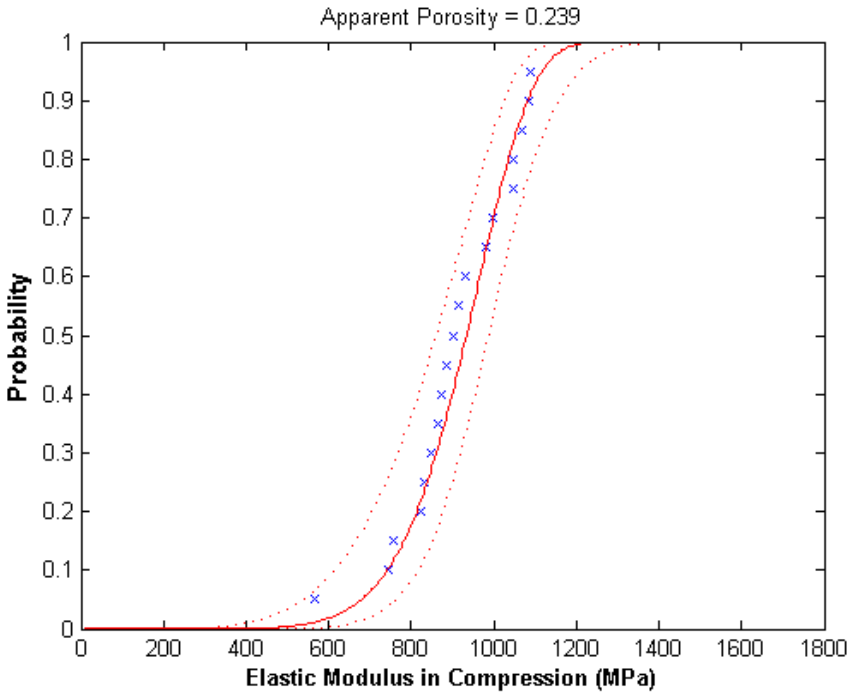

Figure 38. Weibull CDF for the elastic modulus in compression at 23.9% apparent porosity.

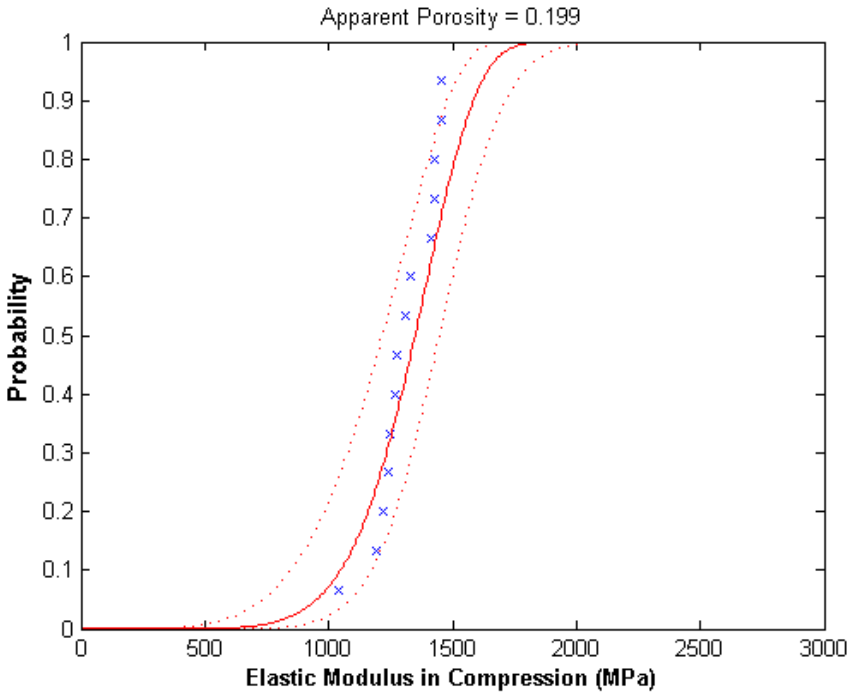

Figure 39. Weibull CDF for the elastic modulus in compression at 19.9% apparent porosity.

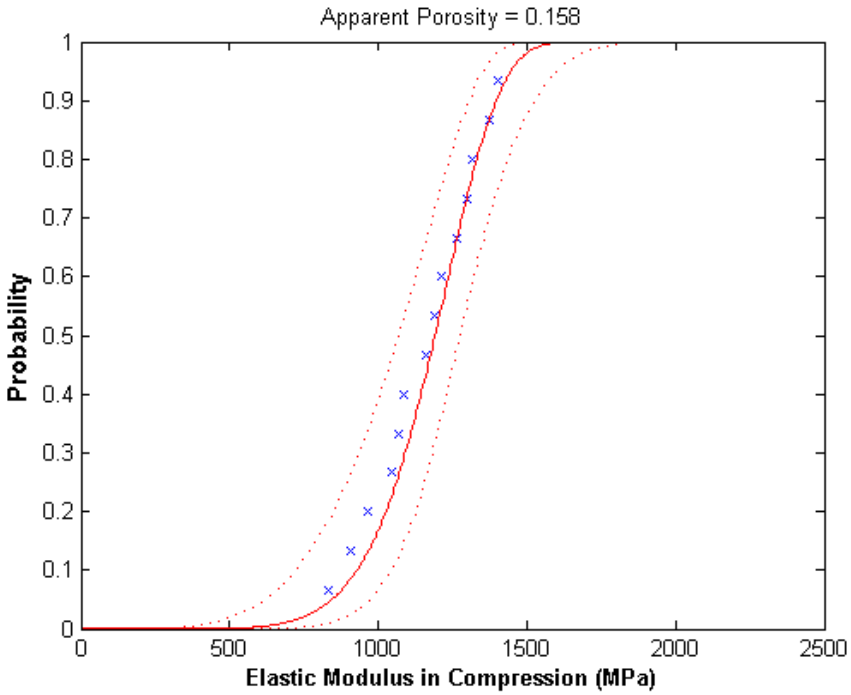

Figure 40. Weibull CDF for the elastic modulus in compression at 15.8% apparent porosity.

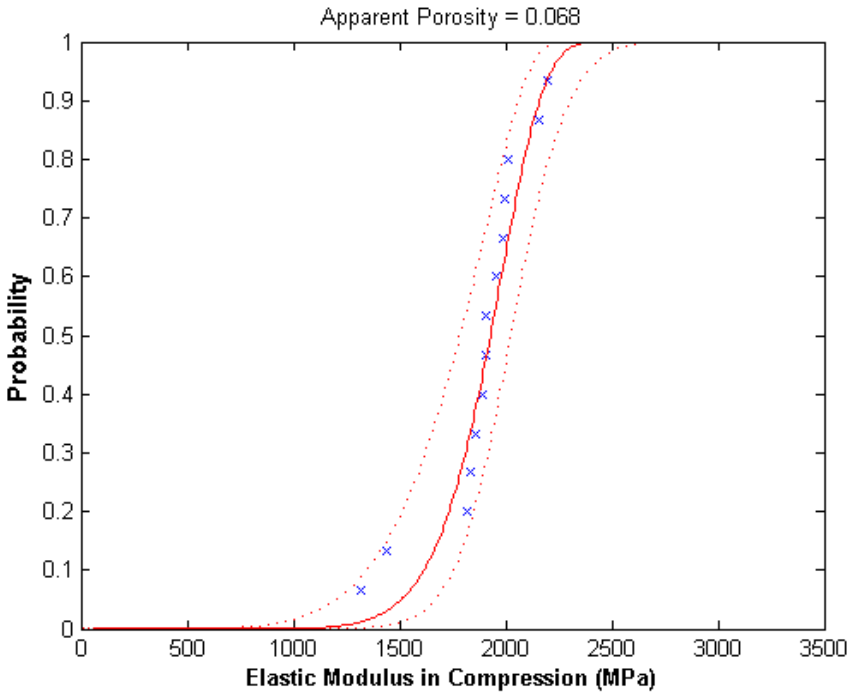

Figure 41. Weibull CDF for the elastic modulus in compression at 6.8% apparent porosity.

The Weibull analysis for the elastic modulus in compression is compared graphically in Figures 42 & 43. In Figure 42 the mean value for the elastic modulus in compression is plotted against the mean porosity. In Figure 43 the Weibull modulus, or shape factor is plotted against mean apparent porosity.

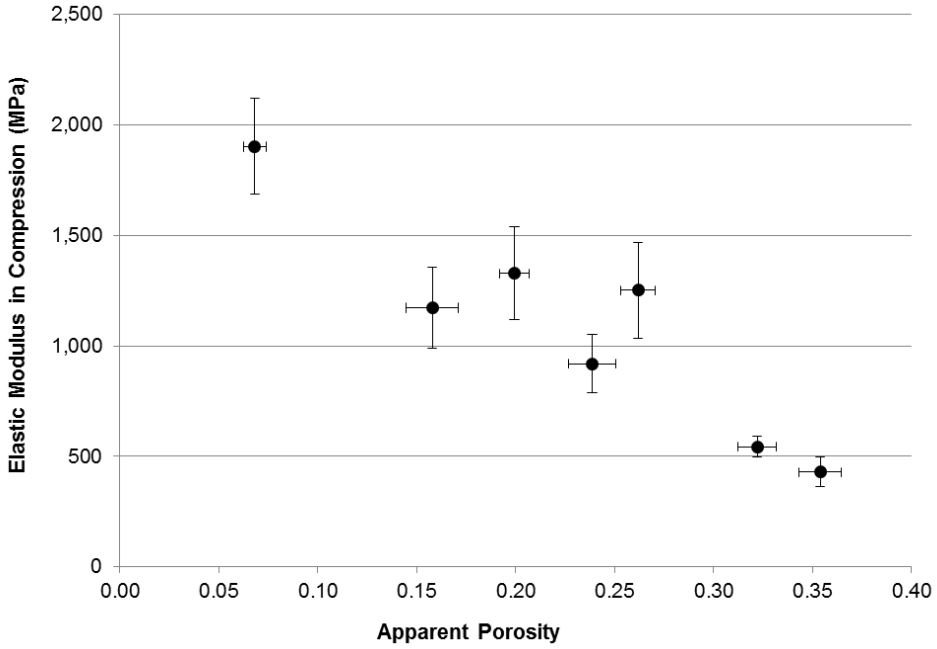

Figure 42. Mean value of the elastic modulus in compression as a function of porosity.

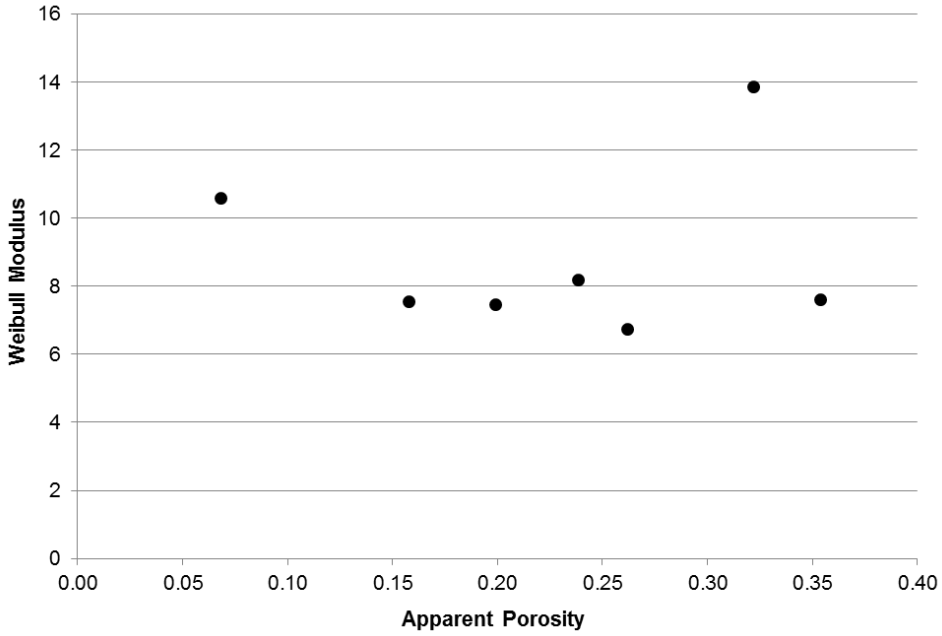

Figure 43. Graphical representation of the Weibull modulus for the elastic modulus in compression as a function of apparent porosity.

As expected, the mean value of the elastic modulus can be observed to increase as apparent porosity decreases. He vertical error bars in Figure 42 also indicate that the elastic

modulus data is more variable than the compressive strength data. In Figure 43 no trend in the data can be readily observed. In all cases the Weibull modulus is above six, but can be observed to be as high as ~14. Again the lowest value for the Weibull modulus occurs at 26.2% porosity.

4.2.4. COMPARISON TO MODELS

4.2.4.1. Compressive Strength: In comparing the experimental results to the published zero porosity compressive strength, an average value was used (Table 1). The data was then fit using four approaches. First an exponential relationship was used as was the case in Duckworth's[32] investigation of the relationship between porosity and strength (Equation 2.8). Then the data was fit using the three models for cellular materials proposed by Gibson and Ashby (Equations 2.9-2.11).

In fitting the data using Gibson and Ashby's models, the lower bounds on *a* and *b* were set at a value of zero, while φ was allowed to vary between zero and one, where a value of one correlates to open cells and a value of zero correlates to a fully dense material. Calculations were performed in MATLAB and the code is shown in Appendix A. The results are summarized in Table 5 below.

Table 5. Summary of curve fitting results for compressive strength, including regression analysis.

Fit Type	Value of Fitting Parameters			R^2	Adjusted R^2	RMSE
	a	b	ϕ			
Duckworth	40.48	--	--	0.9972	0.9972	4.60E+01
Gibson-Ashby: Open	0.2952	--	--	0.1903	0.1903	7.78E+02
Gibson-Ashby: Open	0.1625	--	--	0.2275	0.2275	7.60E+02
Gibson-Ashby: Closed	0.5636	8.20E-05	0.6497	0.1903	<0.0000	9.21E+02

The data in Table 5 shows that all three of Gibson and Ashby's correlations fit the data quite poorly. These models were developed for highly ordered materials with defined pore geometry and the material under investigation may be comprised of pores with varying pore

geometry and size. On the other hand, Duckworth's exponential correlation between strength and porosity appears to fit quite well. The exponential fit can be seen graphically in Figure 44, where the experimental data is represented by blue dots, the fitted model is represented by the solid red line and the upper and lower 95% confidence bounds are represented by the dashed red lines.

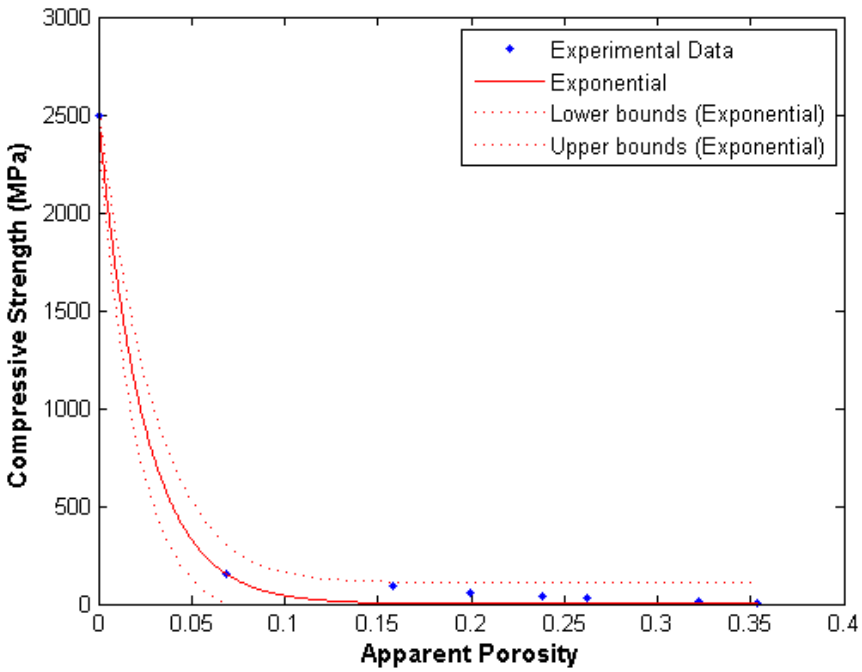

Figure 44. Experimental and published zero porosity data fit with an exponential function.

4.2.4.2. Elastic Modulus: As discussed in Chapter 2, many researchers have proposed empirical, semi-empirical or theoretical models to describe the behavior of the elastic modulus with respect to porosity. In this section ten relevant models will be compared to the experimental data obtained through this research. During the fitting of these models, the value of the zero porosity elastic modulus was taken as the average of published values and, when applicable, the value of Poisson's was limited by the minimum and maximum of published values (Table 1). In Nielsen's model, P_D and M have been set to unity, as suggested when modeling porous glasses. The fitting parameter describes the complexity of the pore structure and was allowed to vary between zero

and one. Fitting was performed in MATLAB (Appendix A) and the results are summarized in Table 6.

Table 6. Summary of fitting results for porosity vs. elastic modulus in compression, including regression analysis.

Fit Type	Value of Fitting Parameters				R^2	Adjusted R^2	RMSE
	a	b	n	v_o			
Hasselman	379.1	--	--	--	0.9997	0.9997	4.411E+02
Nielsen	.00287	--	--	--	0.9996	0.9996	5.157E+02
Wang	59.61	-131.7	--	--	0.9988	0.9987	8.992E+02
Spriggs	--	--	52.66	--	0.9986	0.9986	9.252E+02
Wagh - Poeppel-Singh	--	--	50.91	--	0.9986	0.9986	9.265E+02
Phani - Niyogi	0.03772	--	1394	--	0.9986	0.9983	9.994E+02
MacKenzie	9.143	18.89	--	--	0.7145	0.6669	1.415E+04
Brown - Biddulph - Wilcox	2.489	--	--	--	0.4225	0.4225	1.863E+04
Ramakrishnan	--	--	--	0.21	<0.0000	<0.0000	3.411E+04
Hashin	--	--	--	0.24	<0.0000	<0.0000	4.451E+04

Based on the adjusted R^2 values and the root mean square error, the Hasselman and Nielsen models appear to fit the data most accurately. The models proposed by Wang, Spriggs, Wagh et al. and Phani-Niyogi also fit quite well, while the models proposed by MacKenzie and Brown et al. are less accurate. Both of these models use a polynomial approach and data are fit through manipulation of the coefficients. Ramakrishnan and Hashin's models, which utilize the zero porosity Poisson's ratio, fit very poorly. The models are plotted with the experimental data in Figures 45-54 on the following pages; they are presented according to the adjusted R^2 values, in descending order.

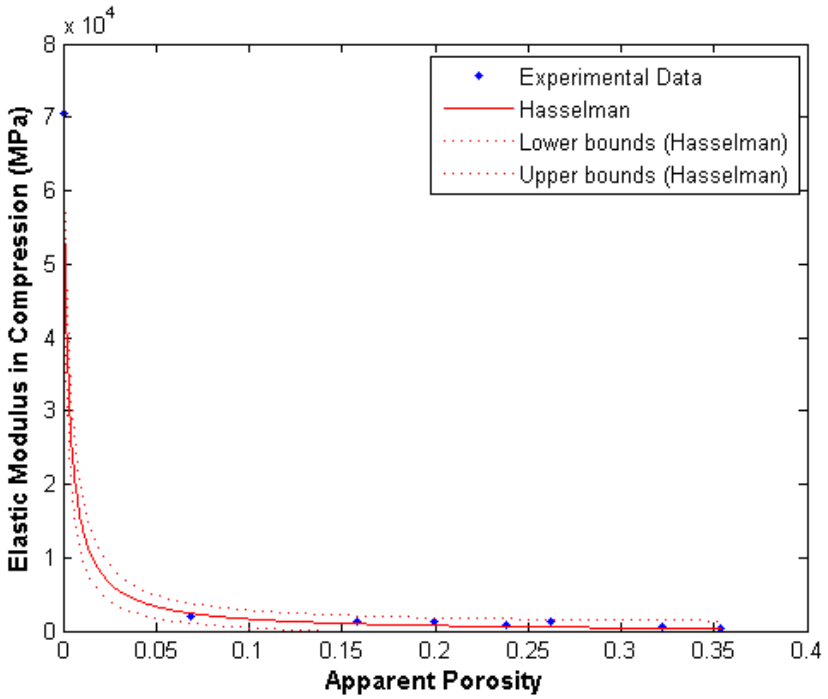

Figure 45. Porosity vs. mean elastic modulus in compression data fitted with the Hasselman correlation.

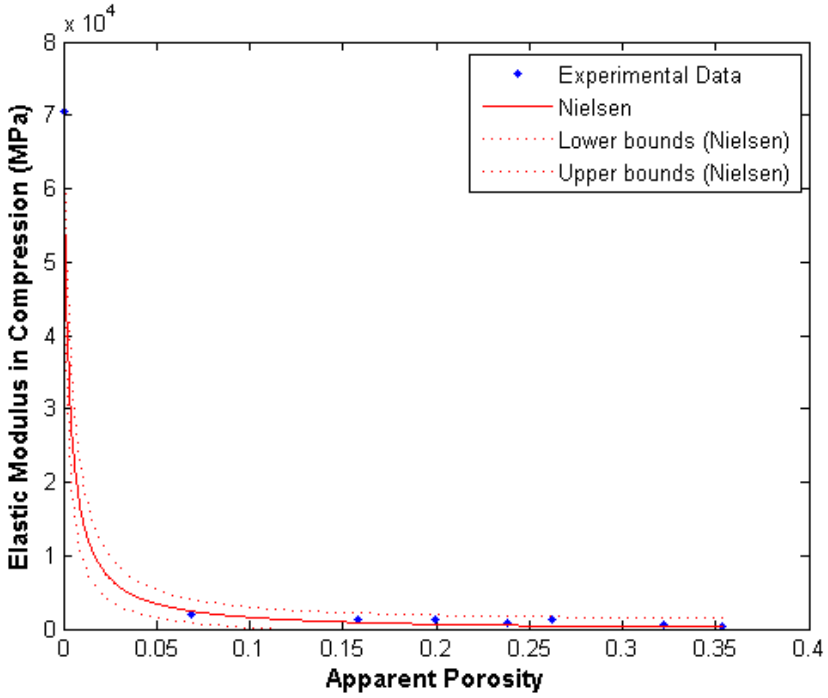

Figure 46. Porosity vs. mean elastic modulus in compression data fitted with the Nielsen correlation.

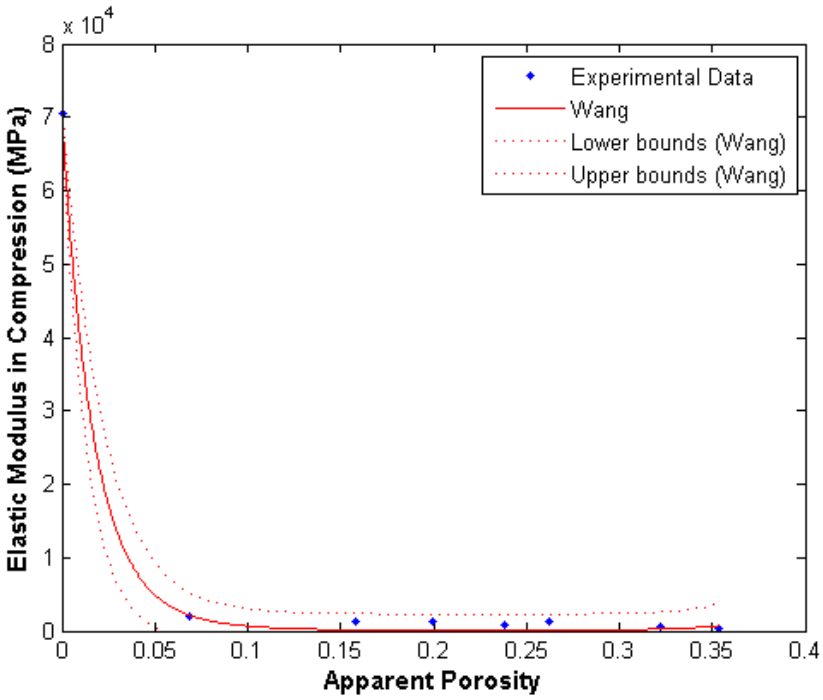

Figure 47. Porosity vs. mean elastic modulus in compression data fitted with the Wang correlation.

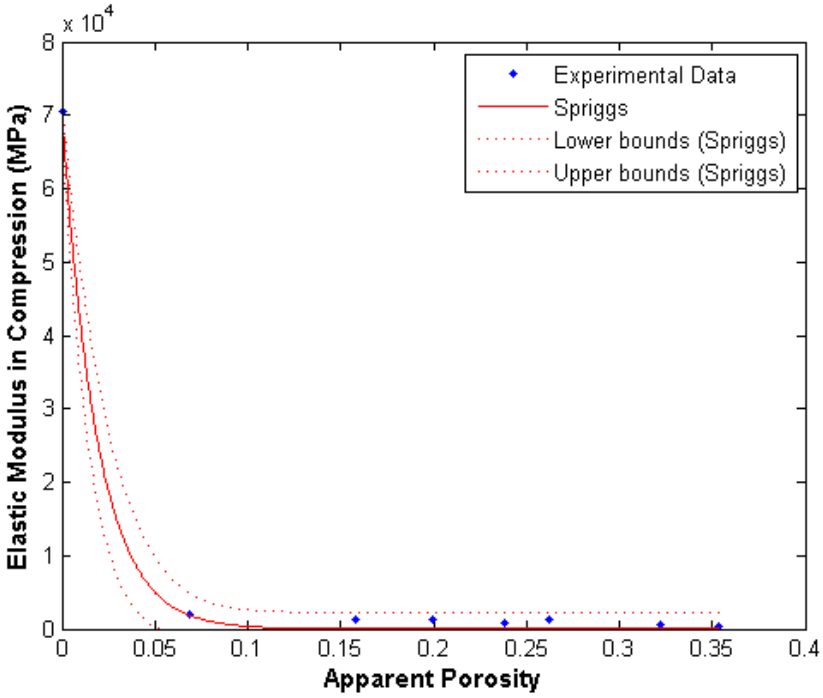

Figure 48. Porosity vs. mean elastic modulus in compression data fitted with the Spriggs correlation.

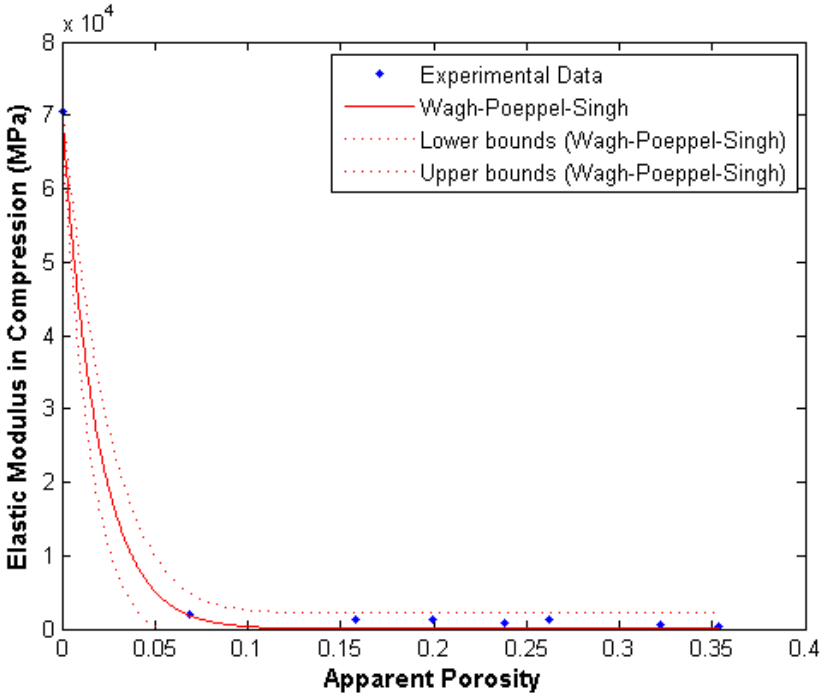

Figure 49. Porosity vs. mean elastic modulus in compression data fitted with the Wagh-Singh-Poeppel correlation.

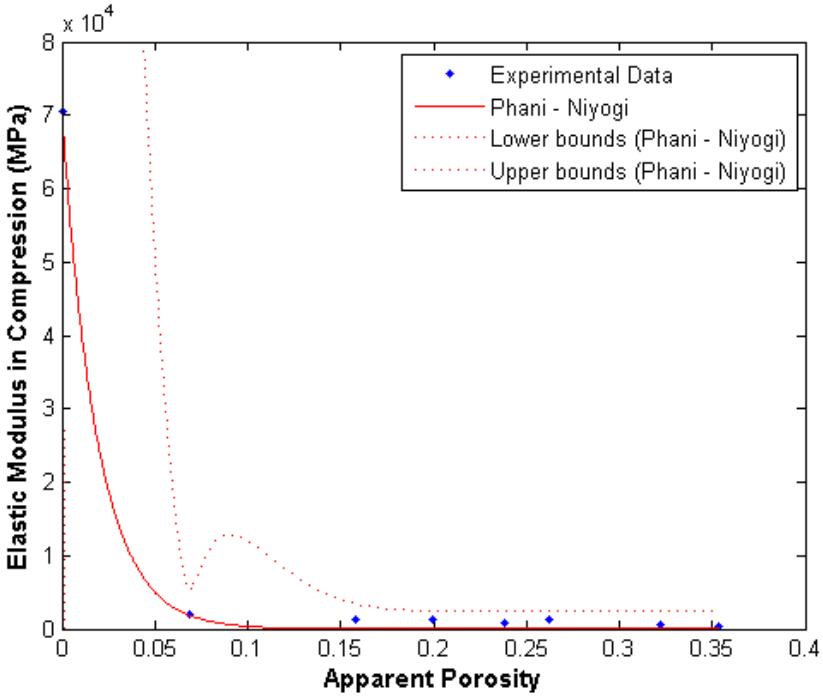

Figure 50. Porosity vs. mean elastic modulus in compression data fitted with the Phani-Niyogi correlation.

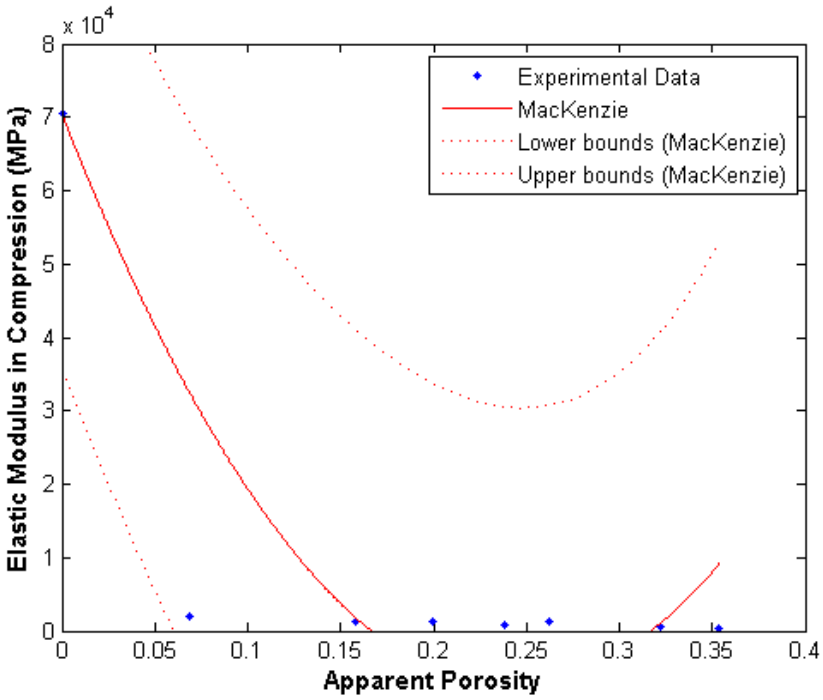

Figure 51. Porosity vs. mean elastic modulus in compression data fitted with the MacKenzie correlation.

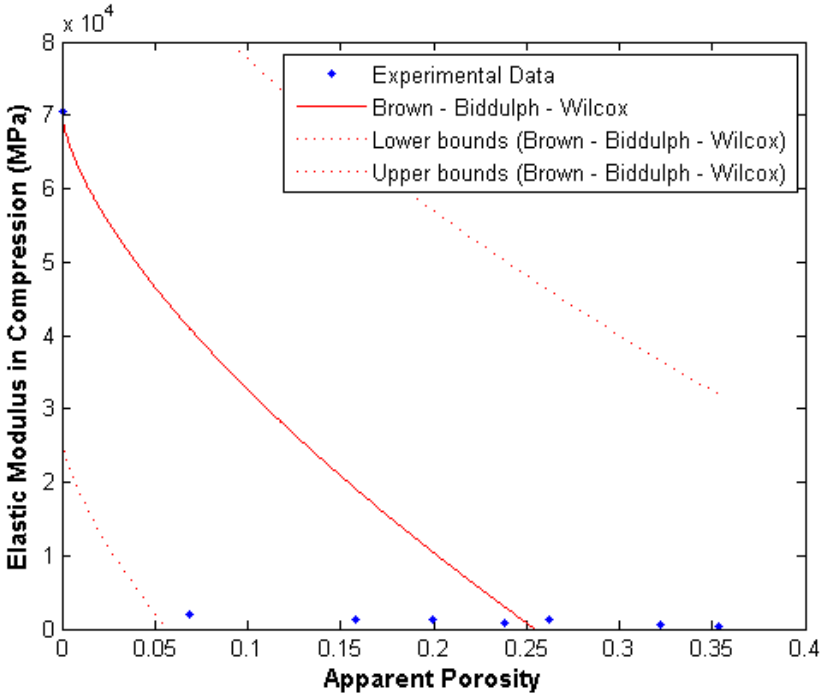

Figure 52. Porosity vs. mean elastic modulus in compression data fitted with the Brown-Biddulph-Wilcox correlation.

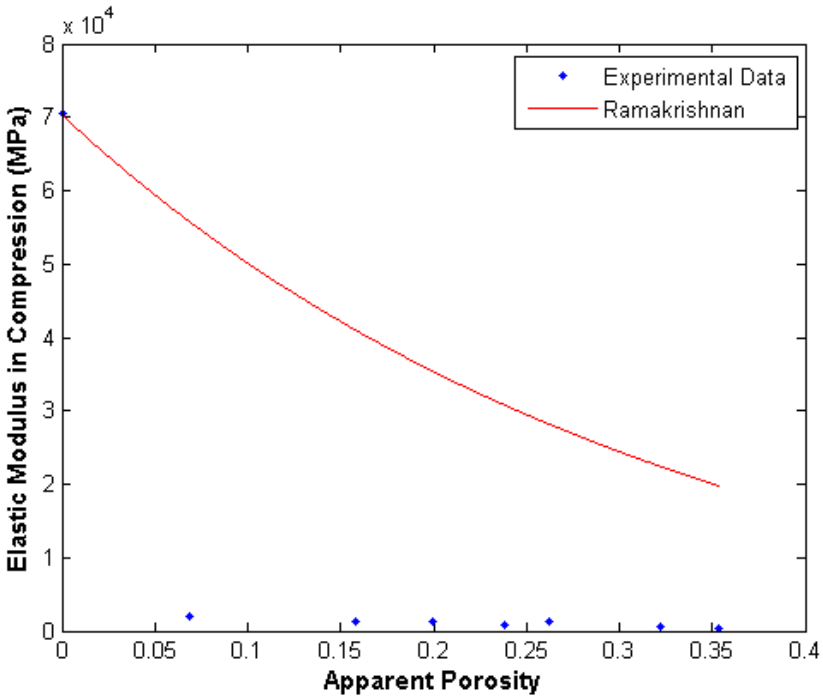

Figure 53. Porosity vs. mean elastic modulus in compression data fitted with the Ramakrishnan correlation. The 95% confidence bounds are too large to be shown.

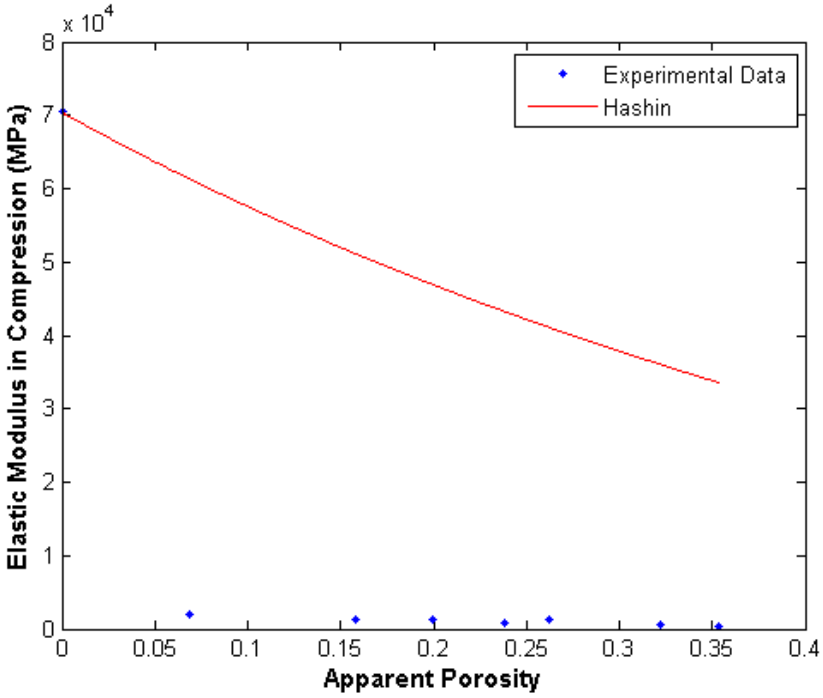

Figure 54. Porosity vs. mean elastic modulus in compression data fitted with the Hashin correlation. The 95% confidence bounds are too large to be shown.

Through inspection of the preceding figures it can be seen that Hasselman and Nielsen's models fits the data most accurately based on the narrow 95% confidence interval as well as the high adjusted R^2 value. The correlation proposed by Wang fits quite well below 32% apparent porosity, while the Spriggs and Wagh-Singh-Poeppel correlations fit the data throughout the range of experimental values. In general the confidence intervals can be observed to become slightly larger as the adjusted R^2 value increases, as would be expected. However, in Figure 68, the 95% confidence bounds on the Phani-Niyogi model are larger and more irregular than anticipated. Although the confidence bounds are quite narrow in the areas in the immediate vicinity of data points, they become more unpredictable where data is not present. The models proposed by MacKenzie, Brown et al., Ramakrishnan and Hashin fit the data quite poorly. The 95% confidence bounds on both the Ramakrishnan and Hashin models are so large that they do not appear on the plots.

The Hasselman, Nielsen, Wang, Spriggs, Wagh-Singh-Poeppel and Phani-Niyogi models all fit the data reasonably well in the higher porosity ranges; however the shape of the curves differ in the lower porosity ranges. These models are compared in Figure 55, where only the 0-20% apparent porosity range is shown.

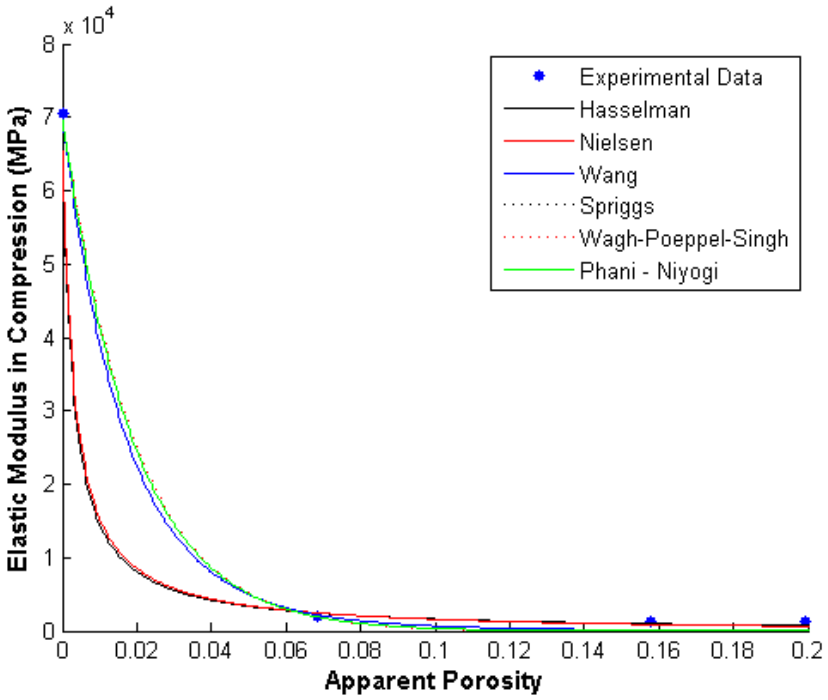

Figure 55. Comparison of the 6 most accurate models for the elastic modulus in compression.

When the models are compared it appears that the Hasselman and Nielsen models fit the experimental data most accurately. The Wang, Spriggs, Wagh-Singh-Poeppel and Phani-Niyogi models all perform very similarly and differ significantly from both the Hasselman and Nielsen models when the apparent porosity is below 6%.

4.3. Flexural Behavior

4.3.1. Stress-Strain Behavior Under Flexural Loading

The stress-strain behavior of all transverse specimens can be seen on the next few pages in Figures 56-62. Stress-strain data is grouped in batches and is shown in order of descending apparent porosity, which was between 7.7 and 34.2%.

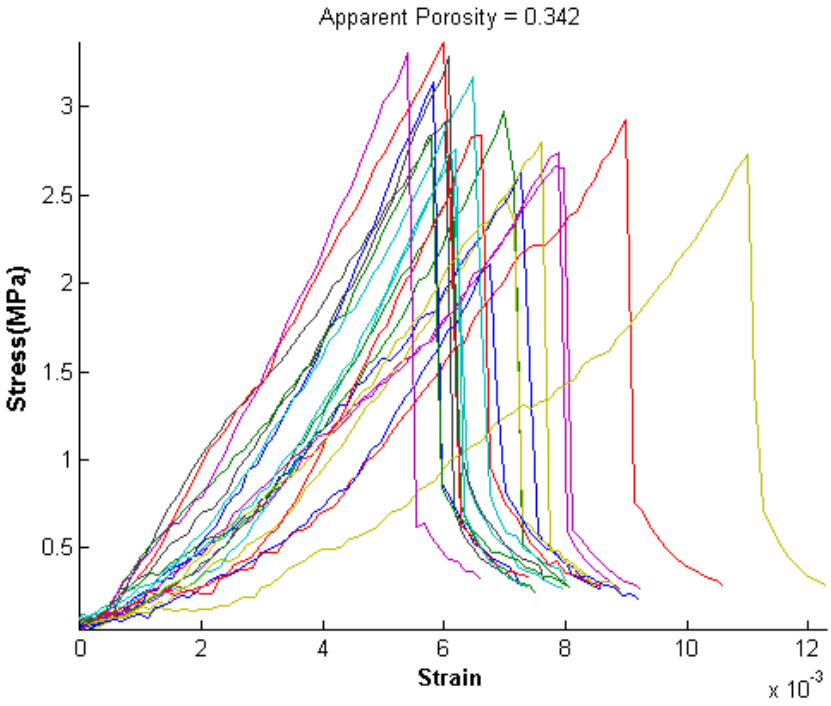

Figure 56. Transverse stress vs. transverse strain: 34.2% apparent porosity.

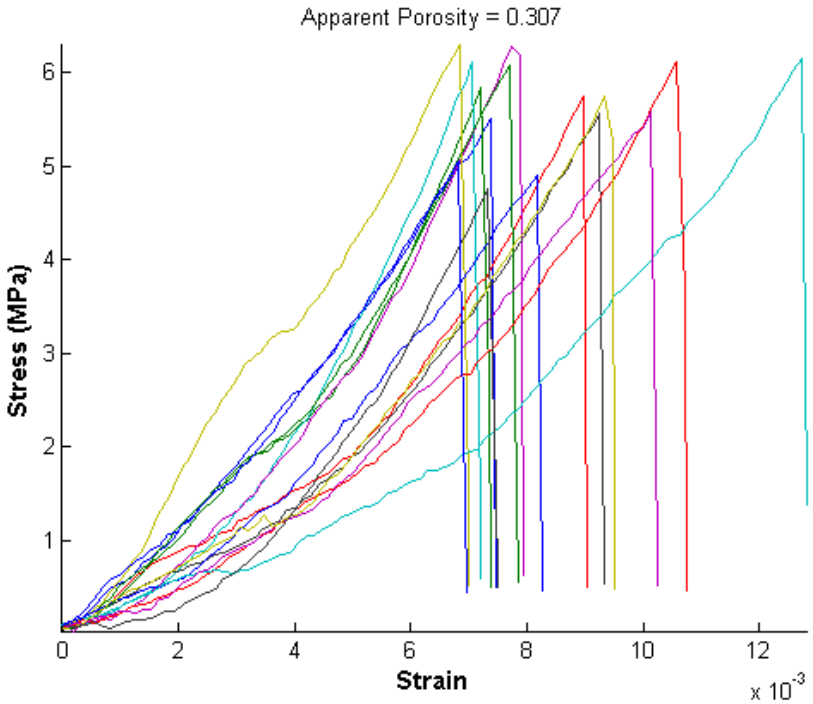

Figure 57. Transverse stress vs. transverse strain: 30.7% apparent porosity.

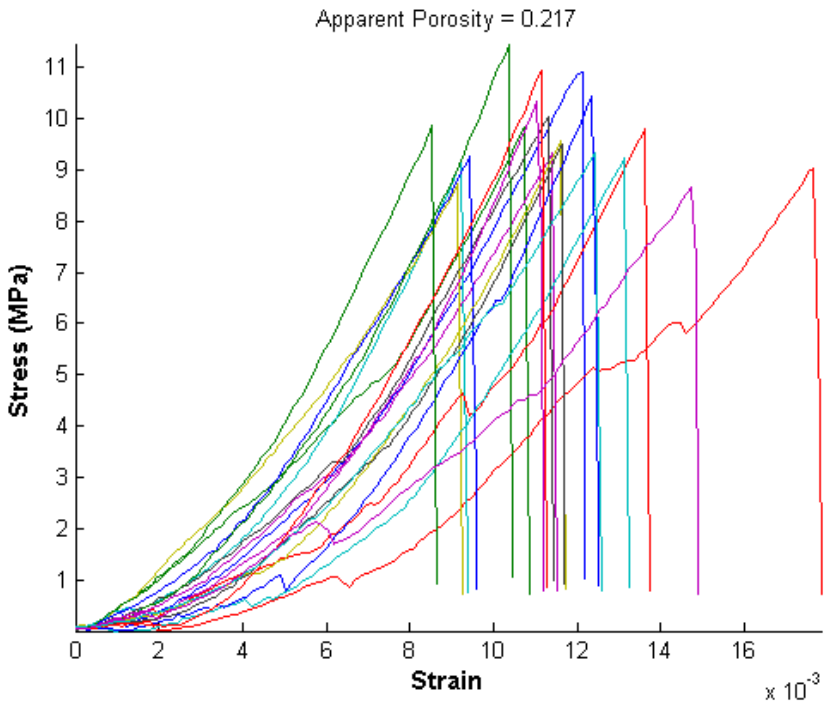

Figure 58. Transverse stress vs. transverse strain: 21.7% apparent porosity.

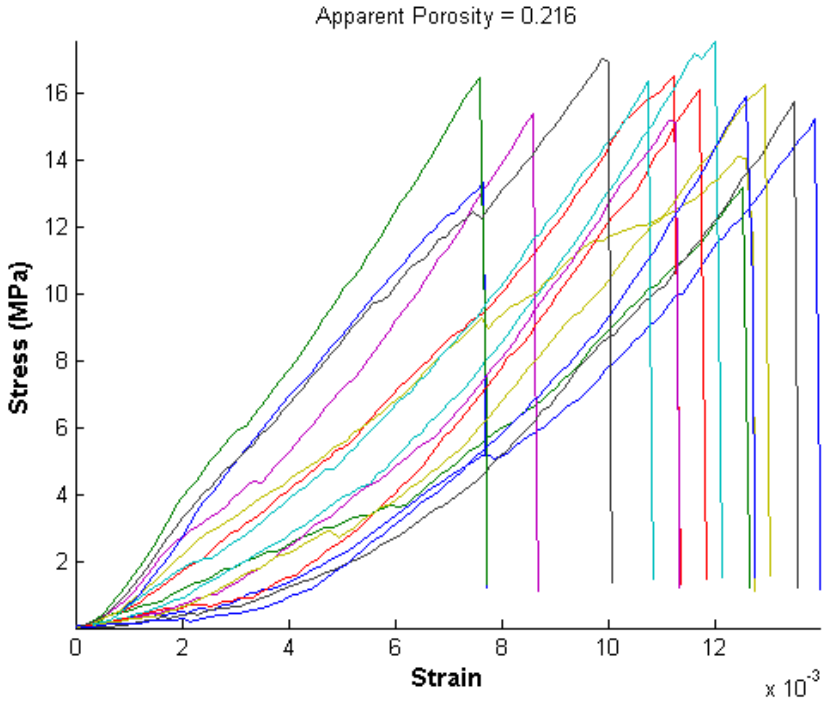

Figure 59. Transverse stress vs. transverse strain: 21.6% apparent porosity.

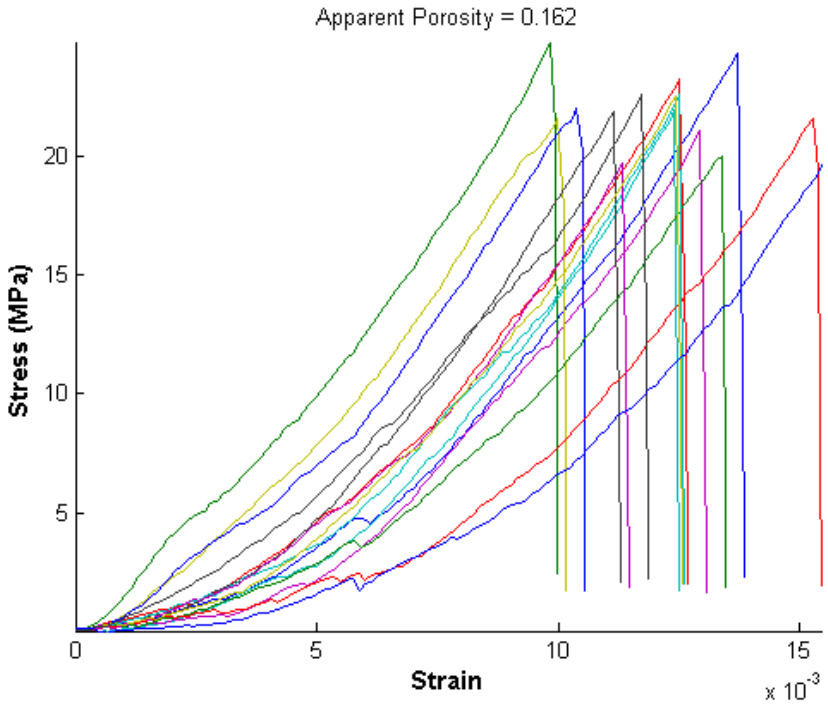

Figure 60. Transverse stress vs. transverse strain: 16.2% apparent porosity.

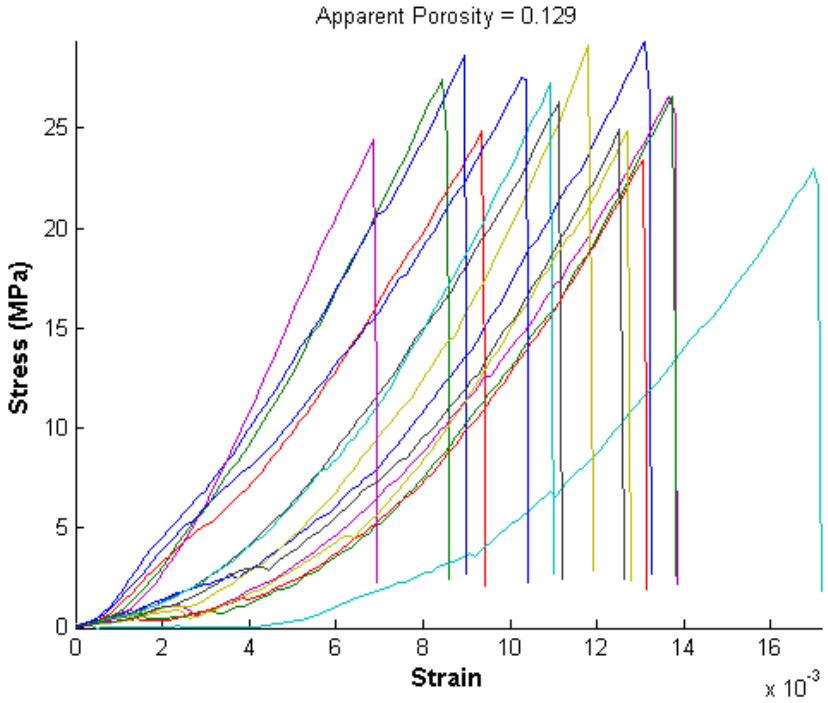

Figure 61. Transverse stress vs. transverse strain: 12.9% apparent porosity.

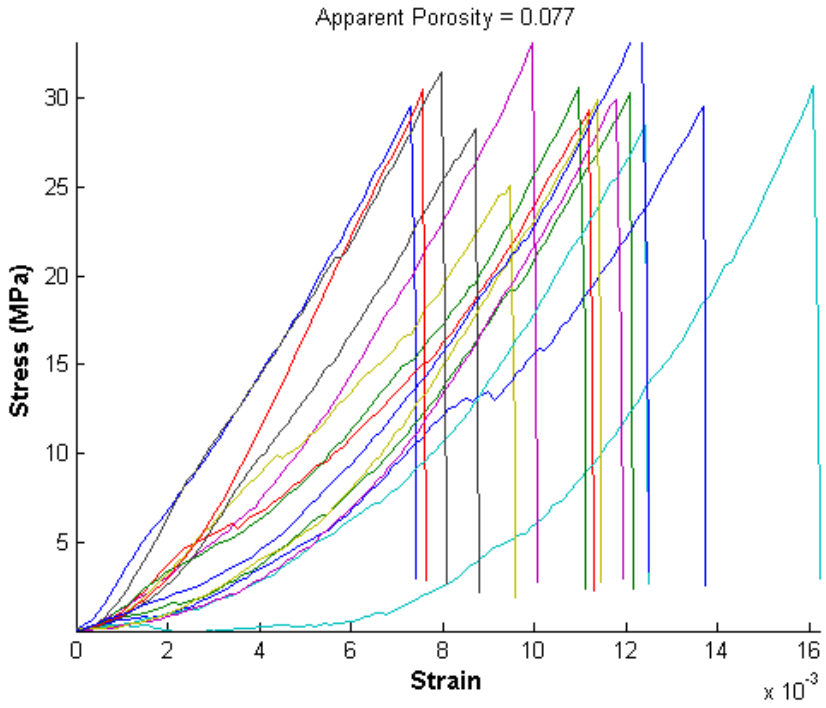

Figure 62. Transverse stress vs. transverse strain: 7.7% apparent porosity.

As expected, the flexural specimens exhibited behavior consistent with porous, brittle materials and did not undergo plastic deformation. Catastrophic failure occurred at the point when maximum stress was achieved. As was the case with the compressive data, the stress-strain curves appear to exhibit non-linear behavior during initial loading. In general, the behavior exhibited by the specimens was somewhat erratic and non-linear until approximately 25-35% of the maximum stress was reached. At that point the stress-strain behavior tended towards linear. Unlike the compressive testing, stress-strain behavior, with the exception of maximum stress, was relatively consistent across the entire range of apparent porosity present.

4.3.2. Elastic Modulus Under Flexural Load

A similar approach was used in determining the elastic modulus in flexure. In this case the most linear portion of the stress-strain curves was observed to begin after 40% of the maximum stress was achieved and data after rupture was removed. These calculations were

performed in MATLAB (Appendix A). The linear portion of the stress-strain curves can be seen in Figures 63-69.

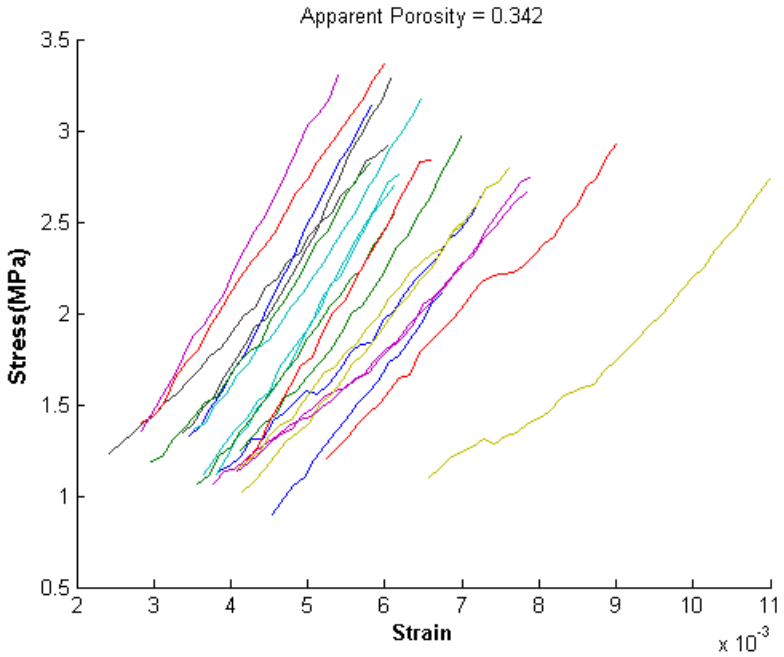

Figure 63. Portion of the stress-strain curve used in calculating the elastic modulus in flexure: 34.2% apparent porosity.

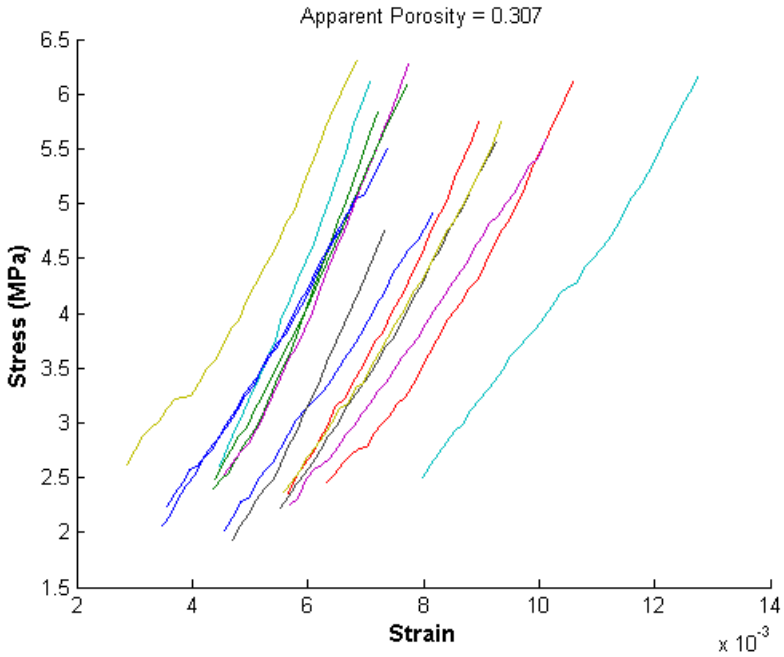

Figure 64. Portion of the stress-strain curve used in calculating the elastic modulus in flexure: 30.7% apparent porosity.

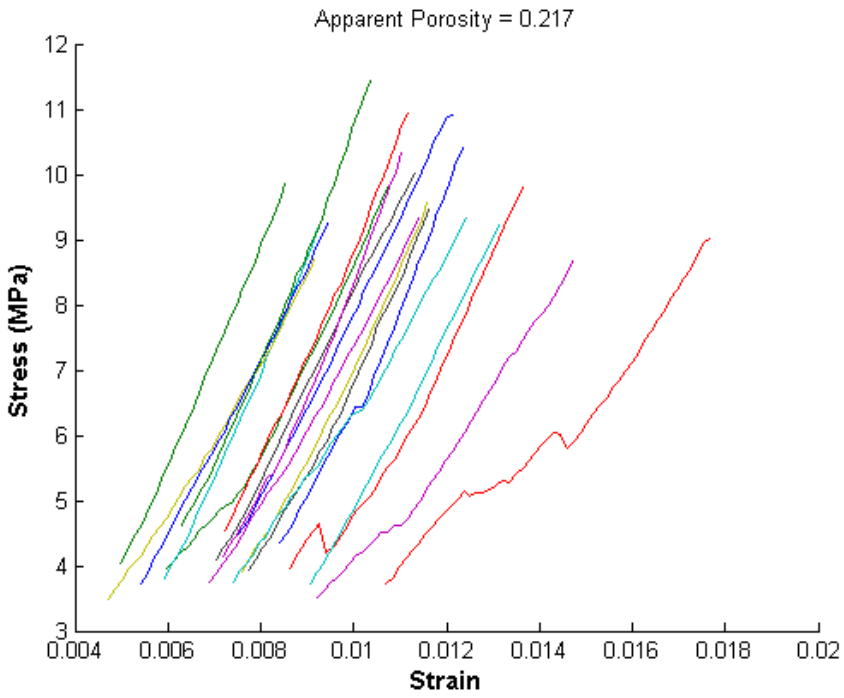

Figure 65. Portion of the stress-strain curve used in calculating the elastic modulus in flexure: 21.7% apparent porosity.

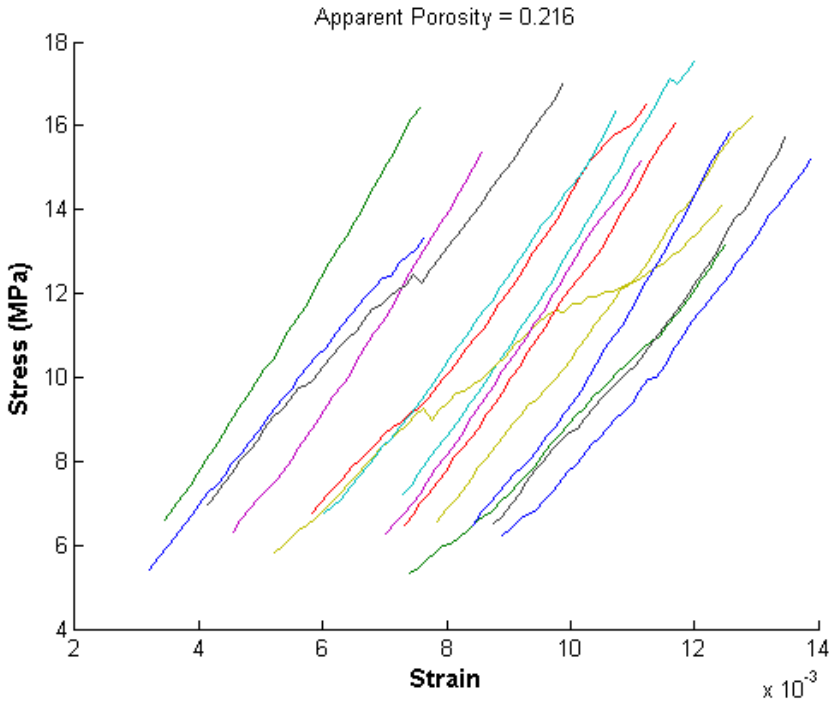

Figure 66. Portion of the stress-strain curve used in calculating the elastic modulus in flexure: 21.6% apparent porosity.

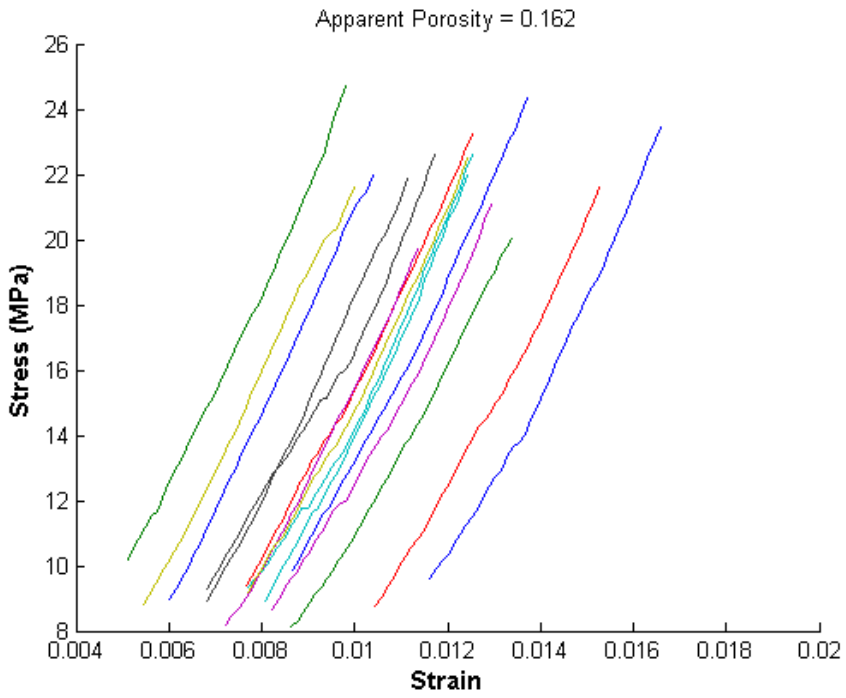

Figure 67. Portion of the stress-strain curve used in calculating the elastic modulus in flexure: 16.2% apparent porosity.

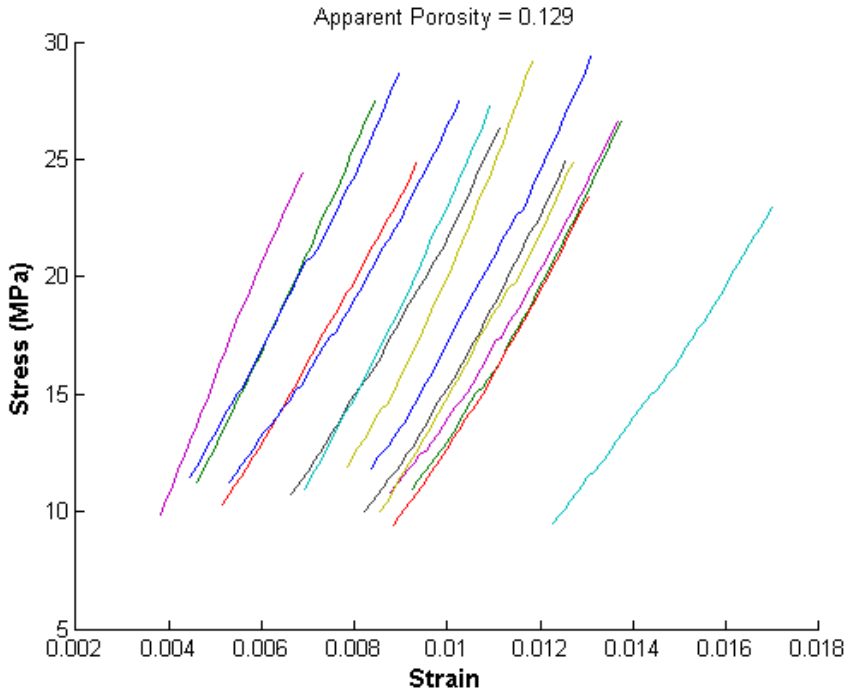

Figure 68. Portion of the stress-strain curve used in calculating the elastic modulus in flexure: 12.9% apparent porosity.

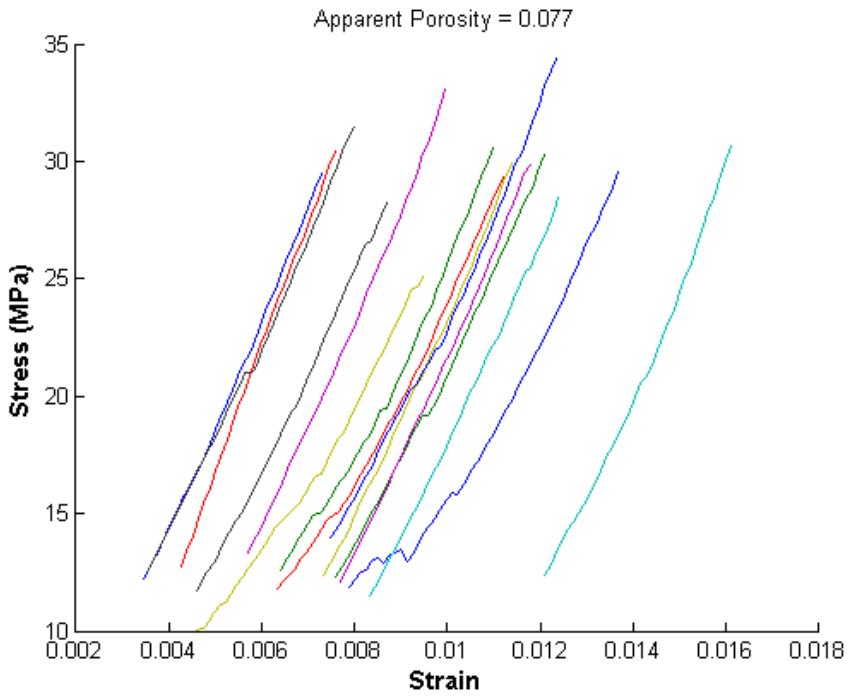

Figure 69. Portion of the stress-strain curve used in calculating the elastic modulus in flexure: 7.7% apparent porosity.

The elastic portion of flexural stress-strain curves can be characterized by being generally linear, particularly as apparent porosity decreases. However, in almost all cases, the curves can also be characterized by discontinuities and load drops, as was the case with the data obtained through compressive testing.

4.3.3. WEIBULL ANALYSIS

4.3.3.1. Transverse Strength: After flexural testing, the data was analyzed using the Weibull method. The results of the this analysis for transverse rupture strength are summarized in Table 7, where the mean transverse strength ranges from 2.84 to 29.95 MPa and the Weibull modulus varies from 10.62 to 17.71. The Weibull CDFs are shown in Figures 70-76.

Table 7. Summary of results for Weibull analysis of transverse strength data.

Apparent Porosity	Mean (MPa)	Std. Dev. (MPa)	Scale Factor (MPa)	Modulus
0.0775	29.9494	2.4091	30.9975	15.2610
0.1286	26.2658	2.1169	27.1867	15.2304
0.1621	22.1827	1.5467	22.8593	17.7050
0.2158	15.6090	1.2002	16.1322	15.9939
0.2170	9.7089	0.9277	10.1091	12.7486
0.3070	5.7278	0.4503	5.9239	15.6303
0.3423	2.8414	0.3228	2.9792	10.6247

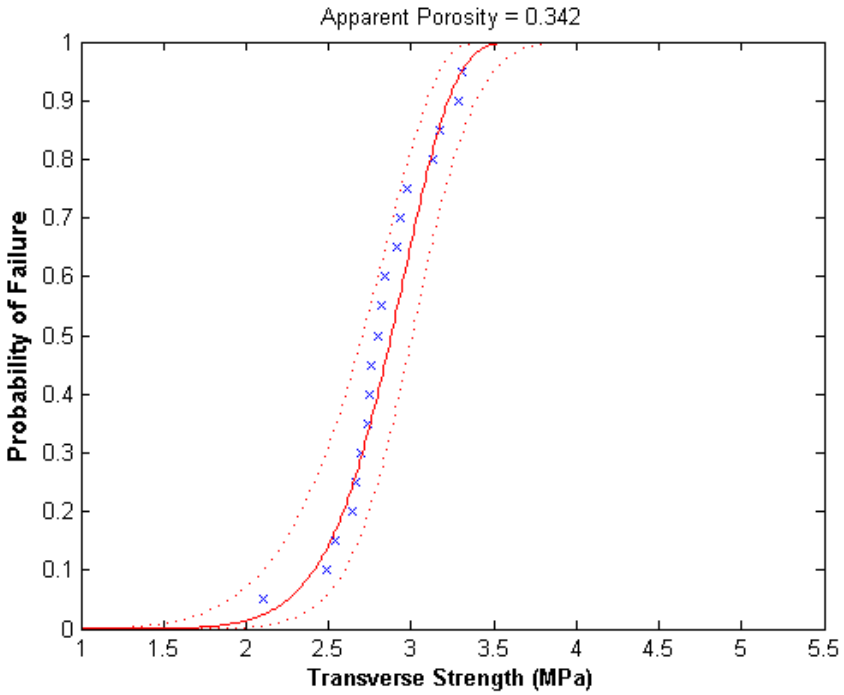

Figure 70. Weibull CDF for transverse strength at 34.2% apparent porosity.

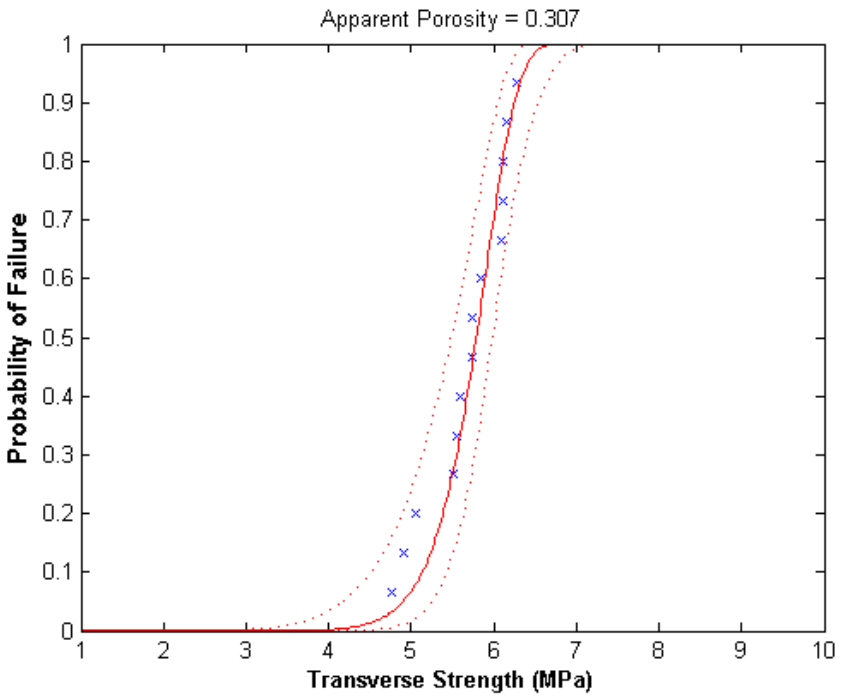

Figure 71. Weibull CDF for transverse strength at 30.7% apparent porosity.

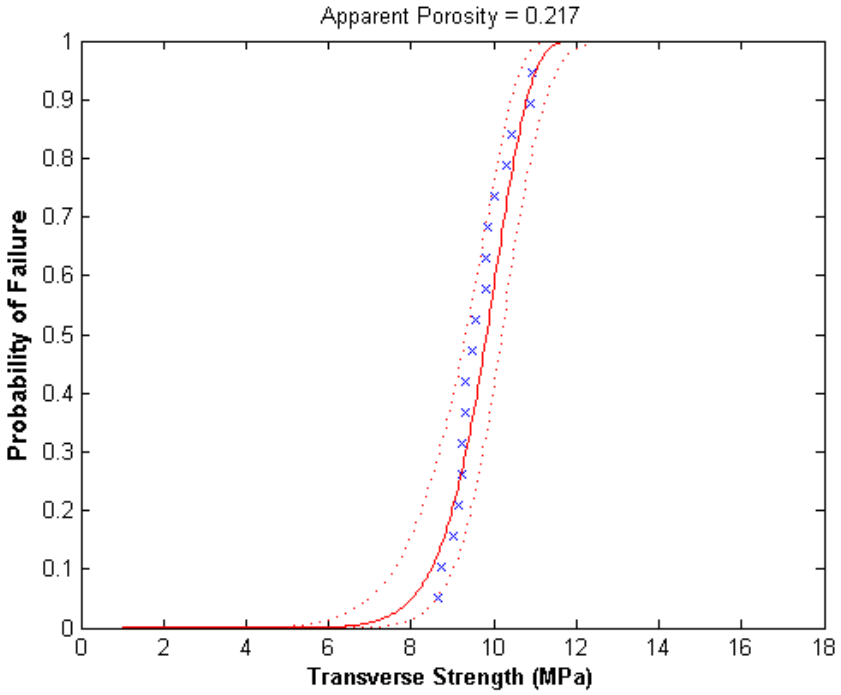

Figure 72. Weibull CDF for transverse strength at 21.7% apparent porosity.

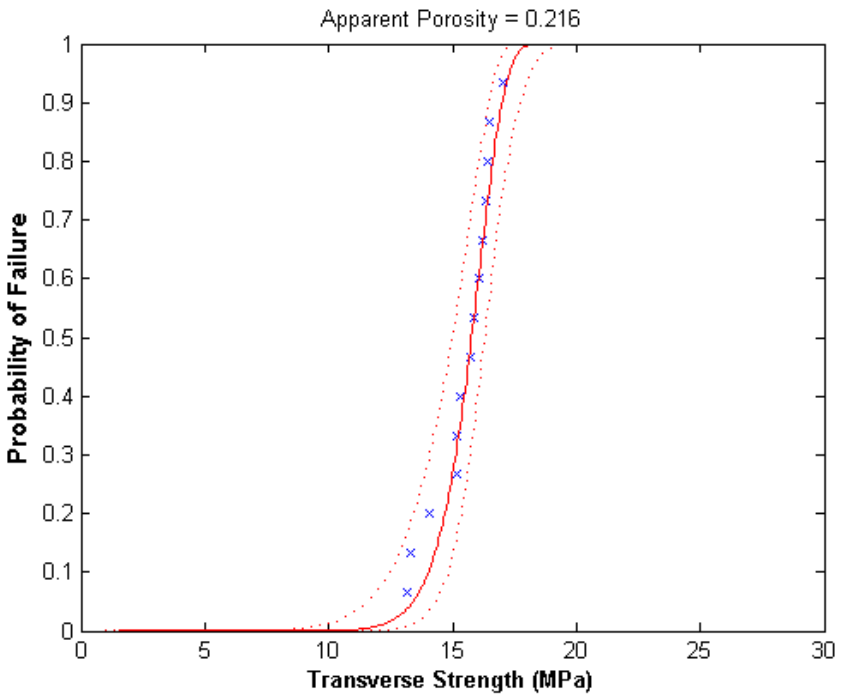

Figure 73. Weibull CDF for transverse strength at 21.6% apparent porosity.

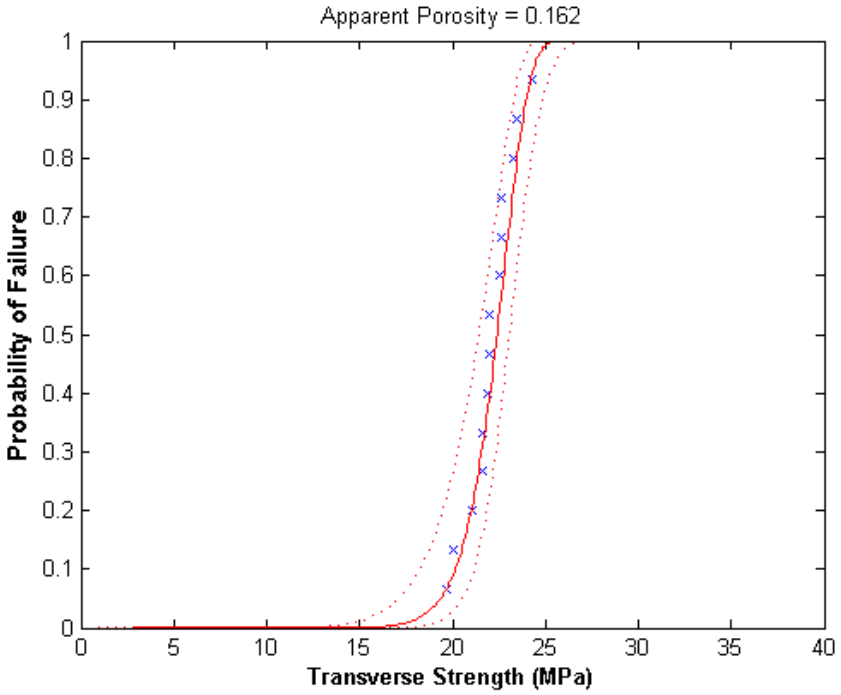

Figure 74. Weibull CDF for transverse strength at 16.2% apparent porosity.

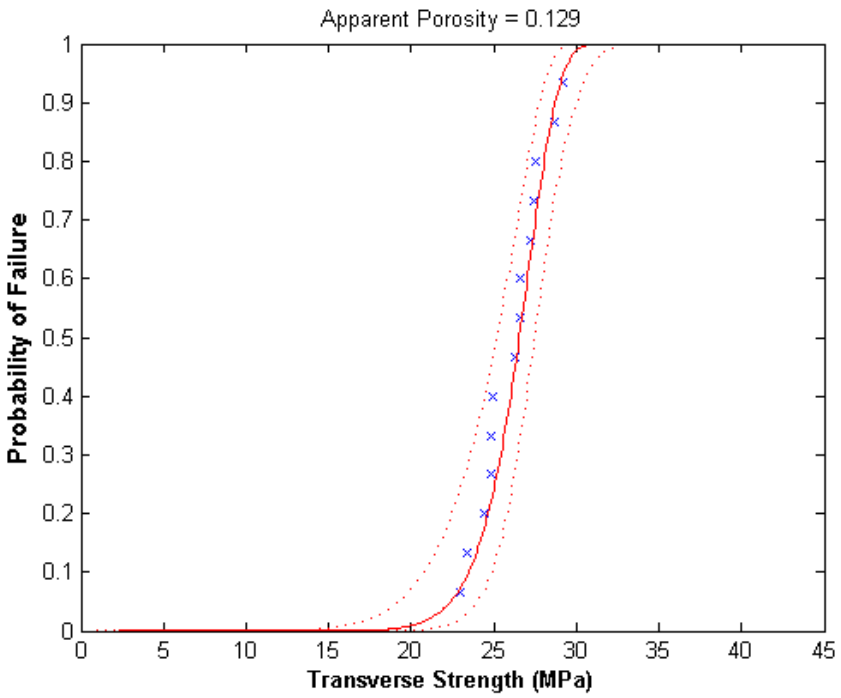

Figure 75. Weibull CDF for transverse strength at 12.9% apparent porosity.

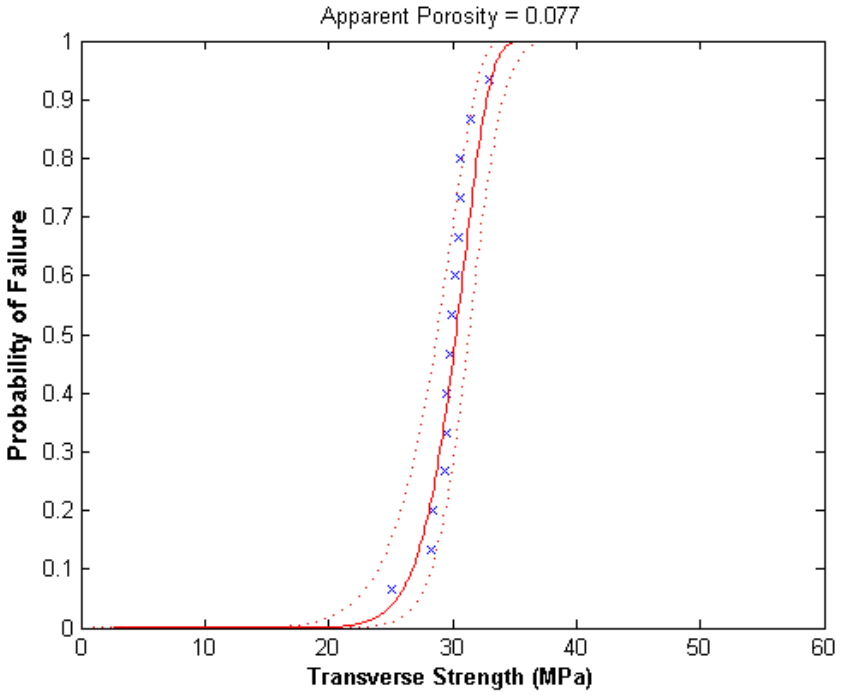

Figure 76. Weibull CDF for transverse strength at 7.7% apparent porosity.

The Weibull data tabulated above is shown graphically in Figures 77 & 78. In Figure 77 the mean transverse strength is plotted against the mean porosity. In Figure 78 the Weibull modulus, or shape factor is plotted against mean apparent porosity.

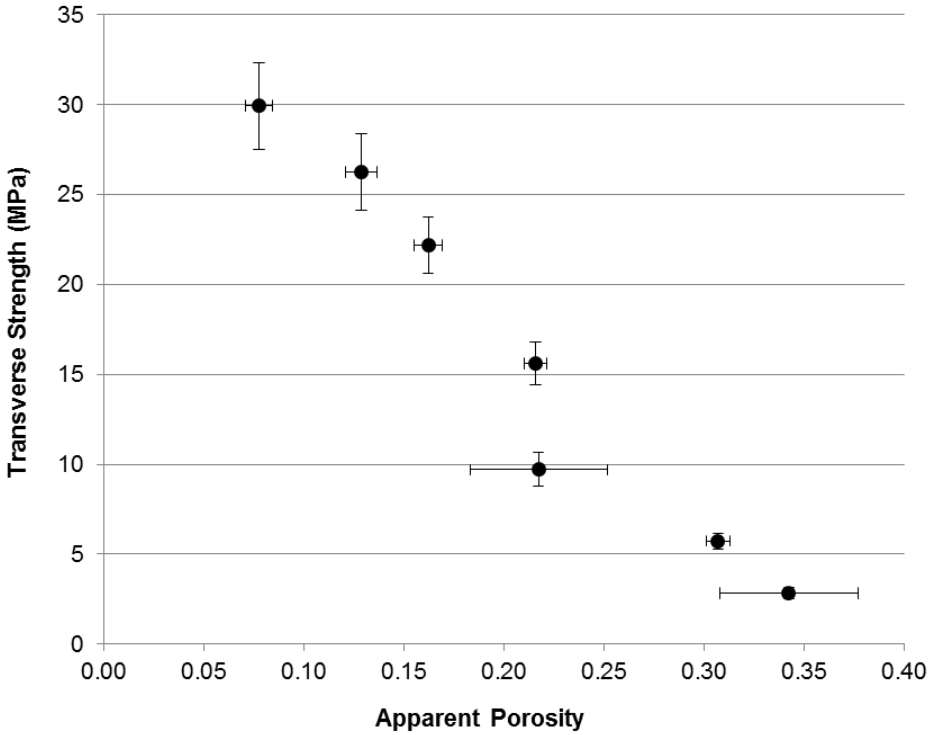

Figure 77. Mean flexure strength as a function of porosity.

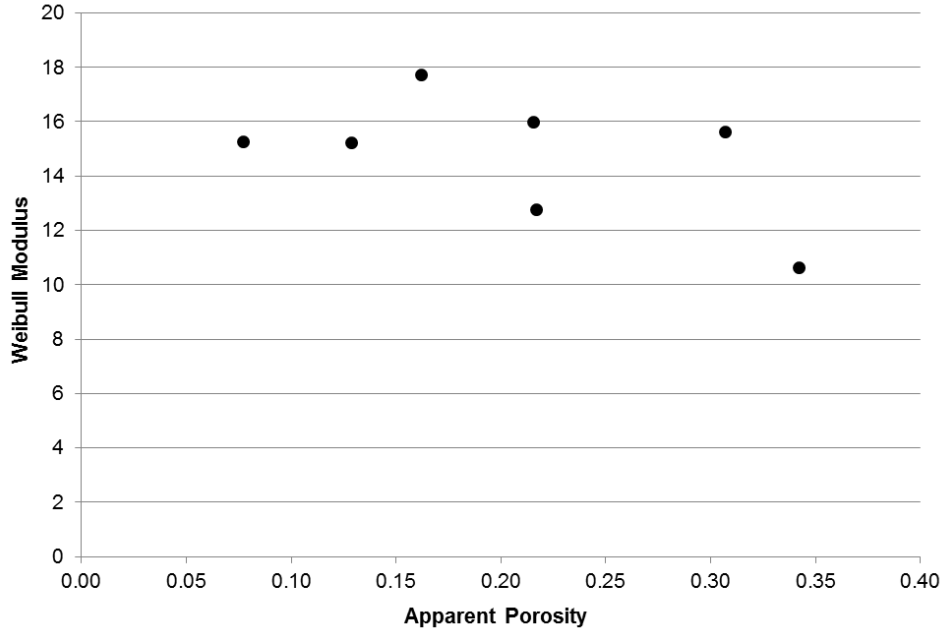

Figure 78. Graphical representation of the Weibull Modulus for transverse strength as a function of apparent porosity.

As expected, the mean transverse strength can be observed to increase as apparent porosity decreases. As with the compressive data, the standard deviation in compressive strength is larger at lower porosity; however, this behavior is not as pronounced. In Figure 78 no trend in the data can be readily observed. In all cases the Weibull modulus for the transverse strength data is above ten.

4.3.3.2. Elastic Modulus Under Flexural Loading: A summary of the Weibull analysis for the elastic modulus in flexure is shown in Table 8. The mean values for the elastic modulus in flexure range between 573.58 and 4112.36 MPa and values for the Weibull modulus vary from 5.09 to 19.64. The Weibull cumulative distribution functions for each batch are shown in Figures 79-85.

Table 8. Summary of Weibull data for elastic modulus in flexure.

Apparent Porosity	Mean (MPa)	Std. Dev. (MPa)	Scale Factor (MPa)	Modulus
0.0775	4112.3621	598.6737	4362.4788	8.1641
0.1286	3664.2996	644.5203	3556.1209	5.9436
0.1621	2805.3861	176.9182	2883.0391	19.6438
0.2158	1954.9952	312.5045	2084.1800	7.3857
0.2170	1356.0461	233.9742	1451.8103	6.8026
0.3070	970.8590	199.1849	1050.1388	5.6389
0.3423	573.5839	129.1935	624.0418	5.0927

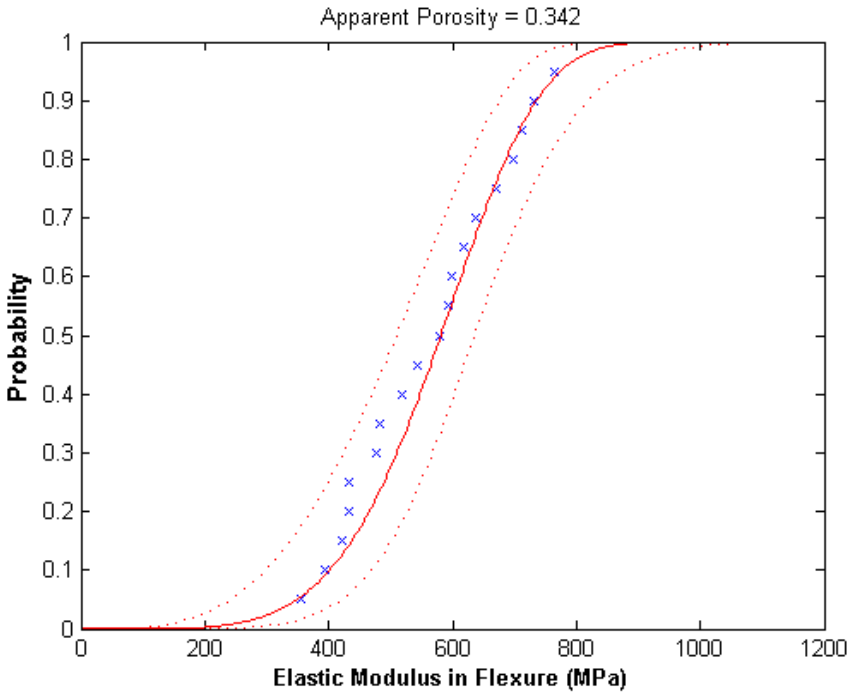

Figure 79. Weibull CDF for the elastic modulus in flexure at 34.2% apparent porosity.

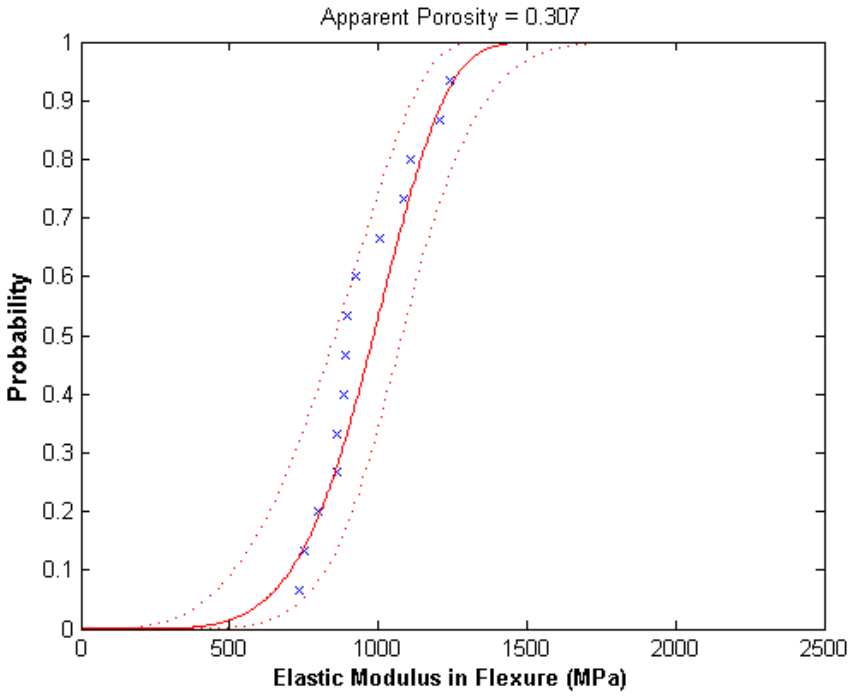

Figure 80. Weibull CDF for the elastic modulus in flexure at 30.7% apparent porosity.

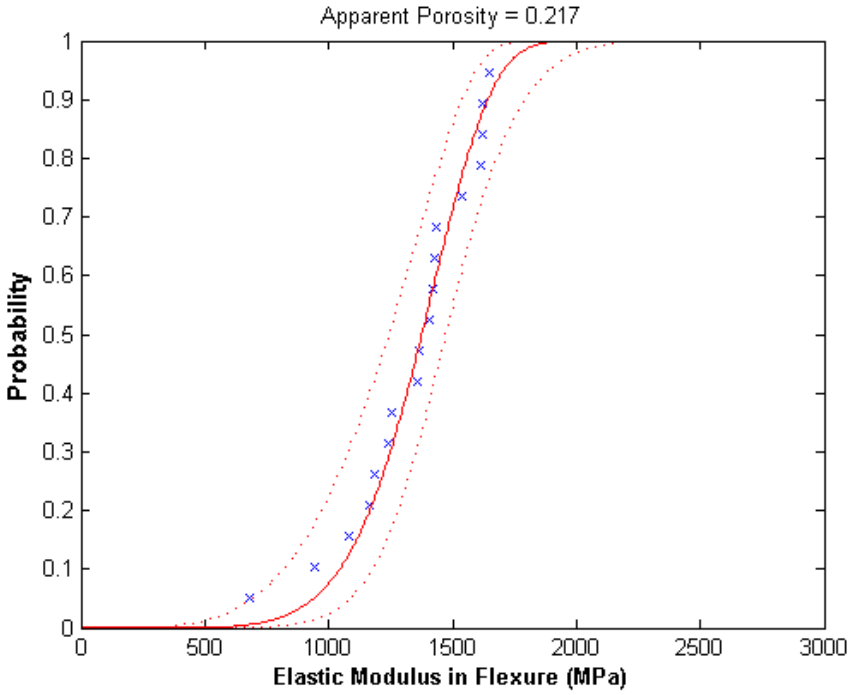

Figure 81. Weibull CDF for the elastic modulus in flexure at 21.7% apparent porosity.

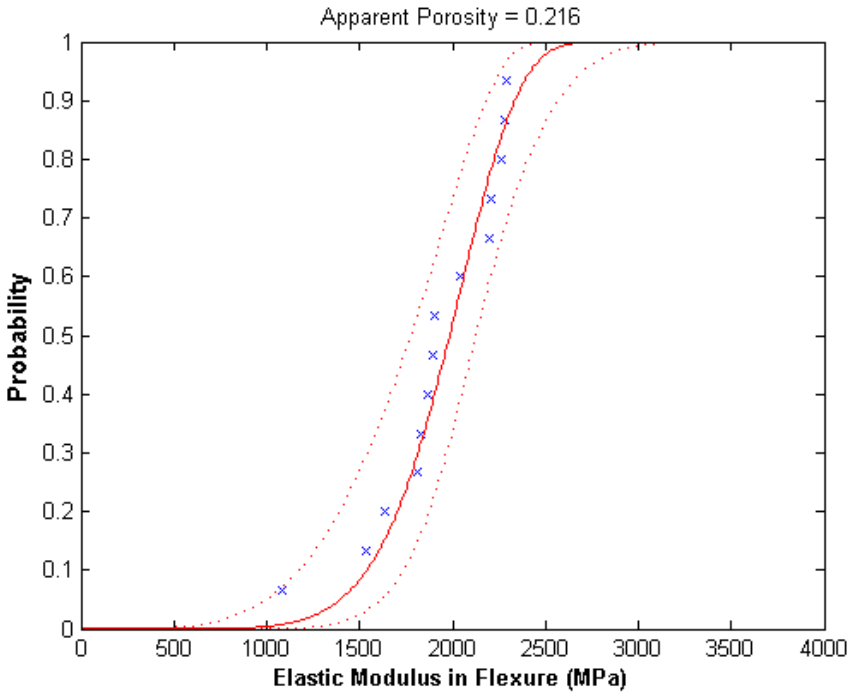

Figure 82. Weibull CDF for the elastic modulus in flexure at 21.6% apparent porosity.

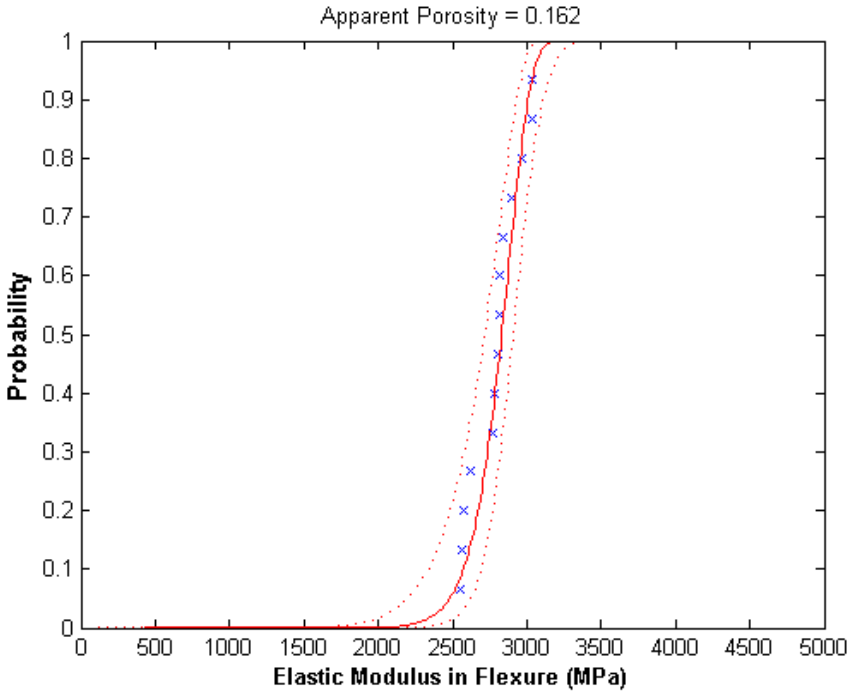

Figure 83. Weibull CDF for the elastic modulus in flexure at 16.2% apparent porosity.

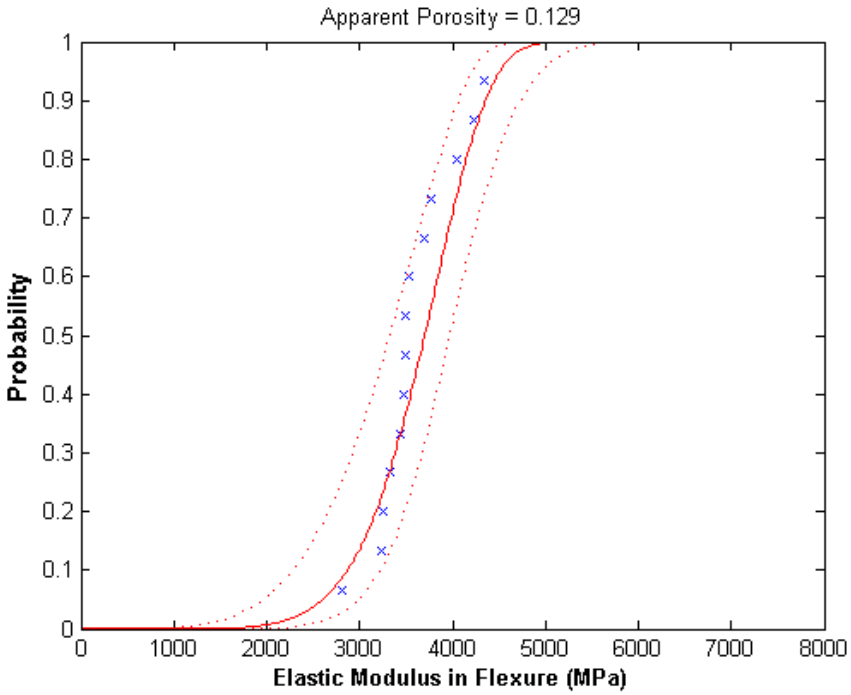

Figure 84. Weibull CDF for the elastic modulus in flexure at 12.9% apparent porosity.

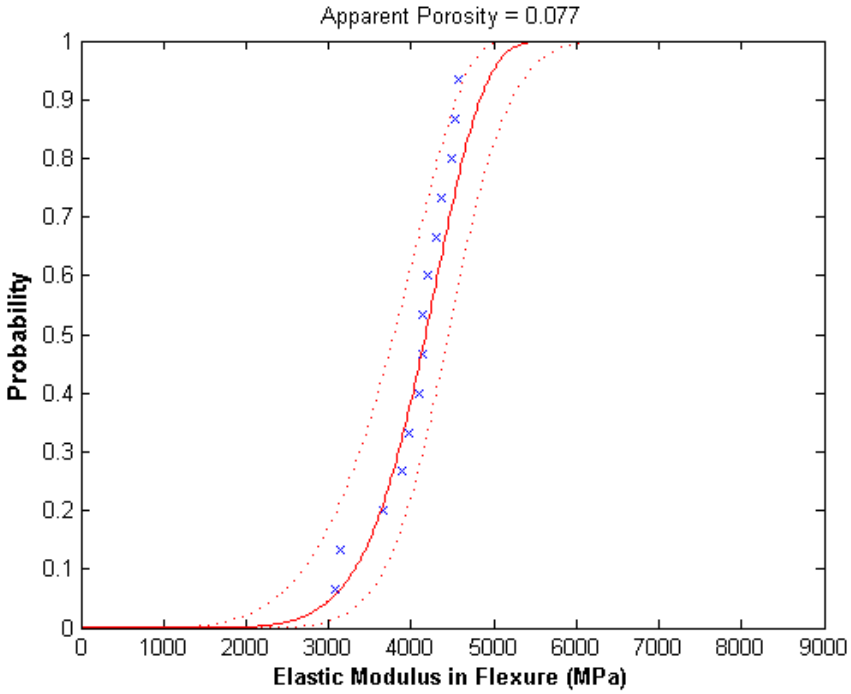

Figure 85. Weibull CDF for the elastic modulus in flexure at 7.7% apparent porosity.

A comparison of the results of the Weibull analysis for the elastic modulus in flexure is shown graphically in Figures 86 & 87. In Figure 86 the mean value for the elastic modulus in

flexure is plotted against the porosity. In Figure 86 the Weibull modulus, or shape factor is plotted against mean apparent porosity.

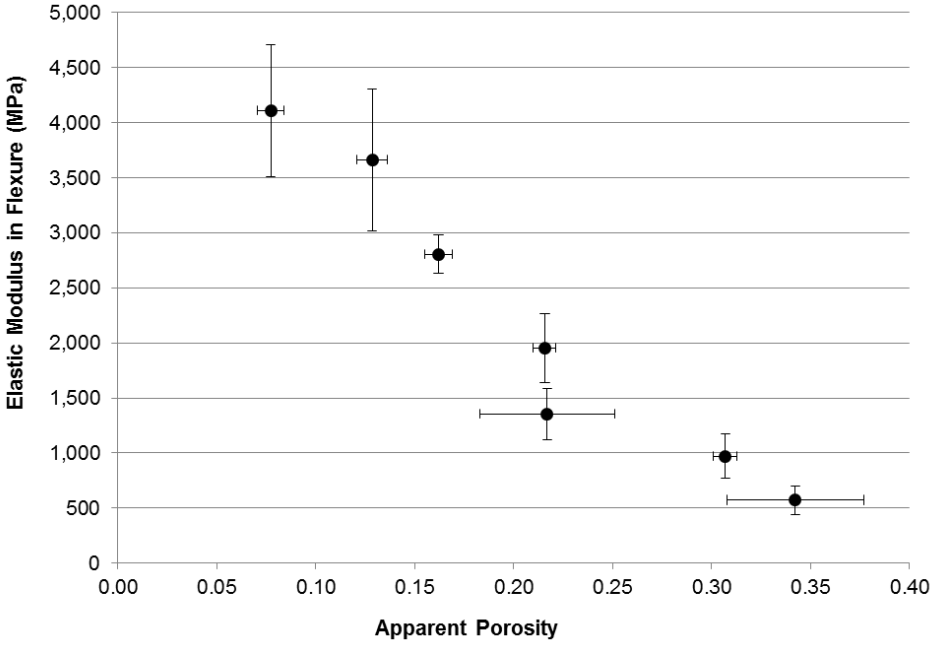

Figure 86. Mean value of the elastic modulus in flexure as a function of porosity.

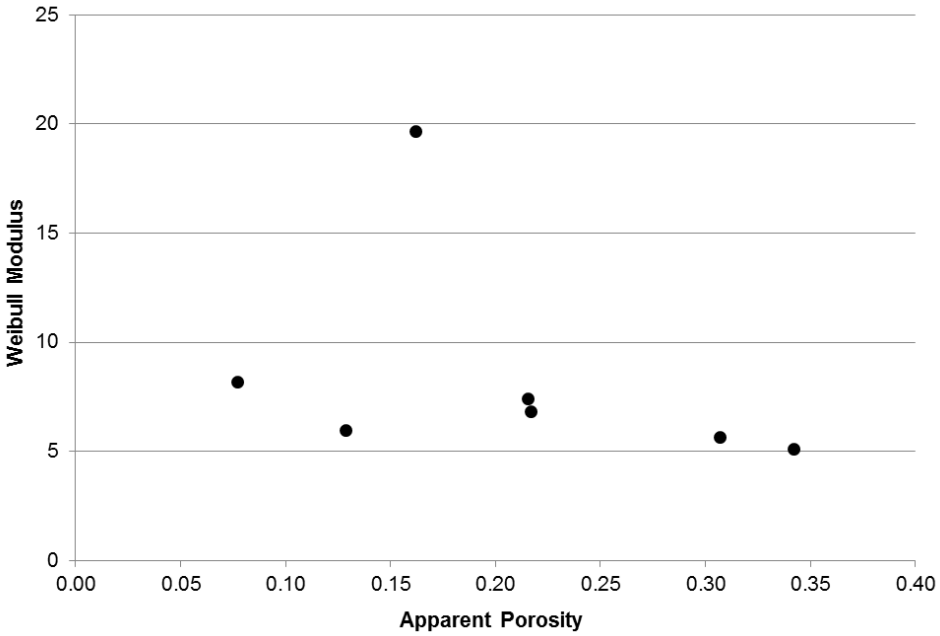

Figure 87. Graphical representation of the Weibull Modulus for the elastic modulus in flexure as a function of apparent porosity.

As expected, the mean value of the elastic modulus can be observed to increase as apparent porosity decreases. As before, variations are much larger at lower porosity, while at higher porosity these variations are minimal. In Figure 87, the value of Weibull modulus is generally between five and ten; however, it can be observed to be as high as ~20. In Figure 88 below, the elastic modulus in flexure is compared to the elastic modulus in compression.

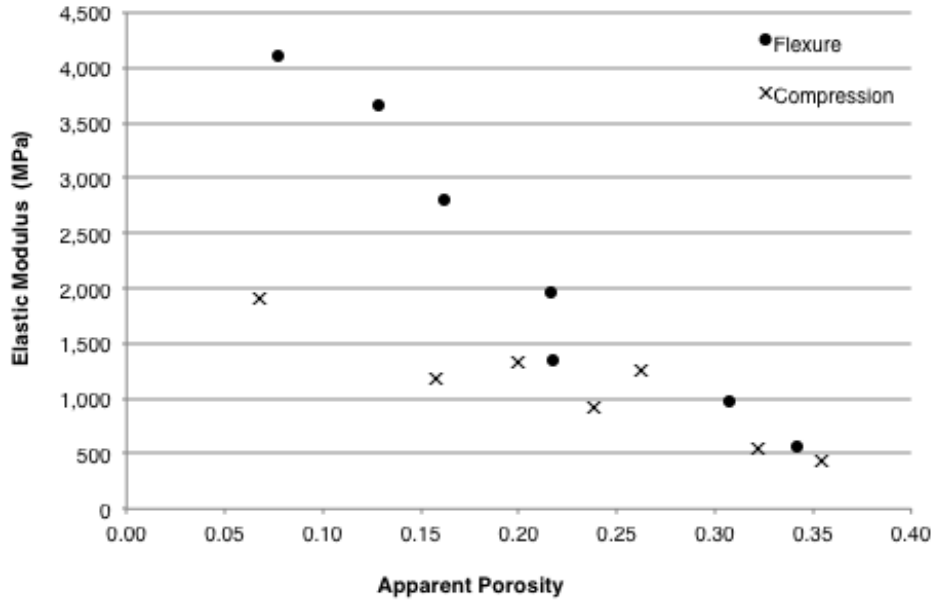

Figure 88. Comparison of calculated values for the elastic modulus in compression and flexure.

Both sets of calculated values follow the same general trend where the elastic modulus increases with decreasing apparent porosity. However, the calculations made from the flexural testing data yielded much higher values compared to the calculations made from the compressive data.

4.3.4. MODELING

In comparing the experimental results to the published zero porosity transverse strength an average value of published data was used. The data was then fit using the exponential model (Eq. 2.8); Gibson and Ashby's models were not used as they were established for compressive strength alone. The results are summarized in the Table 9 below and depicted graphically in

Figure 89. The exponential model fits the experimental data for transverse rupture strength reasonably well; however, the 95% confidence interval is rather large.

Table 9. Summary of curve fitting results for transverse strength, with regression analysis.

Fit Type	Value of Fitting Parameters		R^2	Adjusted R^2	RMSE
	a	b			
Exponential	14.16	--	0.9663	0.9663	7.8858

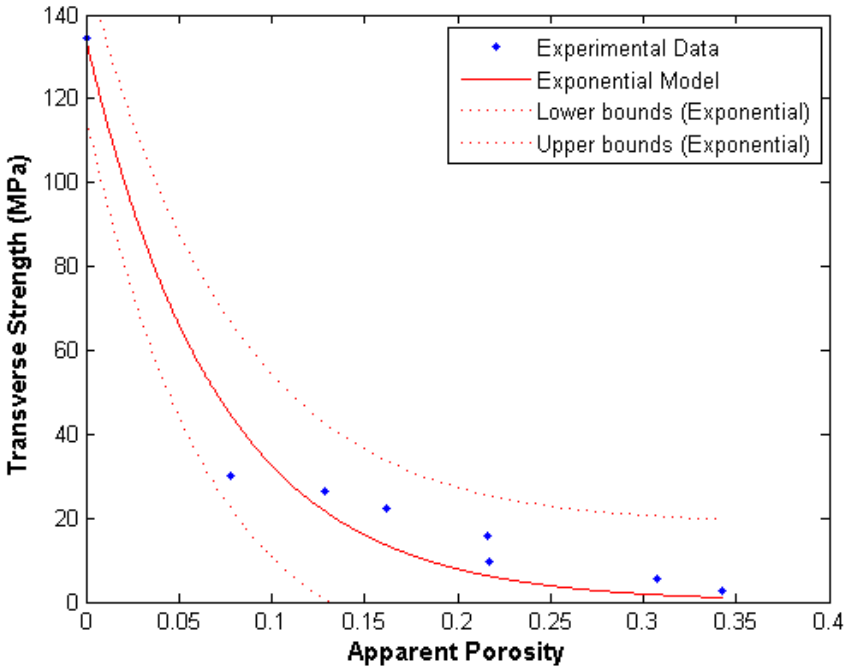

Figure 89. Experimental and published zero porosity data fit with an exponential function.

The experimental data for the elastic modulus in flexure was then fit using established models that relate the elastic modulus to the porosity. A summary of the fitting analysis can be seen in Table 10, where the models are listed in order of adjusted R^2 values from highest to lowest.

Table 10. Summary of fitting results for porosity vs. elastic modulus in flexure, including regression analysis.

Fit Type	Value of Fitting Parameters				R^2	Adjusted R^2	RMSE
	a	b	n	v_o			
Hasselman	159.7	--	--	--	0.9995	0.9995	5.150E+02
Nielsen	0.007125				0.9994	0.9994	5.982E+02
Wang	38.61	-79.01	--	--	0.9972	0.9967	1.392E+03
Spriggs	--	--	33.34	--	0.9947	0.9947	1.754E+03
Wagh-Poeppel-Singh	--	--	32.37	--	0.9945	0.9945	1.799E+03
Phani - Niyogi	0.004062	--	8205	--	0.9947	0.9938	1.894E+03
MacKenzie	9.44	20.02	--	--	0.8050	0.7725	1.152E+04
Brown - Biddulph - Wilcox	2.617	--	--	--	0.4451	0.4451	1.799E+04
Ramakrishnan	--	--	--	0.21	<0.0000	<0.0000	3.507E+04
Hashin	--	--	--	0.24	<0.0000	<0.0000	4.520E+04

As with the compressive testing data, the Hasselman and Nielsen models fit the data most accurately in terms of R^2 values and root mean square error. The models proposed by Wang, Spriggs, Wagh et al. and Phani-Niyogi also fit quite well, while the models proposed by MacKenzie, Brown et al., Ramakrishnan and Hashin fit quite poorly. The models are plotted in Figures 90-99 along with the experimental data.

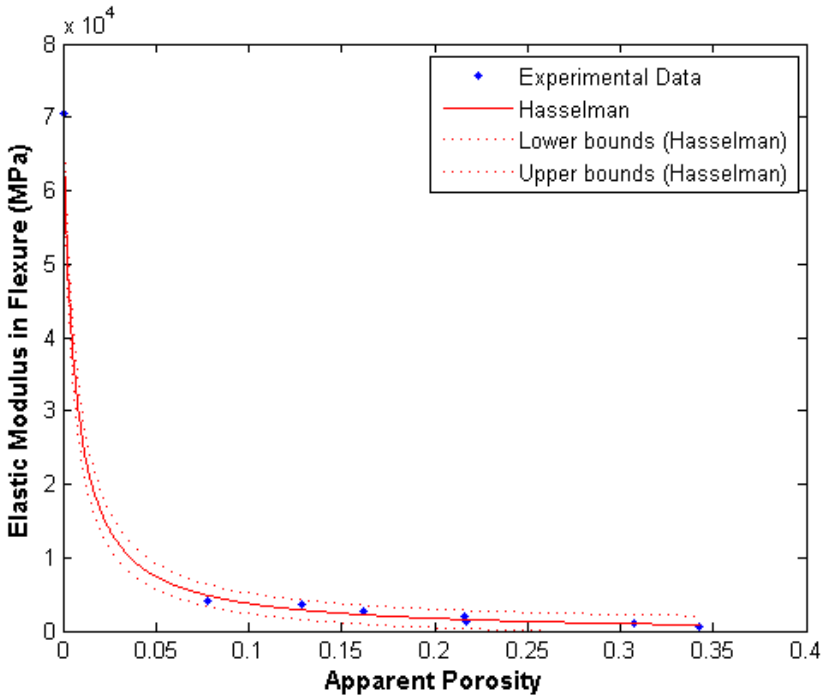

Figure 90. Porosity vs. mean elastic modulus in flexure data fitted with the Hasselman correlation.

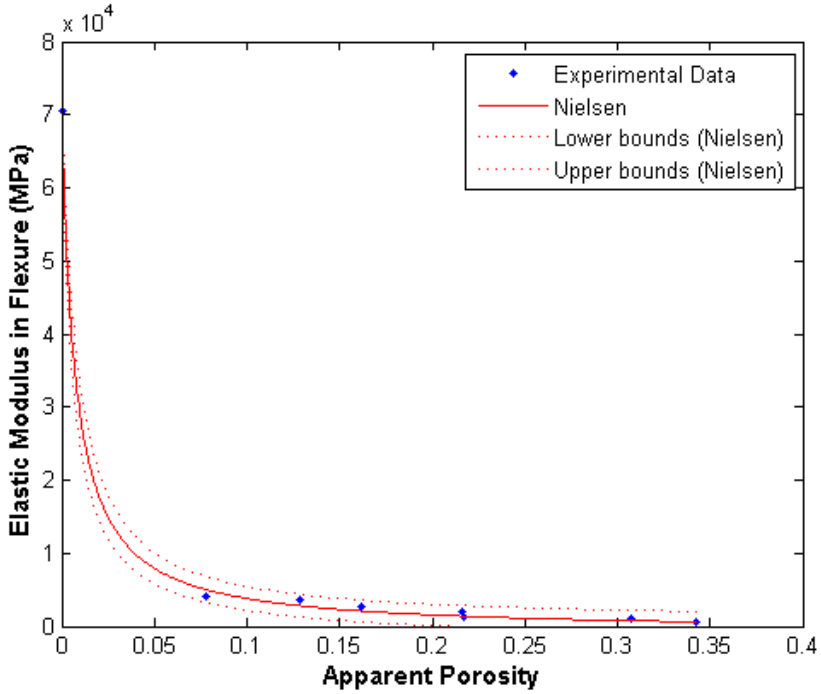

Figure 91. Porosity vs. mean elastic modulus in flexure data fitted with the Nielsen correlation.

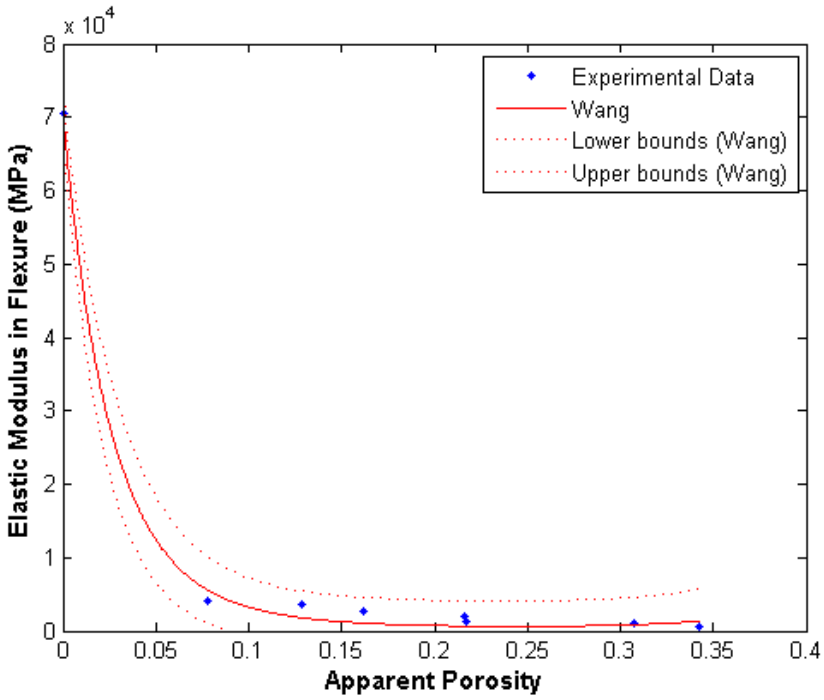

Figure 92. Porosity vs. mean elastic modulus in flexure data fitted with the Wang correlation.

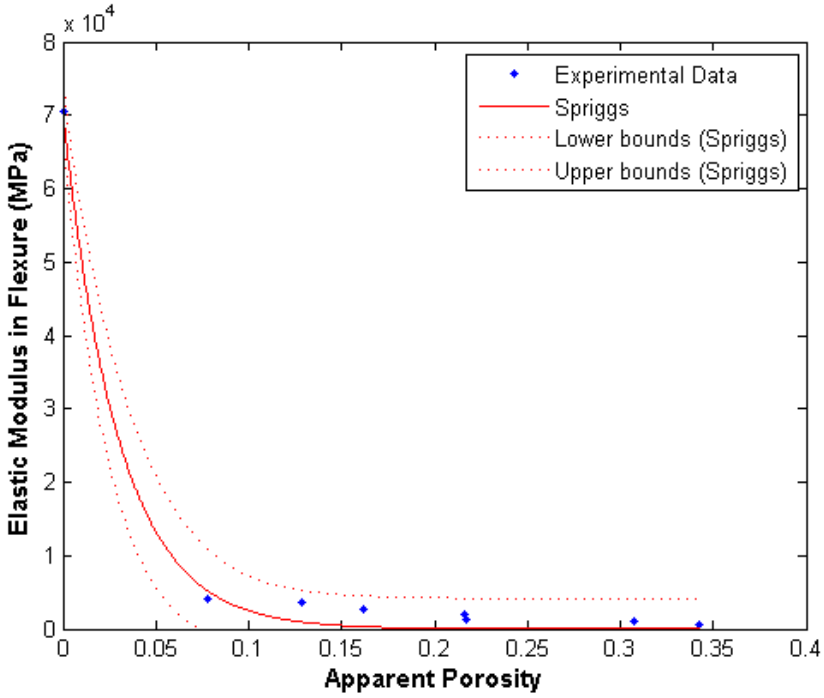

Figure 93. Porosity vs. mean elastic modulus in flexure data fitted with the Spriggs correlation.

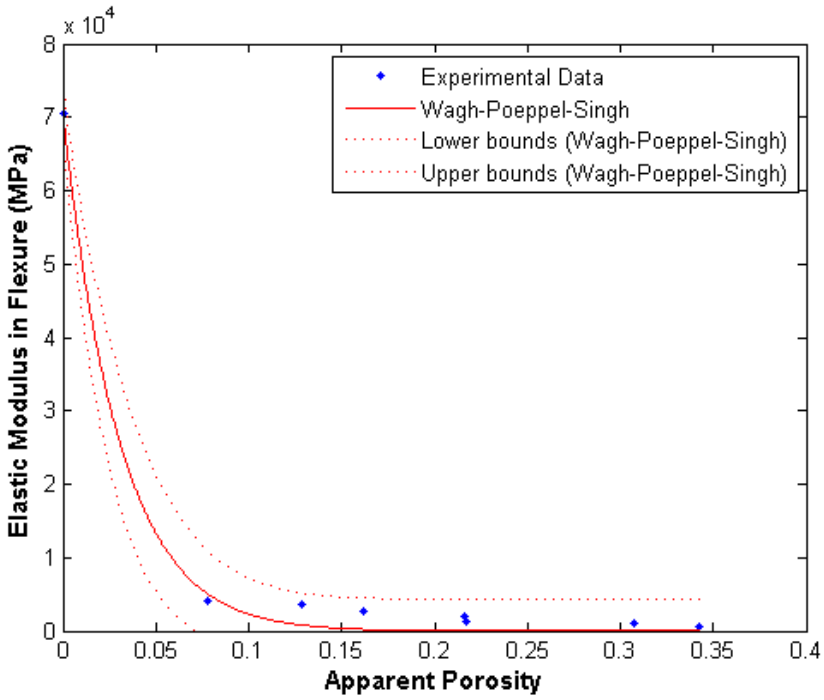

Figure 94. Porosity vs. mean elastic modulus in flexure data fitted with the Wagh-Singh-Poeppel correlation.

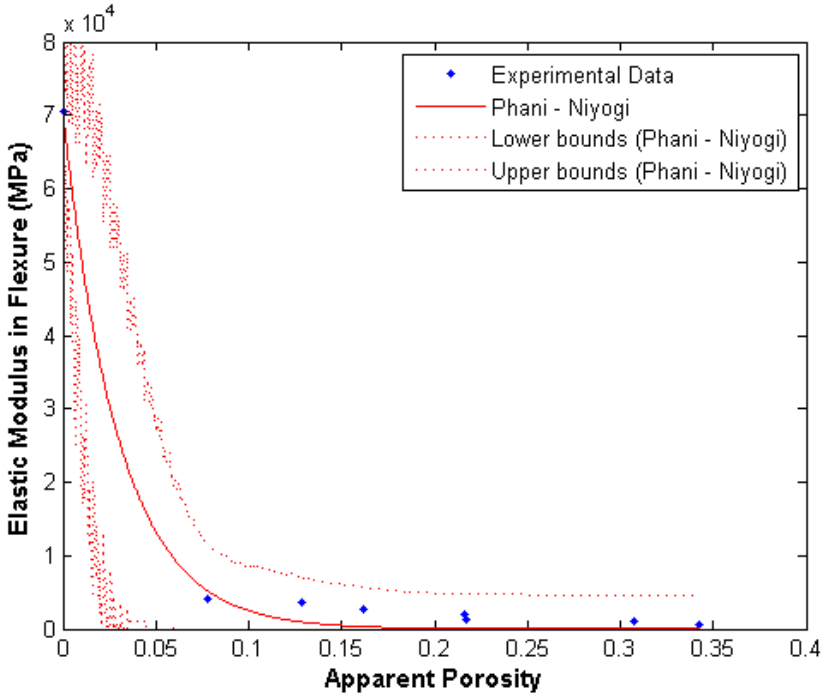

Figure 95. Porosity vs. mean elastic modulus in flexure data fitted with the Phani-Niyogi correlation.

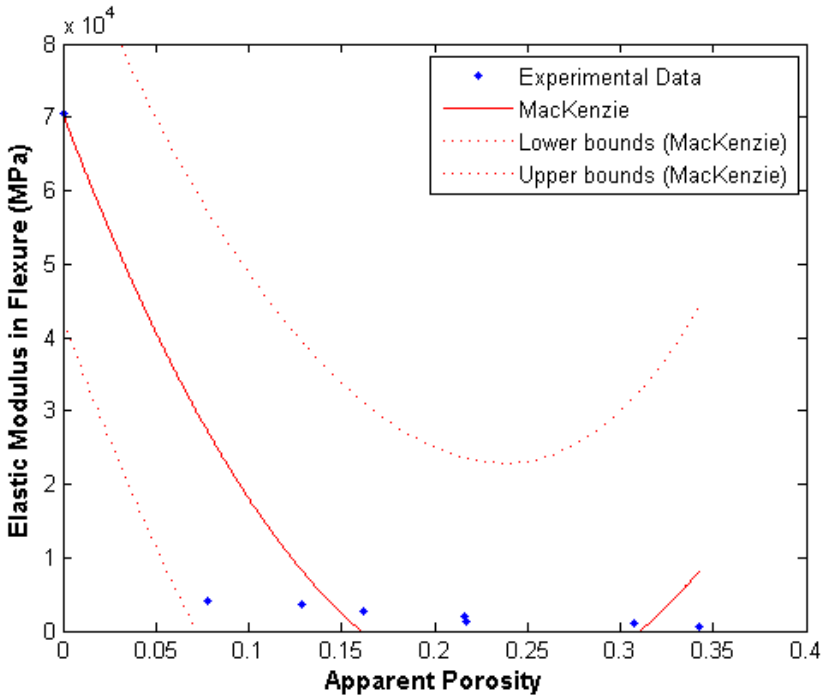

Figure 96. Porosity vs. mean elastic modulus in flexure data fitted with the MacKenzie correlation.

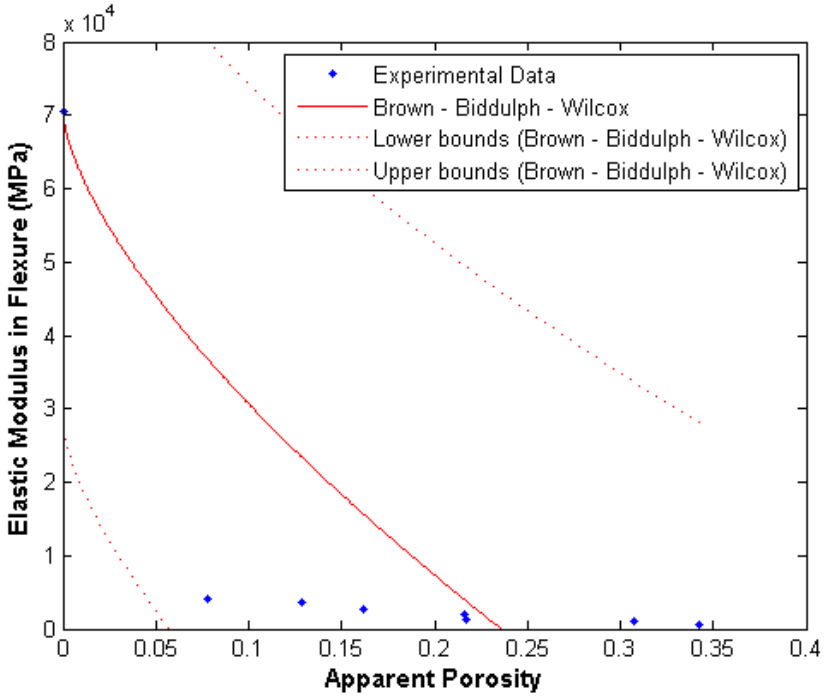

Figure 97. Porosity vs. mean elastic modulus in flexure data fitted with the Brown-Biddulph-Wilcox correlation.

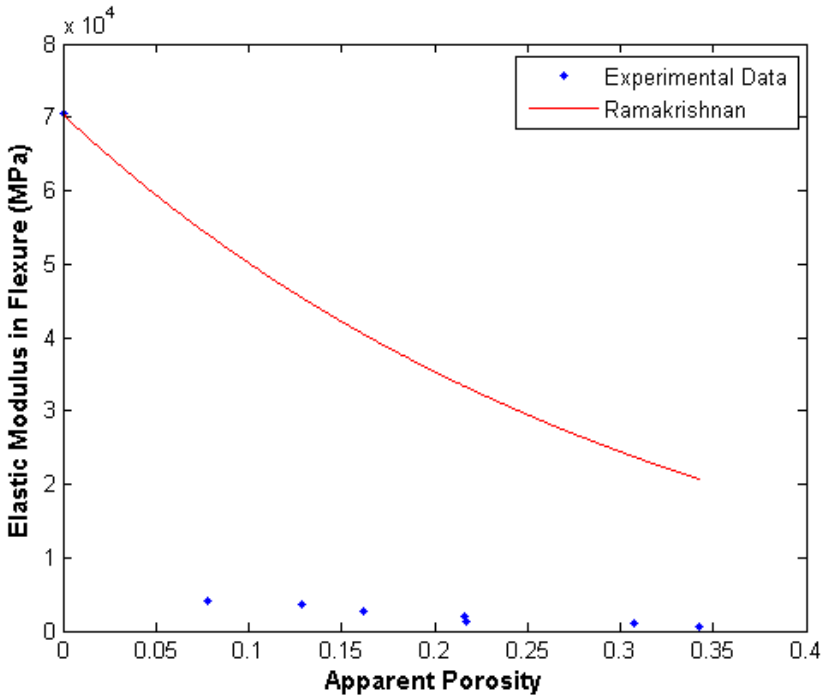

Figure 98. Porosity vs. mean elastic modulus in flexure data fitted with the Ramakrishnan correlation. The 95% confidence bounds are too large to be shown.

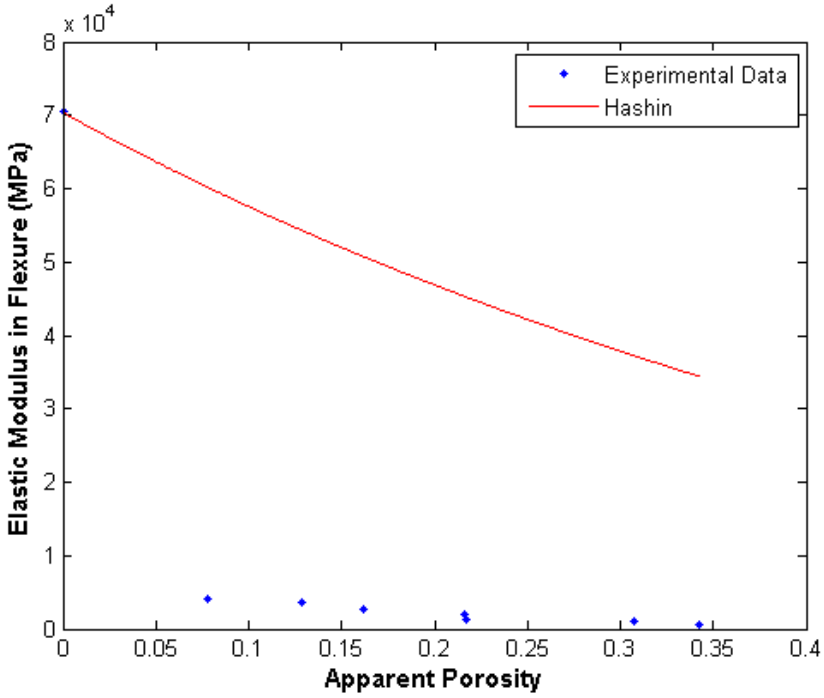

Figure 99. Porosity vs. mean elastic modulus in flexure data fitted with the Hashin correlation. The 95% confidence bounds are too large to be shown.

Through inspection of the preceding figures it appears that Hasselman and Nielsen's correlations again provide the most accurate fit to the data based on the narrow 95% confidence interval and the high adjusted R^2 value. Again, the correlation proposed by Wang fits quite well below 32% apparent porosity, while the Spriggs and Wagh-Singh-Poeppel correlations fit the data throughout the range of experimental values. As with the compressive testing data, the Phani-Niyogi correlation fits well in terms of adjusted R^2 value; however, the 95% confidence bounds appear to be quite erratic in the regions where experimental data is not present. The models proposed by MacKenzie, Brown et al., Ramakrishnan and Hashin fit the data quite poorly. Again the 95% confidence bounds on both the Ramakrishnan and Hashin models are so large that they do not appear on the plots. The Hasselman, Nielsen, Wang, Spriggs, Wagh-Singh-Poeppel and Phani-Niyogi models are compared in Figure 100, where only the 0-20% apparent porosity range is shown.

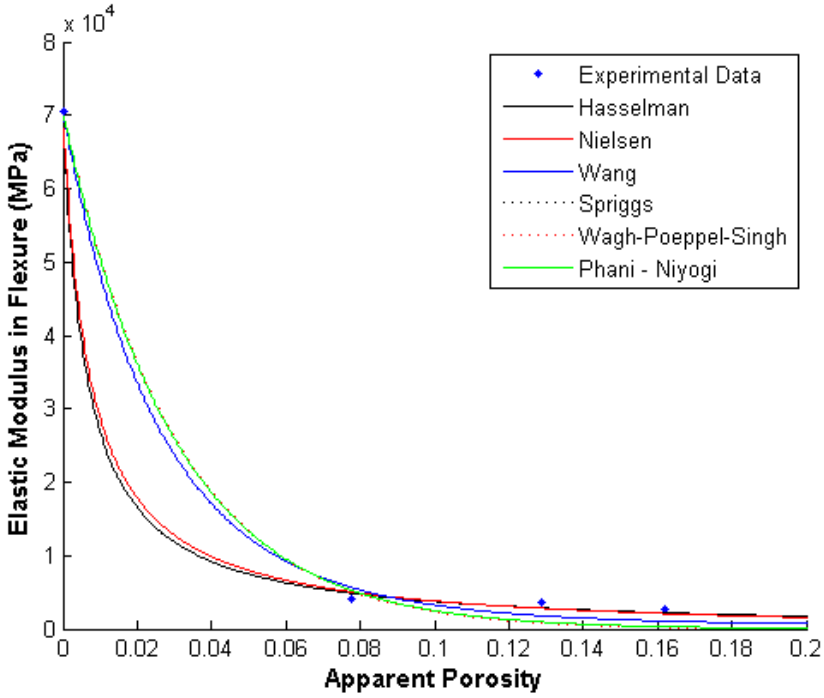

Figure 100. Comparison of the 6 most accurate models for elastic modulus in flexure.

As with the compressive testing data, when the models are compared it appears that the Hasselman and Nielsen models fit the experimental data most accurately. The Wang, Spriggs, Wagh-Singh-Poeppel and Phani-Niyogi models all perform very similarly and differ significantly from the Hasselman and Nielsen models for apparent porosity values below 6%.

CHAPTER 5. DISCUSSION

Through this research, it was demonstrated that contaminated waste glass could be densified successfully through very low temperature sintering. The peak firing temperatures can be varied between 705°C and 790°C to produce materials that exhibit a broad range of apparent porosity. The volumetric shrinkage that occurs through the densification process is directly related to this porosity and within this temperature the relationship appears to be linear ($Shrinkage = 0.2546T - 172.42$). This can be said of the relationships between apparent porosity and shrinkage ($P = -1.1871 * Shrinkage + 43.452$) and between porosity and bulk density ($\rho = -0.0216P + 2.3154$) as well. However, some discrepancies were observed and they may have effected subsequent investigation into the mechanical behavior of the materials to some degree.

The specimen geometry did vary slightly with temperature. At higher temperatures dimensional distortion was more pronounced and the upper and lower faces of the specimens had a tendency to become non-planar. In addition, significantly more shrinkage was exhibited towards the top face of the specimens, resulting in trapezoidal cross sections. These discrepancies may have resulted from a temperature gradient within the kiln. However, because the specimen's thickness is quite small when compared to the height of the furnace chamber, it is more likely that this was caused by non-uniform heat transfer rates, particularly through the bottom surface of the specimen. These dimensional distortions were also more pronounced in flexure specimens. These specimens had a different aspect ratio than the compression specimens, which may have resulted in different, and perhaps non-uniform, heat transfer characteristics.

In addition, the when the apparent porosity was plotted against volumetric shrinkage, the data were somewhat scattered. This could result from the calculation methods for the volumetric

shrinkage and apparent porosity. Volumetric shrinkage was calculated from seven measurements taken before and after densification. The dimensional distortion of the specimens may have introduced error into these calculations. Further, the procedure for calculating the apparent porosity, as detailed in the ASTM C373, accounts only for the volume of open pores present in the specimen. Pores that are isolated from the porous network, e.g. closed pores, would not be taken into account and as such, the true porosity may differ from the calculated apparent porosity.

Moreover, at ~15% volumetric shrinkage the apparent porosity exhibits a high degree of variability, as evidenced by the large standard deviations. The peak firing temperature employed to achieve 15% volumetric shrinkage is very close to the average published crystallization temperature of clear soda lime silicate glass. The raw materials used in this research were collected from the municipal waste stream and as such, the composition and color of the glass particles varied significantly. This could mean that localized crystallization was occurring between particles with lower crystallization temperatures, while crystallization phenomena was not yet occurring in adjacent particles, which may have had slightly higher crystallization temperatures. This could attribute to the observed variation in apparent porosity.

5.1. Compressive Strength

The results of compressive testing show that compressive strength and porosity are inversely related, which was expected. Further, the compressive behavior agreed well with Duckworth's exponential model. However, the models proposed by Gibson and Ashby fit quite poorly. As these models were developed for cellular materials, this is not altogether surprising. The material under investigation cannot be characterized as strictly open or closed celled. In

addition, given the random geometry and distribution of the glass prior to densification, a highly ordered, cellular structure was not expected.

Analysis of the stress-stress data shows that specimens do not behave in a manner consistent with brittle solids, where unloading occurs abruptly at the point where maximum stress is achieved. Nor do they behave similarly to cellular foams, in which stress tends to plateau after the yield stress is achieved[6]. Instead the specimens appear to experience unloading in stages, perhaps due to cleavage in discrete areas on the fracture surface. Further, discontinuities and load drops were seen throughout both the elastic and plastic portions of the curves. This behavior is not in agreement with the general behavior of dense ceramics, however it is common in porous materials. In the less dense specimens, the load drops are likely due to fractures in the necks between particles, while in more dense specimens they may be due to the creation and growth of small cracks near the grain boundaries.

Through calculation of the Weibull mean and standard deviation, it was observed that the standard deviation in compressive strength was related to apparent porosity. Specimens with lower apparent porosity were produced at higher peak firing temperature and these temperatures are within the crystallization range. Therefore, it is likely that the particles have begun to coalesce into grains, but full crystallization has not yet been achieved. Were that the case, the degree of crystallization may vary and as a result, a range of grain sizes may be present. This would affect the ease with which small cracks could propagate through the specimen. Hence, either incomplete or inconsistent crystallization may have accounted for the variation in strength present at lower apparent porosity.

The values of the Weibull modulus were scattered between roughly four and eleven and no clear relationship was seen between the apparent porosity and Weibull modulus. In general,

these values are rather low. Common structural ceramics typically exhibit Weibull moduli of approximately 10 and current research endeavors to raise this to 20[50]. The low values could be attributed to inconsistencies in specimen production. They may also have resulted from premature failure brought about by uneven loading of the specimen during testing.

The results of testing are very encouraging when compared to ASTM standards for common structural ceramic building products. The requirements for compressive strength vary with application and regional considerations. In facing brick and building brick products are expected to withstand between 10 and 21 MPa before failure, while paving brick products requirements range from 21 to 56 MPa. Through compressive testing it was determined that compressive strength values between 13.8 and 150.8 MPA can be achieved at peak firing temperatures in the range of ~720°C and 790°C.

5.2. Modulus of Rupture

The results of flexural testing followed similar trends as those discussed above for the compressive data. Transverse rupture strength and porosity fit the exponential model quite well and the stress-strain behavior was characterized by discontinuities and load drops. Under flexural loads the material behaved in a manner consistent with both brittle solids and porous materials. Unloading occurred abruptly, immediately following the point of maximum stress. In addition, the transverse strength was substantially higher than the compressive strength, as expected.

The Weibull analysis yielded Weibull modulus values between 10 and 18, which is within the common range for structural ceramics. Again the Weibull moduli were somewhat scattered and the potential reasons for this are discussed above.

Because structural ceramics are brittle in nature, flexural requirements are not as common for building materials. The most common application is roof tiles, which are required to

withstand 7.5 to MPa before failure. Through flexural testing it was determined that transverse strength values between 10.6 and 15.3 MPA can be achieved at peak firing temperatures in the range of ~705°C and 790°C.

5.3. Elastic Modulus

Inspection of the stress-strain curves shows that during initial loading, the behavior is quite non-linear. There are several possible causes for this behavior. First, imperfections in specimen geometry may have contributed to the observed non-linearity. Variations in geometry may have led to poor or uneven contact between the bearing surface and the specimen. Were this the case, irregularities may have resulted in localized fracture, which would have skewed the results. Second, during initial loading, the structure of the specimen may have undergone reorganization. This is a phenomenon common to sintered materials and under relatively small loads the pore structure becomes more compact through small-scale deformation of particles, grains or ligaments. Third, the non-linearity in the stress-strain behavior may have been caused by contact readjustment; the specimen may have shifted slightly on the test fixture during initial loading. However, it is also possible that this material cannot be characterized by linear elastic behavior at all.

Under compressive loading the Weibull analysis of the elastic modulus data generally yielded values of the Weibull moduli ranging from six to twelve, but a value of ~14 was calculated at 32.2% apparent porosity. Under flexural loading the Weibull analysis of the elastic modulus data generally yielded values of the Weibull moduli ranging from five to ten, but a value of ~20 was calculated at 16.2% apparent porosity. No general trend was observed and overall variation was larger than typically expected in structural ceramics.

The data obtained through both compressive and flexural data fit a number of theoretical models for predicting the elastic modulus based on the porosity. The models proposed by Hasselman and Nielsen proved to be most accurate in predicting the elastic behavior. If the equations are reorganized, Nielsen's model is quite similar to Hasselman's. In general, models that rely on the assumption of spherical particles tended to accurately predict behavior, while models that make use of the Poisson's ratio of the zero porosity material fit very poorly.

Evaluation of the elastic modulus calculations showed that values calculated from the compressive and flexural data do not agree. It was thought that the stochastic nature of the pore distribution and morphology combined with the isotropic behavior of zero porosity soda-lime silicate glass would result in composite materials that exhibited quasi-isotropic behavior. From this observation it may be hypothesized that this materials is in fact anistropic. However, it is very likely that the observed dimensional distortion of specimens, particularly in the lower porosity range, had a significant impact on the results of compressive testing. Potential anisotropy may also be caused by the interactions of contaminants on a molecular level. This may play an interesting role in future research.

5.4. Fractography

Specimens were photographed immediately following compressive testing and a representative sample of these micrographs can be seen in Figure 101, on the following page.

(a) (b) (c)

Figure 101. Specimens after compressive testing. (a) high porosity specimen (b) typical specimen (c) low porosity specimen

The specimen in Figure 101a is representative of very high porosity specimens, which were partially reduced to powder through compressive testing. The specimen in Figure 101b is representative of the majority of specimens tested. In general, these specimens exhibited a series of cracks radiating out from near their center, which is more consistent with specimens that have been subjected to impact testing. This may indicate that the load was applied unevenly. In fact many of the specimens exhibited non-planar surfaces and slight cupping after densification. Given that the top and bottom bearing surfaces of compression testing apparatus are planar, full contact would not be established and the force would be applied near the center of the specimen on one face and along the outside edges of the opposite face. This could account for the fracture pattern seen in Figure 101b. The specimen in Figure 101c is representative of low porosity specimens, which underwent densification at higher temperatures. It can be seen that fracture surface is at a roughly 45° to the direction of the applied load.

The photographs in Figure 102 show representative specimens of flexural testing. Fracture occurred between the support spans and fracture planes were more consistent with the 45° angle expected through theoretical analysis of uniaxial testing.

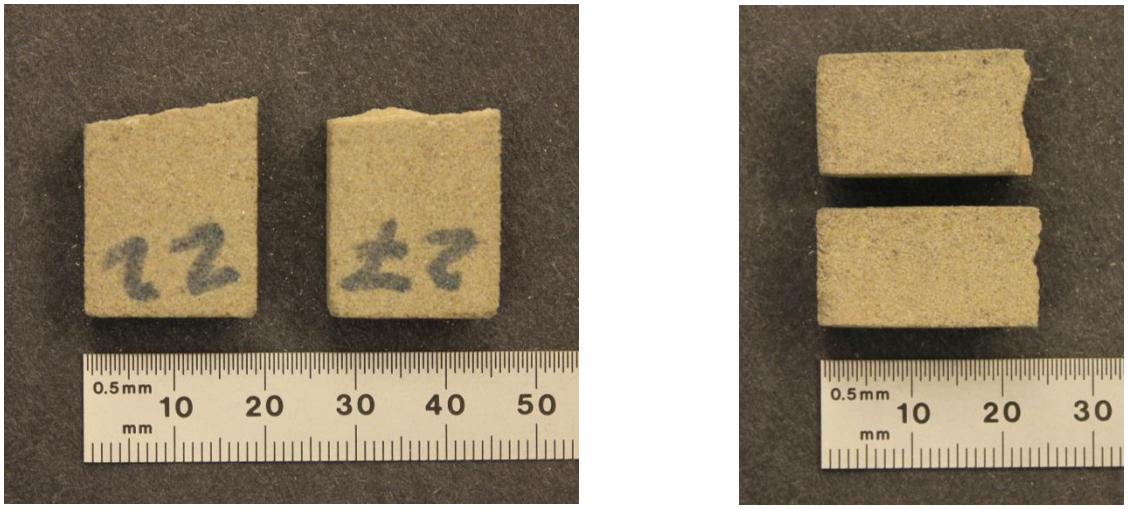

(a) (b)

Figure 102. Characteristic fracture angle exhibited by specimens following flexural testing. (a) Top (b) Side

Roughly half of the specimens exhibited angled fracture surfaces, as shown in Figure 102a, while the other half exhibited relatively vertical fracture surfaces, as seen in Figure 102b. Following flexural testing, the fracture surfaces of test specimens were evaluated through microscopy. SEM micrographs of two representative specimens are shown in Figures103 and 104, on the following two pages.

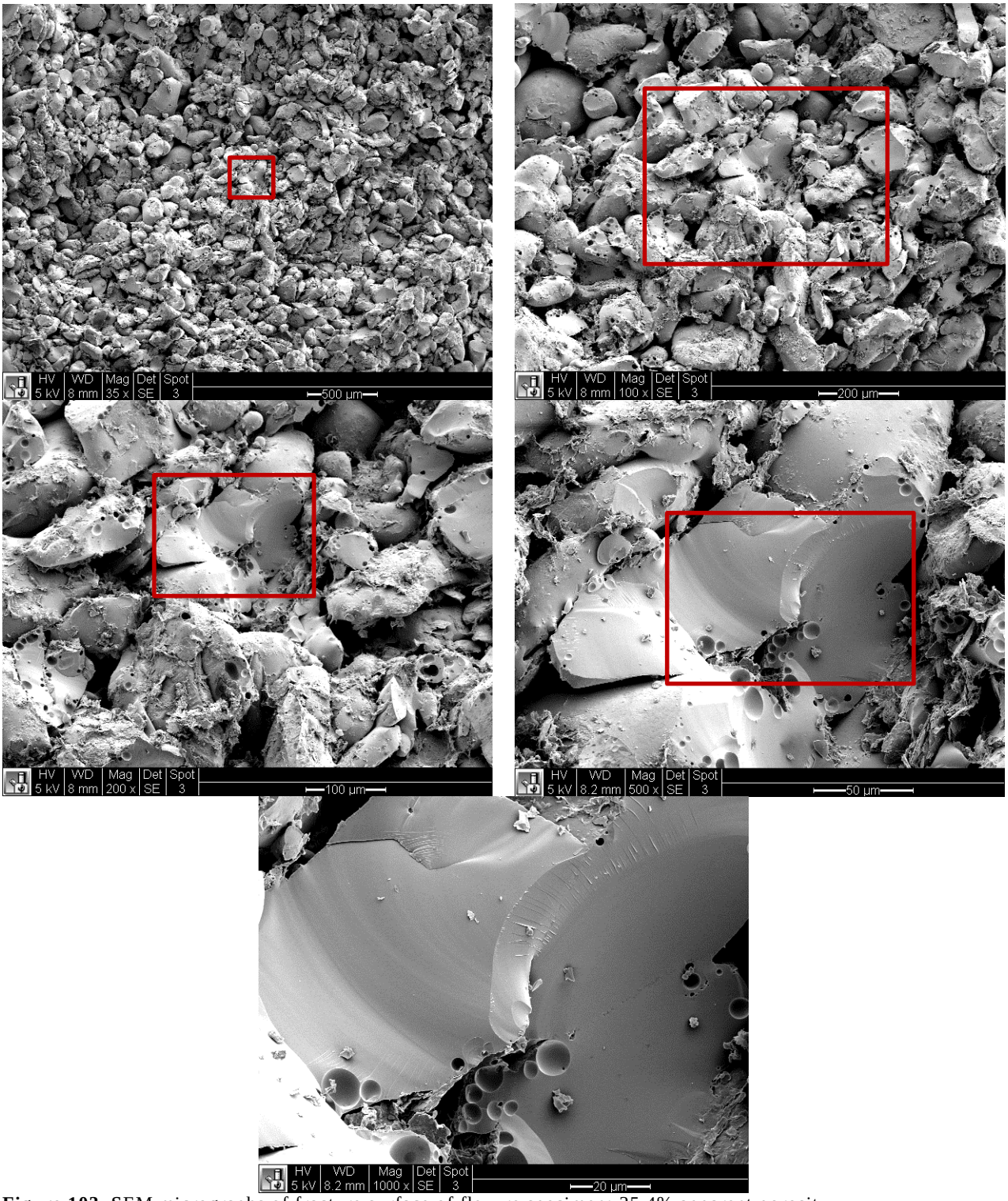

Figure 103. SEM micrographs of fracture surface of flexure specimen: 35.4% apparent porosity.

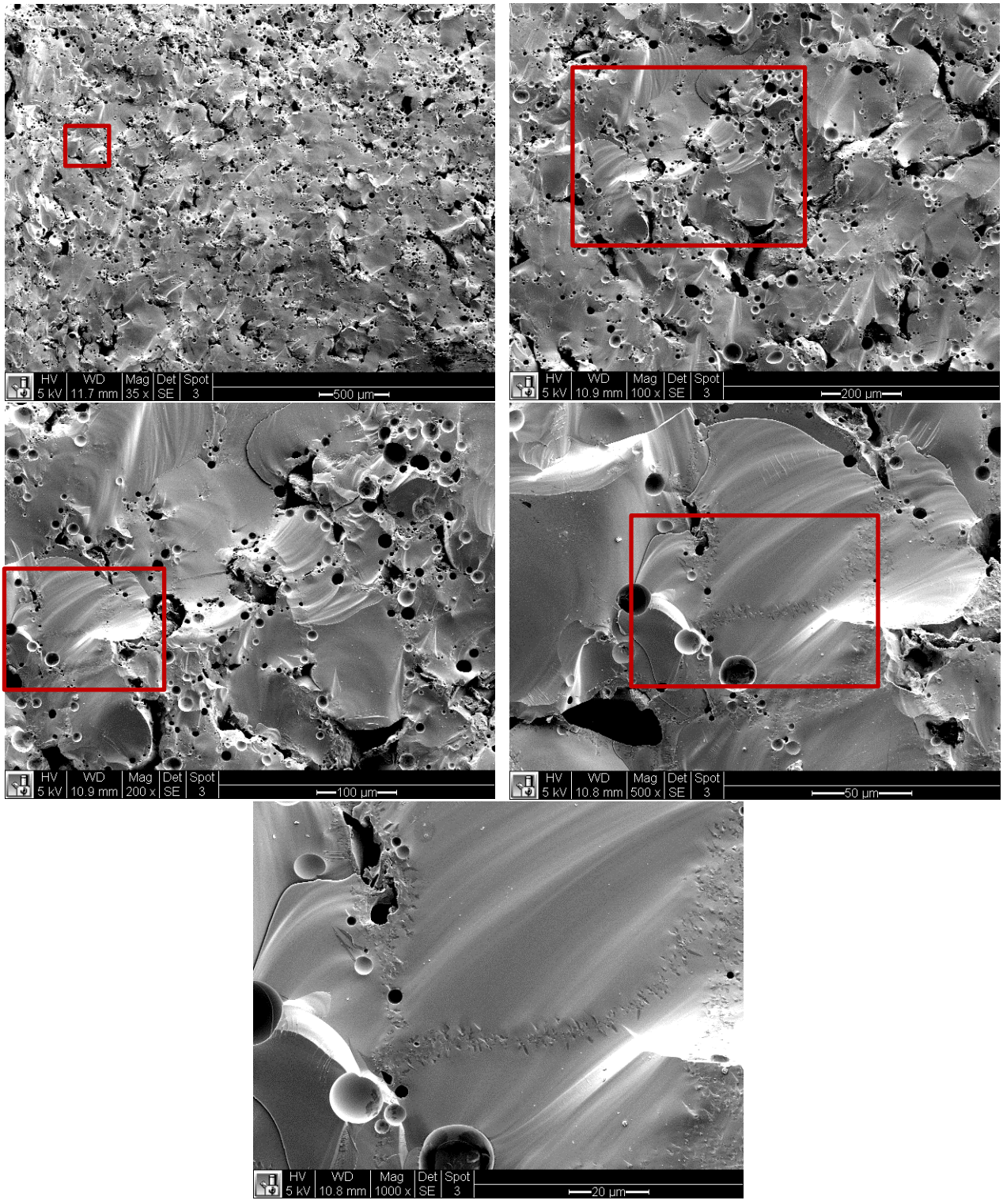

Figure 104. SEM micrographs of fracture surface of flexure specimen: 7.7% apparent porosity.

Analysis of the micrographs in Figures 103 and 104 reveals a marked difference in the microstructure and characteristic fracture behavior of the two specimens. The high apparent porosity specimen (Figure 103) can be characterized by discrete particles that exhibit minimal deformation from their cold state and are bonded through somewhat sparely distributed neck formation. The occurrence of necking appears to be generally uniform throughout the specimen, with cleavage occurring both at the necks and through the particles themselves. Some porosity can be seen near the necks, which was expected given the broad particle size distribution of the waste glass feedstock. In sintering processes, as small particles are bonded to larger ones, small voids become isolated and form micro-pores. As the sintering process continues the micro-pores diffuse out of the solid and converge into the porous network.

This phenomenon is visible in the SEM micrographs of the low apparent porosity specimen (Figure 104). The sintering process has advanced significantly and the microstructure can be characterized by grains rather than particles. Micro-pores are still present, but the majority have diffused to grain boundaries or have converged to form larger pores. In general, bonding is complete and fracture can be characterized as mostly transgranular. In many cases fracture was initiated at the pores, where stress concentration affects dominate.

CHAPTER 6. CONCLUSIONS

Overall the results of this investigation are very promising. Based on the experimental investigation the following conclusions can be made:

1. Marchelli and Prabhakar's process for creating macro-scale porous materials, from recycled glass results in predictable physical and mechanical behavior.
2. Volumetric shrinkage, apparent porosity, and bulk density follow linear relationships within the 705°C and 790°C range of peak firing temperatures.
3. Under compressive loads, the material does not exhibit stress-strain behavior consistent with brittle solids or cellular porous material.
4. Both compressive and transverse strength can be related to apparent porosity through an exponential relationship. Comparison of experimental compressive testing data to models for cellular materials yielded poor results. This is consistent with the fact that the material does not exhibit an ordered pore structure composed solely of open or closed cells.
5. Elasticity and apparent porosity can be related through established two-phase models that assume that the continuous phase is composed of spherical particles. However, models based on the Poisson's ratio of the zero porosity material fit very poorly.
6. Calculations for the elastic modulus obtained through compressive and flexural testing do not agree. At this stage, it is unclear if this was the consequence of irregular specimen geometry or inherent anisotropy. The effects of contamination may also have played a role in this observation.
7. The densification process used during experimentation is compatible with contaminated waste glass. The presence of micro-scale organic and inorganic contaminants has not

prevented sintering and through manipulation of peak firing temperature, sufficient strength can be achieved for construction application.

8. The SEM micrographs show that a significant degree of crystallization occurs within the 705°C to 790°C range. However, full crystallization is not achieved and voids are observed near grain boundaries. In many cases, cracks appear to initiate between voids, as expected.

9. High strength materials can be created at much lower temperatures than previously thought, which results in end products with very low embodied energy. This would reduce both greenhouse gas emissions and manufacturing costs.

CHAPTER 7. RECOMMENDATIONS FOR FUTURE WORK

1. Characterization of the mechanical behavior of this material would benefit from 4-point bending tests, rather than 3-point. In the 4-point bend test, shear forces between the two loading forces is zero and bending stresses are distributed over the entire area between the two loads. Because the area over which bending stresses are applied is larger, the probability of encountering a defect is larger as well. Hence, the 4-point method yields more realistic values of transverse rupture strength.

2. Analysis of the material using the three-parameter Weibull distribution would provide more reliable information regarding the probability of failure in components as this method provides more robust results. In addition, inspection of the Weibull probability plot for compressive strength (Appendix B) indicates that a linear fit may not be applicable, particularly in the lower porosity ranges.

3. An investigation of potentially non-linear elastic stress-strain behavior is warranted. This would be undertaken by first re-evaluating the stress-strain behavior on planar specimens, so that errors due to geometric variations would be minimized.

4. The flexural behavior of larger specimens is currently unknown. It is widely recognized that the transverse rupture strength of porous materials does not remain constant with changes in specimen size. A thorough investigation of this phenomenon in porous glass materials has not yet been performed.

5. Although established theoretical models have been shown to fit the experimental well. The accuracy of the models has not been evaluated for materials that exhibit <6% apparent porosity. Testing on additional specimens with lower porosity will aid in this

evaluation and it is possible that a more accurate, phenomenological model can be developed. This will likely involve finite element methods.

6. Very little work has been performed with contaminated waste glass. Successfully using waste glass as a primary feedstock will require a comprehensive understanding of how contaminants in the supply will affect the microstructure and mechanical properties.

7. Although CIP methods are utilized by industry, the majority of masonry manufacturers have moved towards extrusion. CIP and extrusion have many aspects in common and this transition has been made with numerous masonry products. However, this material will present unique challenges due to the brittle nature of glass.

REFERENCES

1. EPA. *Glass*. Common Wastes & Materials June 21, 2012 [cited 2012; Available from: http://www.epa.gov/waste/conserve/materials/glass.htm.
2. Marchelli, G.P., R. 2011. PCT Patent 2011/153369. "Porous glass articles formed using cold work process"
3. Mencík, J., *Strength and fracture of glass and ceramics*. 1992, Amsterdam; New York: Elsevier.
4. Harper, C.A., *Handbook of ceramics, glasses, and diamonds*. 2001, New York: McGraw-Hill.
5. Bengisu, M., *Engineering ceramics*. 2001, Berlin; New York: Springer.
6. Gibson, L.J. and M.F. Ashby, *Cellular solids : structure and properties*. 1997, Cambridge; New York: Cambridge University Press.
7. McLellan, G.W. and E.B. Shand, *Glass engineering handbook*. 1984, New York: McGraw-Hill.
8. Bansal, N.P. and R.H. Doremus, *Handbook of glass properties*. 1986, Orlando: Academic Press.
9. German, R.M., *Sintering Theory and Practice*. 1996, New York: John Wiley & Sons, Inc.
10. Kuczynski, G.C. *Sintering processes*. in *International Conference on Sintering Related Phenomena*. New York: Plenum Press.
11. Rahaman, M.N., *Sintering of ceramics*. 2008, Boca Raton, FL: CRC Press.
12. Scott, W.D., *Densification, Crystallization, and Sticking Behavior of Crushed Waste Glass Sintered in Refractory Molds with Release Agents*, 2000, Clean Washington Center: Seattle.
13. Djohari, H., J.I. Martínez-Herrera, and J.J. Derby, *Transport mechanisms and densification during sintering: I. Viscous flow versus vacancy diffusion.* Chemical Engineering Science, 2009. **64**(17): p. 3799-3809.
14. Hibbeler, R.C., *Mechanics of materials*. 1997, Upper Saddle River, N.J.: Prentice Hall.
15. Dowling, N., *Mechanical behavior of materials: engineering methods for deformation, fracture, and fatigue.* 1993, Upper Saddle River: Prentice Hall.
16. Enke, D., F. Janowski, and W. Schwieger, *Porous glasses in the 21st century—a short review.* Microporous and Mesoporous Materials, 2003. **60**(1–3): p. 19-30.
17. Haux, E.H. "Method of Preparing Cellular Materials"
18. Ford, D. "Nodulated Cellular Glass and Method of Forming"
19. Spiridonov, Y.A. and L.A. Orlova, *Problems of Foam Glass Production.* Glass and Ceramics Glass and Ceramics, 2003. **60**(9/10): p. 313-314.
20. Manevich, V. and K. Subbotin, *Mechanism of foam-glass formation.* Glass and Ceramics, 2008. **65**(5-6): p.5-6.
21. Manevich, V. and K. Subbotin, *Foam glass and problems of energy conservation.* Glass and Ceramics, 2008. **65**(3-4): p. 3-4.
22. Demidovich, B.K., et al., *NEW PRODUCTION LINE FOR THE MANUFACTURE OF HIGH QUALITY FOAM GLASS.* Glass and Ceramics (English translation of Steklo i Keramika), 1972. **29**(9-10): p. 651-654.
23. Éidukyavichus, K.K., et al., *Use of cullet of different chemical compositions in foam glass production.* Glass and Ceramics (English translation of Steklo i Keramika), 2004. **61**(3-4): p. 77-80.
24. Tulyaganov, D.U., et al., *Preparation and characterization of high compressive strength foams from sheet glass.* Journal of Porous Materials, 2006. **13**(2): p. 133-139.
25. Bernardo, E., et al., *Recycling of waste glasses into partially crystallized glass foams.* Journal of Porous Materials, 2010. **17**(3): p. 359-365.
26. Bernardo, E. and G. Scarinci, *Fast sinter crystallisation of waste glasses.* Advances in Applied Ceramics: Structural, Functional & Bioceramics, 2008. **107**(6): p. 344-349.
27. Bernardo, E., E. Bonomo, and A. Dattoli, *Optimisation of sintered glass–ceramics from an industrial waste glass.* Ceramics International, 2010. **36**(5): p. 1675-1680.
28. Rosli, N.R., et al., *Characterisation and properties of sintered recycled glass utilising CIP method*, 2011. p.245-250.
29. Schabbach, L.M., et al., *Integrated approach to establish the sinter-crystallization ability of glasses from secondary raw material.* Journal of Non-Crystalline Solids, 2011. **357**(1): p. 10-17.
30. Mackenzie, J.K., *The Elastic Constants of a Solid Containing Spherical Holes.* Proceedings of the Physical Society of London Section B, 1950. **63**(361): p. 2-11.
31. Ryshkewitch, E., *Compression Strength of Porous Sintered Alumina and Zirconia.* J American Ceramic Society Journal of the American Ceramic Society, 1953. **36**(2): p. 65-68.

32. Duckworth, W., *Discussion of Ryshkewitch Paper by Winston Duckworth**. J American Ceramic Society Journal of the American Ceramic Society, 1953. **36**(2): p. 68-68.
33. Spriggs, R.M., *Expression for Effect of Porosity on Elastic Modulus of Polycrystalline Refractory Materials, Particularly Aluminum Oxide.* J American Ceramic Society Journal of the American Ceramic Society, 1961. **44**(12): p. 628-629.
34. Knudsen, F.P., *Dependence of Mechanical Strength of Brittle Polycrystalline Specimens on Porosity and Grain Size.* J American Ceramic Society Journal of the American Ceramic Society, 1959. **42**(8): p.376-387.
35. Hasselman, D.P.H., *On the Porosity Dependence of the Elastic Moduli of Polycrystalline Refractory Materials.* Journal of the American Ceramic Society, 1962. **45**(9): p. 452-453.
36. Hashin, Z., *Citation Classic - the Elastic-Moduli of Heterogeneous Materials.* Current Contents/Engineering Technology & Applied Sciences, 1988(39): p. 14-14.
37. Boccaccini, A.R. and Z. Fan, *A new approach for the Young's modulus-porosity correlation of ceramic materials.* Ceramics International, 1997. **23**(3): p. 239-245.
38. Wang, J.C., *Young's modulus of porous materials.* Journal of Materials Science, 1984. **19**(3): p. 801-808.
39. Phani, K.K. and S.K. Niyogi, *Young's modulus of porous brittle solids.* Journal of Materials Science, 1987. **22**(1): p. 257-263.
40. Wagh, A.S., R.B. Poeppel, and J.P. Singh, *Open pore description of mechanical properties of ceramics.* Journal of Materials Science, 1991. **26**(14): p. 3862-3868.
41. Ramakrishnan, N., *Effective elastic moduli of porous ceramic materials.* Journal of the American Ceramic Society, 1993. **76:11**: p. 2745-2752.
42. Nielsen, L.F., *Elasticity and Damping of Porous Materials and Impregnated Materials.* J American Ceramic Society Journal of the American Ceramic Society, 1984. **67**(2): p. 93-98.
43. Nielsen, L.F., *Strength and Stiffness of Porous Materials.* Journal of the American Ceramic Society, 1990. **73**(9): p. 2684-2689.
44. Lu, G., G.Q. Lu, and Z.M. Xiao, *Mechanical Properties of Porous Materials.* Journal of Porous Materials, 1999. **6**(4): p. 359.
45. Brown, S.D., R.B. Biddulph, and P.D. Wilcox, *A Strength-Porosity Relation Involving Different Pore Geometry and Orientation.* Journal of the American Ceramic Society, 1964. **47**(7): p. 320-322.
46. ASTM, *C373 Standard Test Method for Water Absorption, Bulk Density, Apparent Porosity, and Apparent Specific Gravity of Fired Whiteware Products*, 2006, ASTM International: West Conshohocken, PA.
47. ASTM, *C67 Standard Test Methods for Sampling and Testing Brick and Structural Clay Tile*, 2011, ASTM International: West Conchocken, PA.
48. ASTM, *C1167 Standard Specification for Clay Roof Tiles*, 2011, ASTM International: West Conshohocken, PA.
49. Rinne, H., *The Weibull distribution : a handbook*. 2009, Boca Raton: CRC Press http://www.crcnetbase.com/doi/pdfplus/10.1201/978142008.
50. Petrovic, J.J., *Weibull statistical fracture theory for the fracture of ceramics.* MTA Metallurgical Transactions A, 1987. **18**(11): p. 1829-1834.

APPENDIX A. MATLAB CODE

WEIBULL CUMULATIVE DISTRIBUTION FUNCTION

```
% Importing data from Excel file
a = '2012.06.05_90.xlsx';

% Flexure
data = importTestData(a,'Flexure','A31:H50');
Porosity = importTestData(a,'Porosity & Density', 'G14:HC14');

% Compression
%data = importTestData(a,'Compression','A31:H50');
%Porosity = importTestData(a,'Porosity & Density', 'G14:H14');

P = Porosity(1)/100;

Specimen = data(:,1);
Force = data(:,2);
MaxExt = data(:,3);
MaxLoad = data(:,4);
MaxStrain = data(:,5);
MaxStress = data(:,6);
MaxStress_SI = data(:,6)*0.00689475728; % Conversion from psi to MPa
Modulus = data(:,8);

% Removing untested specimens
Force(Force==0)=[];
MaxExt(MaxExt==0)=[];
MaxLoad(MaxLoad==0)=[];
MaxStrain(MaxStrain==0)=[];
MaxStress(MaxStress==0)=[];

MaxStress_SI(MaxStress_SI==0)=[];
Modulus(Modulus==0)=[];

[xe,ye,ze] = WeibullFunction(MaxStress);
xe % Weibull mean, variance and parameters for Stress

[xsi,ysi,zsi] = WeibullFunction(MaxStress_SI);

[x2,y2,z2] = WeibullFunction(Modulus);
x2 % Weibull mean, variance and parameters for Modulus

figure (1)
plot(ysi(:,1),ysi(:,2),'bx');
hold on
handles = plot(zsi(:,1),zsi(:,2),'r-
',zsi(:,1),zsi(:,3),'r:',zsi(:,1),zsi(:,4),'r:');
hold off
xlabel('Transverse Strength (MPa)','FontSize',10.25, 'FontWeight', 'bold');
ylabel('Probability of Failure','FontSize',10.5, 'FontWeight', 'bold');
title(sprintf('Apparent Porosity = %0.3f',P))
```

```
figure (2)
plot(y2(:,1),y2(:,2),'bx');
hold on
handles = plot(z2(:,1),z2(:,2),'r-
',z2(:,1),z2(:,3),'r:',z2(:,1),z2(:,4),'r:');
hold off
xlabel('Elastic Modulus in Flexure (MPa)','FontSize',10.25, 'FontWeight',
'bold');
ylabel('Probability','FontSize',10.5, 'FontWeight', 'bold');
title(sprintf('Apparent Porosity = %0.3f',P))
```

WEIBULL PARAMETERS AND STATISTICS

```
function [WeibullValues, Weibull_emp, Weibull_CI] = WeibullFunction(data)

[empF,x,empFlo,empFup] = ecdf(data); % Calculates empirical CDF

% Estimating Weibull parameters (2-param method: paramEsts(1)==scale factor;
paramsEsts(2)==shape factor)
paramEsts = wblfit(data);
[mean,variance] = wblstat(paramEsts(1),paramEsts(2));

% Fitting the Weibull distribution to the data
[nlogl,paramCov] = wbllike(paramEsts,data);
Max = 1.5*max(data); % Setting maximum x-axis value
xx = linspace(1,Max,500); % Generating vector for Weibull model
alpha = 0.05; % Confidence interval = (1 - alpha)
[wblF,wblFlo,wblFup] = wblcdf(xx,paramEsts(1),paramEsts(2),paramCov, alpha);

WeibullValues(1,1) = mean;
WeibullValues(2,1) = variance;
WeibullValues(3,1) = paramEsts(1); % Scale Factor
WeibullValues(4,1) = paramEsts(2); % Shape Factor

x(1,:)=[];
empF(1,:)=[];
empFlo(1,:)=[];
empFup(1,:)=[];
nn=length(x);
x(nn,:)=[];
empF(nn,:)=[];
empFlo(nn,:)=[];
empFup(nn,:)=[];

Weibull_emp(:,1) = x;
Weibull_emp(:,2) = empF;
Weibull_emp(:,3) = empFlo;
Weibull_emp(:,4) = empFup;

Weibull_CI(:,1) = xx;
Weibull_CI(:,2) = wblF;
Weibull_CI(:,3) = wblFlo;
Weibull_CI(:,4) = wblFup;
```

CURVE FITTING: STRENGTH VS. POROSITY

```
% Raw data in column vectors
porosity = [0.068293956, 0.157918777, 0.199390342, 0.238705579, 0.26194036,
0.32207726, 0.353890922, 0]';
Rdensity = [2.057570495, 2.013967218, 1.884468307, 1.828298613, 1.689011738,
1.64869763, 1.586948928, 2.496666667]'/2.496666667;
stress = [150.8231852, 95.85578076, 58.73356981, 39.72630857, 34.62236751,
13.76298208, 6.824050584, 2500]';

% Initialize arrays to store fits and goodness-of-fit.
fitresult = cell( 2, 1 );
gof = struct( 'sse', cell( 2, 1 ), ...
    'rsquare', [], 'dfe', [], 'adjrsquare', [], 'rmse', [] );


%% Fit: 'Exponential'.
[xData, yData] = prepareCurveData( porosity, stress);

% Set up fittype and options. Update coefficient in equation to published
value of zero porosity strength.
ft = fittype( '2500*exp(-a*x)', 'independent', 'x', 'dependent', 'y' );
opts = fitoptions( ft );
opts.Display = 'Off';
opts.Lower = -Inf;
opts.StartPoint = 0.959291425205444;
opts.Upper = Inf;

% Fit model to data.
[fitresult{1}, gof(1)] = fit( xData, yData, ft, opts );

% Plot fit with data.
figure( 'Name', 'Exponential' );
h = plot( fitresult{1}, xData, yData, 'predobs' );
legend( h, 'Experimental Data', 'Exponential', 'Lower bounds (Exponential)',
'Upper bounds (Exponential)', 'Location', 'NorthEast' );

% Label axes
axis([0 .40 0 3000]);
xlabel( 'Apparent Porosity','FontSize', 10.5, 'FontWeight', 'bold' );
ylabel( 'Compressive Strength (MPa)','FontSize', 10.5,'FontWeight', 'bold' );



%% Fit: 'Gibson-Ashby: Open'.
[xData, yData] = prepareCurveData( Rdensity, stress);

% Set up fittype and options. Update coefficient in equation to published
value of zero porosity strength.
ft = fittype( '2500*a*x^(3/2)', 'independent', 'x', 'dependent', 'y' );
opts = fitoptions( ft );
opts.Display = 'Off';
opts.Lower = 0;
opts.StartPoint = 0.0318328463774207;
opts.Upper = Inf
```

```
% Fit model to data.
[fitresult{2}, gof(2)] = fit( xData, yData, ft, opts );

% Plot fit with data.
figure( 'Name', 'Rational' );
h = plot( fitresult{2}, xData, yData, 'predobs' );
legend( h, 'Experimental Data', G-A: Open1, 'Lower bounds (Rational)', 'Upper
bounds (Rational)', 'Location', 'NorthEast' );

% Label axes
axis([0 .40 0 3000]);
xlabel( 'Relative Density','FontSize', 10.5, 'FontWeight', 'bold' );
ylabel( 'Compressive Strength (MPa)','FontSize', 10.5,'FontWeight', 'bold' );



%% Fit: 'Gibson-Ashby: Open2'.
[xData, yData] = prepareCurveData( Rdensity, stress);


% Set up fittype and options. Update coefficient in equation to published
value of zero porosity strength.
ft = fittype( '2500*a*x^(3/2)*(1+x^.5)','independent', 'x','dependent','y' );
opts = fitoptions( ft );
opts.Display = 'Off';
opts.Lower = 0;
opts.StartPoint = 0.913375856139019;
opts.Upper = Inf;


% Fit model to data.
[fitresult{2}, gof(2)] = fit( xData, yData, ft, opts );

% Plot fit with data.
figure( 'Name', 'Rational' );
h = plot( fitresult{2}, xData, yData, 'predobs' );
legend( h, 'Experimental Data', G-A: Open2, 'Lower bounds (Rational)', 'Upper
bounds (Rational)', 'Location', 'NorthEast' );

% Label axes
axis([0 .40 0 3000]);
xlabel( 'Relative Density','FontSize', 10.5, 'FontWeight', 'bold' );
ylabel( 'Compressive Strength (MPa)','FontSize', 10.5,'FontWeight', 'bold' );



%% Fit: 'Gibson-Ashby: Closed'.
[xData, yData] = prepareCurveData( Rdensity, stress);
```

```
% Set up fittype and options. Update coefficient in equation to published
value of zero porosity strength.
ft = fittype( '2500*a*(c*x)^(3/2)+b*(1-c)*x', 'independent', 'x',
'dependent', 'y' );
opts = fitoptions( ft );
opts.Display = 'Off';
opts.Lower = [0 0 0];
opts.StartPoint = [0.392227019534168 0.655477890177557 0.171186687811562];
opts.Upper = [Inf Inf 1];

% Fit model to data.
[fitresult{2}, gof(2)] = fit( xData, yData, ft, opts );

% Plot fit with data.
figure( 'Name', 'Rational' );
h = plot( fitresult{2}, xData, yData, 'predobs' );
legend( h, 'Experimental Data', G-A: Open2, 'Lower bounds (Rational)', 'Upper
bounds (Rational)', 'Location', 'NorthEast' );

% Label axes
axis([0 .40 0 3000]);
xlabel( 'Relative Density','FontSize', 10.5, 'FontWeight', 'bold' );
ylabel( 'Compressive Strength (MPa)','FontSize', 10.5,'FontWeight', 'bold' );
```

ELASTIC MODULUS IN COMPRESSION

```
files = dir('*.CSV');
n = length(files); % Number of raw data files in this batch

porosity = 0.262; % Update value as appropriate

for i=1:n
    S=int2str(i);
    filename = ['Specimen_RawData_' S '.CSV'];
    sheetname = ['Specimen_RawData_' S];
    M = xlsread(filename, sheetname,'A14:E2500');
    T = xlsread(filename, sheetname,'B3');

    M(:,4)=M(:,4)/100; % Convert from % as reported by Bluehill
    M(:,5)=M(:,5)*6.89475728; % Convert from ksi to MPa

    % Brings strain back to zero if gage length wasn't reset during testing
    if M(1,2) ~= 0
        M(:,2) = M(:,2)-M(1,2);
        M(:,4) = M(:,2)/T;
        M(1,4) = 0;
    end

    xlabel('Strain', 'FontSize',10.5, 'FontWeight', 'bold');
    ylabel('Stress (MPa)','FontSize',10.5, 'FontWeight', 'bold');
    title(sprintf('Apparent Porosity = %0.3f',porosity))

    LL = 0.2; % Lower limit
    UL = 0.7; % Upper limit

    % removing all data before (max*LL) is reached
    for j = 1:length(M)

        if M(1,5) < C * LL
            M(1,:)=[];
        end

        if M(1,5)> C * LL
            break
        end
    end

    % removing all data after (max*UL) is reached
    for j= 1:length(M)
        if M(j,5) > C * UL
           k=j;
           break
        end
    end
    M = M(1:k,1:5);

    % Plot "linear" portion of the stress-strain curve
    figure(2)
    hold all
```

```
    plot(M(:,4),M(:,5))
    xlabel('Strain', 'FontSize',10.5, 'FontWeight', 'bold');
    ylabel('Stress (MPa)','FontSize',10.5, 'FontWeight', 'bold');
    title(sprintf('Apparent Porosity = %0.3f',porosity))

    % calculate the elastic Modulus
    p = polyfit(M(:,4),M(:,5),1);

    % Calculate R^2
    y = polyval(p, M(:,4));
    yresid = M(:,5) - y;
    SSresid = sum(yresid.^2);
    SStotal = (length(M(:,5))-1) * var(M(:,5));
    rsq = 1 - SSresid/SStotal;

    Modulus(i,1) = p(1);
    Modulus(i,2) = rsq;
end
format long g
Modulus(:,1)
Modulus(:,2)
Modulus(3,:)=[];
Rsqr = mean(Modulus(:,2))
```

ELASTIC MODULUS IN FLEXURE

```
files = dir('*.CSV');
n = length(files); % Number of raw data files in this batch

porosity = 0.078;

for i= 1:n
    S=int2str(i);
    filename = ['Specimen_RawData_' S '.CSV'];
    sheetname = ['Specimen_RawData_' S];
    M = xlsread(filename, sheetname,'A10:E200');
    T = xlsread(filename, sheetname,'B3:B4');

    M(:,4)=M(:,4)/100; % Convert from % as reported by Bluehill
    M(:,5)=M(:,5)*6.89475728; % Convert from ksi to MPa

    % Brings strain back to zero if gage length wasn't reset
    if M(1,2) ~= 0
        M(:,2) = M(:,2)-M(1,2);
        M(:,4) = M(:,2)*T(2)*6/(T(1)^2);
        M(1,4) = 0;
    end

    xlabel('Strain', 'FontSize',10.5, 'FontWeight', 'bold');
    ylabel('Stress (MPa)','FontSize',10.5, 'FontWeight', 'bold');
    title(sprintf('Apparent Porosity = %0.3f',porosity))

    % removing all data after failure
    [C,I] = max(M(:,5));
    M = M(1:I,1:5);

    LL = 0.4; % Lower limit

    % removing all data stress is less than (LL*max).
    for j = 1:length(M)
        if M(1,5) < C * LL
            M(1,:)=[];
        else
            break
        end
    end

    % Plot "linear" portion of the stress-strain curve
    figure(2)
    hold all
    plot(M(:,4),M(:,5))
    xlabel('Strain', 'FontSize',10.5, 'FontWeight', 'bold');
    ylabel('Stress (MPa)','FontSize',10.5, 'FontWeight', 'bold');
    title(sprintf('Apparent Porosity = %0.3f',porosity))

    % calculate the flexural Modulus
    p = polyfit(M(:,4),M(:,5),1);
```

```
    % Calculate R^2
    y = polyval(p, M(:,4));
    yresid = M(:,5) - y;
    SSresid = sum(yresid.^2);
    SStotal = (length(M(:,5))-1) * var(M(:,5));
    rsq = 1 - SSresid/SStotal;

    Modulus(i,1) = p(1);
    Modulus(i,2) = rsq;
    %}
end
format long g
Modulus(:,1)
Modulus(:,2)
Modulus(3,:)=[];
Rsqr = mean(Modulus(:,2))
```

ELASTIC MODULUS VS. POROSITY

```
% Initialize arrays to store fits and goodness-of-fit.
fitresult = cell( 9, 1 );
gof = struct( 'sse', cell( 9, 1 ), ...
    'rsquare', [], 'dfe', [], 'adjrsquare', [], 'rmse', [] );

%% Raw Data
porosity = [0.068293956, 0.157918777, 0.199390342, 0.238705579, 0.26194036,
0.32207726, 0.353890922, 0]';
modulus = [1902.87543, 1173.813639, 1328.674305, 920.2174158, 1251.688132,
544.4069941, 429.1786447, 70420]';
[xData, yData] = prepareCurveData( porosity, modulus );


%% Fit: 'Hasselman'.

% Set up fittype and options.
ft = fittype( '70420*(1-(a*x)/((1+(a-1)*x)))', 'independent', 'x',
'dependent', 'y' );
opts = fitoptions( ft );
opts.Display = 'Off';
opts.Lower = -Inf;
opts.StartPoint = 0.568823660872193;
opts.Upper = Inf;

% Fit model to data.
[fitresult{1}, gof(1)] = fit( xData, yData, ft, opts );

% Plot fit with data.
figure( 'Name', 'Hasselman' );
h = plot( fitresult{1}, xData, yData, 'predobs' );
legend( h, 'Experimental Data', 'Hasselman', 'Lower bounds (Hasselman)',
'Upper bounds (Hasselman)', 'Location', 'NorthEast' );

% Label axes
axis([0 .40 0 80000]);
xlabel( 'Apparent Porosity','FontSize', 10.5, 'FontWeight', 'bold' );
ylabel( 'Elastic Modulus in Compression (MPa)','FontSize', 10.5,'FontWeight',
'bold' );


%% Fit: 'Brown - Biddulph - Wilcox'.

% Set up fittype and options.
ft = fittype( '70420*(1-a*x^(2/3))', 'independent', 'x', 'dependent', 'y' );
opts = fitoptions( ft );
opts.Display = 'Off';
opts.Lower = -Inf;
opts.StartPoint = 0.616044676146639;
opts.Upper = Inf;
```

```
% Fit model to data.
[fitresult{2}, gof(2)] = fit( xData, yData, ft, opts );

% Plot fit with data.
figure( 'Name', 'Brown - Biddulph - Wilcox' );
h = plot( fitresult{2}, xData, yData, 'predobs' );
legend( h, 'Experimental Data', 'Brown - Biddulph - Wilcox', 'Lower bounds
(Brown - Biddulph - Wilcox)', 'Upper bounds (Brown - Biddulph - Wilcox)',
'Location', 'NorthEast' );

% Label axes
axis([0 .40 0 80000]);
xlabel( 'Apparent Porosity','FontSize', 10.5, 'FontWeight', 'bold' );
ylabel( 'Elastic Modulus in Compression (MPa)','FontSize', 10.5,'FontWeight',
'bold' );


%% Fit: 'Phani - Niyogi'.

% Set up fittype and options.
ft = fittype( '70420*(1-a*x)^n', 'independent', 'x', 'dependent', 'y' );
opts = fitoptions( ft );
opts.Display = 'Off';
opts.Lower = [-Inf -Inf];
opts.StartPoint = [0.622055131485066 0.350952380892271];
opts.Upper = [Inf Inf];

% Fit model to data.
[fitresult{3}, gof(3)] = fit( xData, yData, ft, opts );

% Plot fit with data.
figure( 'Name', 'Phani - Niyogi' );
h = plot( fitresult{3}, xData, yData, 'predobs' );
legend( h, 'Experimental Data', 'Phani - Niyogi', 'Lower bounds (Phani -
Niyogi)', 'Upper bounds (Phani - Niyogi)', 'Location', 'NorthEast' );

% Label axes
axis([0 .40 0 80000]);
xlabel( 'Apparent Porosity','FontSize', 10.5, 'FontWeight', 'bold' );
ylabel( 'Elastic Modulus in Compression (MPa)','FontSize', 10.5,'FontWeight',
'bold' );

%% Fit: 'Hashin'.

% Set up fittype and options.
ft = fittype( '70420*(1-x)/(1+(1+v)*(13-15*v)/(2*(7-5*v))*x)', 'independent',
'x', 'dependent', 'y' );
opts = fitoptions( ft );
opts.Display = 'Off';
opts.Lower = 0.21;
opts.StartPoint = 0.22;
opts.Upper = 0.24;
```

```
% Fit model to data.
[fitresult{4}, gof(4)] = fit( xData, yData, ft, opts );

% Plot fit with data.
figure( 'Name', 'Hashin' );
h = plot( fitresult{4}, xData, yData, 'predobs' );
legend( h, 'Experimental Data', 'Hashin', 'Lower bounds (Hashin)', 'Upper
bounds (Hashin)', 'Location', 'NorthEast' );

% Label axes
axis([0 .40 0 80000]);
xlabel( 'Apparent Porosity','FontSize', 10.5, 'FontWeight', 'bold' );
ylabel( 'Elastic Modulus in Compression (MPa)','FontSize', 10.5,'FontWeight',
'bold' );


%% Fit: 'Spriggs'.

% Set up fittype and options.
ft = fittype( '70420*exp(-b*x)', 'independent', 'x', 'dependent', 'y' );
opts = fitoptions( ft );
opts.Display = 'Off';
opts.Lower = -Inf;
opts.StartPoint = 0.145538980384717;
opts.Upper = Inf;

% Fit model to data.
[fitresult{5}, gof(5)] = fit( xData, yData, ft, opts );

% Plot fit with data.
figure( 'Name', 'Spriggs' );
h = plot( fitresult{5}, xData, yData, 'predobs' );
legend( h, 'Experimental Data', 'Spriggs', 'Lower bounds (Spriggs)', 'Upper
bounds (Spriggs)', 'Location', 'NorthEast' );

% Label axes
axis([0 .40 0 80000]);
xlabel( 'Apparent Porosity','FontSize', 10.5, 'FontWeight', 'bold' );
ylabel( 'Elastic Modulus in Compression (MPa)','FontSize', 10.5,'FontWeight',
'bold' );


%% Fit: 'Ramakrishnan'.

% Set up fittype and options.
ft = fittype( '70420*(1-x)^2/(1+(2-3*v)*x)', 'independent', 'x', 'dependent',
'y' );
opts = fitoptions( ft );
opts.Display = 'Off';
opts.Lower = 0.21;
opts.StartPoint = 0.22;
opts.Upper = 0.24;
```

```
% Fit model to data.
[fitresult{6}, gof(6)] = fit( xData, yData, ft, opts );

% Plot fit with data.
figure( 'Name', 'Ramakrishnan' );
h = plot( fitresult{6}, xData, yData, 'predobs' );
legend( h, 'Experimental Data', 'Ramakrishnan', 'Lower bounds
(Ramakrishnan)', 'Upper bounds (Ramakrishnan)', 'Location', 'NorthEast' );

% Label axes
axis([0 .40 0 80000]);
xlabel( 'Apparent Porosity','FontSize', 10.5, 'FontWeight', 'bold' );
ylabel( 'Elastic Modulus in Compression (MPa)','FontSize', 10.5,'FontWeight',
'bold' );


%% Fit: 'Wagh-Poeppel-Singh'.

% Set up fittype and options.
ft = fittype( '70420*(1-x)^n', 'independent', 'x', 'dependent', 'y' );
opts = fitoptions( ft );
opts.Display = 'Off';
opts.Lower = -Inf;
opts.StartPoint = 0.239916153553658;
opts.Upper = Inf;

% Fit model to data.
[fitresult{7}, gof(7)] = fit( xData, yData, ft, opts );

% Plot fit with data.
figure( 'Name', 'Wagh-Poeppel-Singh' );
h = plot( fitresult{7}, xData, yData, 'predobs' );
legend( h, 'Experimental Data', 'Wagh-Poeppel-Singh', 'Lower bounds (Wagh-
Poeppel-Singh)', 'Upper bounds (Wagh-Poeppel-Singh)', 'Location',
'NorthEast');

% Label axes
axis([0 .40 0 80000]);
xlabel( 'Apparent Porosity','FontSize', 10.5, 'FontWeight', 'bold' );
ylabel( 'Elastic Modulus in Compression (MPa)','FontSize', 10.5,'FontWeight',
'bold' );


%% Fit: 'Wang'.

% Set up fittype and options.
ft = fittype( '70420*exp(-(b*x+c*x^2 ))', 'independent', 'x', 'dependent',
'y' );
opts = fitoptions( ft );
opts.Display = 'Off';
opts.Lower = [-Inf -Inf];
opts.StartPoint = [0.956134540229802 0.575208595078466];
opts.Upper = [Inf Inf];
```

```
% Fit model to data.
[fitresult{8}, gof(8)] = fit( xData, yData, ft, opts );

% Plot fit with data.
figure( 'Name', 'Wang' );
h = plot( fitresult{8}, xData, yData, 'predobs' );
legend( h, 'Experimental Data', 'Wang', 'Lower bounds (Wang)', 'Upper bounds
(Wang)', 'Location', 'NorthEast' );

% Label axes
axis([0 .40 0 80000]);
xlabel( 'Apparent Porosity','FontSize', 10.5, 'FontWeight', 'bold' );
ylabel( 'Elastic Modulus in Compression (MPa)','FontSize', 10.5,'FontWeight',
'bold' );


%% Fit: 'MacKenzie'.

% Set up fittype and options.
ft = fittype( '70420*(1-f1*x+f2*x^2)', 'independent', 'x', 'dependent', 'y'
);
opts = fitoptions( ft );
opts.Display = 'Off';
opts.Lower = [-Inf -Inf];
opts.StartPoint = [0.168990029462704 0.649115474956452];
opts.Upper = [Inf Inf];

% Fit model to data.
[fitresult{9}, gof(9)] = fit( xData, yData, ft, opts );

% Plot fit with data.
figure( 'Name', 'MacKenzie' );
h = plot( fitresult{9}, xData, yData, 'predobs' );
legend( h, 'Experimental Data', 'MacKenzie', 'Lower bounds (MacKenzie)',
'Upper bounds (MacKenzie)', 'Location', 'NorthEast' );

% Label axes
axis([0 .40 0 80000]);
xlabel( 'Apparent Porosity','FontSize', 10.5, 'FontWeight', 'bold' );
ylabel( 'Elastic Modulus in Compression (MPa)','FontSize', 10.5,'FontWeight',
'bold' );
```

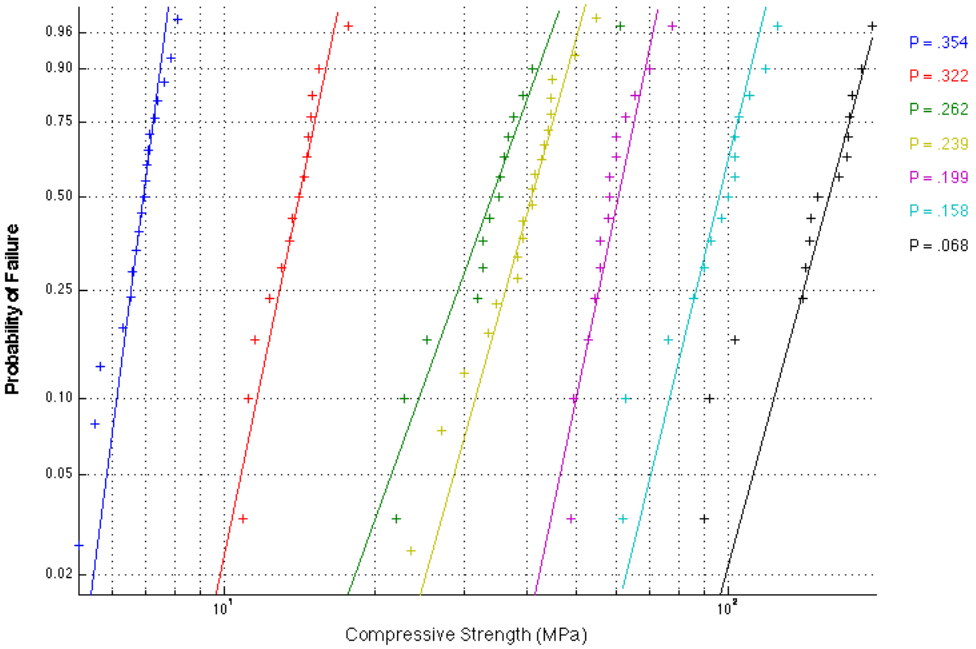

Figure 105. Weibull probability plot for compressive strength data.

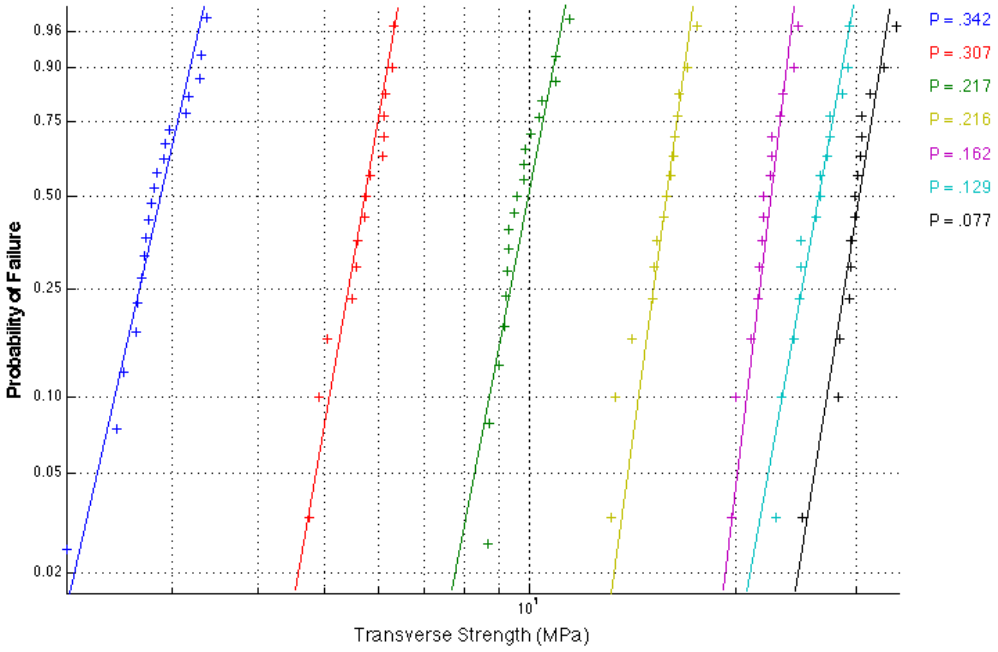

Figure 106. Weibull probability plot for transverse strength data.